UNIVERSITY OF CANTERBURY

Department of Physics and Astronomy

CHRISTCHURCH NEW ZEALAND

A thesis submitted in partial fulfilment of the requirements for the Degree of Master of Science in Medical Physics in the University of Canterbury, New Zealand

by

Jared Steel

Investigation into the Dosimetric Effects of Abutting Multi-Leaf-Collimated Photon Fields with Extended Source-to-Surface Electron Fields

Jared Steel

Year: 2005-2007

MSc Supervisors:
Assoc. Prof. Lou Reinisch & Allan Stewart

Abstract

This thesis reports on the findings of an investigation into the dosimetry resulting from the abutment of *en face* 6 MeV electron and 6 MV photon beams as applied to the clinical challenge of radiation therapy treatments to head and neck cancer sites. Particular concern is given to the use of multi-leaf collimator (MLC) technology for photon beam definition when abutted to extended source-to-surface (SSD) electron beams. We made dosimetric comparison between MLC and Cerrobend® shielding for use in an abutment situation. The effects of extending the SSD of the electron beam were also assessed. We checked the ability of a Pinnacle^3 v7.6 treatment planning system (TPS) to correctly model the dosimetry resulting from this extended electron beam SSD. Volumetric simulations of composite dosimetry resulting in water were conducted in MATLAB® for variations of surface abutment gap, and photon beam shielding type and angle. Visualization Toolkit (VTK) script was developed to visualise the resulting dosimetry. The effect of extending the SSD of the electron beam increases the beam penumbra significantly, exacerbating the challenge of matching this field to a photon beam edge. Furthermore, the TPS was shown to inaccurately model the electron beam penumbra for the extended SSD conditions. The employment of MLC shielding provides for some advantages over Cerrobend® in terms of overall composite hotspot volumes and coldspot magnitudes, though introduces detrimental dosimetric inhomogeneities in the underlying volume. Distinctly, no combination of abutment gap and shielding variables resulted in dosimetry in the range of 90% to 110% at the depth of d_{max} for the beam energies considered here. We provided tabulated data across these variables to outline the trade-offs present, and aid clinical decisions regarding this challenging dosimetric situation.

Acknowledgement

Scientific endeavour is rarely sustainable outside a nourishing cultural system. So it is to those individuals that comprise my locality in such a system that I wish to acknowledge. My supervisors Assoc. Prof. Lou Reinisch and senior physicist Allan Stewart are owed a massive debt of gratitude for their guidance and patience. Lou's keen scientific eye complements his compassion and enthusiasm for his students and their challenges; he helped enormously in bringing cohesion and clarity to this project. Allan tirelessly attended – to often mundane questions – with astuteness and consideration; and has guided this project from more than one deviation off the green. To my other colleagues at Auckland Regional Blood and Cancer Service, I extend much appreciation; the radiation therapists, oncologists, and physics staff were invariably approachable, and generous in the sharing of knowledge, suggestions, and encouragement. To principal physicist Isla Nixon I am especially grateful; her keen eye for detail helped level out many of the peculiarities inherent in the work of this author. I also extend major gratitude to Peter Smale and Phil Satory; these talented physics registrars provided insight and humour in times of darkness, and more than one bout of haphazard discourse resulted in the elucidation of new directions and research potential. To my close friends Lesley Smith, Luc Toussaint, and Lydia Shelton, I extend great respect and admiration; these excellent individuals made Auckland a new home – providing audacious and energetic companionship on many adventures that ultimately kept my mindset healthy. And of course, to my family – eternally encouraging and understanding through life's contemplations; I return much love and respect, and am equally proud of their pursuits and perceptions.

I also wish to acknowledge the Australisian College of Physical Scientists and Engineers in Medicine in association with the Auckland District Health Board for the local development of the medical physics registrar training scheme and the resulting opportunity to write this thesis.

Contents

Figures

Tables

Nomenclature

Auckland regional blood and cancer service	ARBCS
Beams eye view	BEV
Central axis	CAX
Computed tomography	CT
Cross-plane	CP
Depth of maximum dose deposition	D_{max}
Digitally reconstructed radiograph	DRR
Effective point of measurement	P_{eff}
Graphical user interface	GUI
In-plane	IP
Intensity modulated radiation therapy	IMRT
International atomic energy agency	IAEA
Linear accelerator	Linac
Monitor units	MU
Multi-leaf collimator	MLC
National radiation laboratory	NRL
Optical density	OD
Percentage depth dose	PDD
Portable network graphic	PNG
Radiation therapy	RT
Radiographic	RG
Region of interest	ROI
Source to surface distance	SSD
Technical report series	TRS
Thermoluminiscence dosimeters	TLD
Treatment planning system	TPS
Volume of interest	VOI
Visualization Toolkit	VTK

Chapter 1

Introduction

This chapter outlines the scientific and clinical context of this project, including a literature review, and provides overview to the direction of investigation.

1.1 Background

Head and neck cancer is ranked 11th in the world in terms of new presentations [1]. In New Zealand, it accounted for a regional average of 5.9 deaths per 100000, annually over the years 1994 to 2000 [2]. The successful treatment of head and neck cancer requires the inactivation of all cancerous tissue in regions both immediate and proximal to the tumour lesion. Lymphatic tumour involvement in this site is often poorly encapsulated, therefore attention to the surrounding tissues is required.

Radiation therapy provides a functionally conservative approach to treatment of cancer in the head and neck region. Treatment with high energy ionizing radiation is complicated however, by the presence of radiosensitive structures e.g. the spinal cord, in regions adjacent to the tumour. Further technical complications arise due to the surface contour geometries and tissue density heterogeneities typical of this physiological site.

At the Auckland Regional Blood and Cancer Service's (ARBCS) radiation therapy (RT) department, a technique is employed involving the combined use of high energy photon and electron beams. Lateral 6 MV photon beams deliver therapeutic dose to the lymphatic structures in the neck, however the underlying spinal cord must be shielded before the dose tolerance is exceeded (see Figure 1). A patent material, Cerrobend®, is specifically shaped and moulded for this shielding in each case. The unshielded target regions then receive the remaining prescription, however treatment to the volume overlying the spinal cord remains incomplete. The depth penetration characteristics of

electron beams in the MeV energy range allow the dose to this volume to be boosted without delivering significant additional dose to the underlying spinal cord. Currently, 6 or 9 MeV electron fields are abutted to the photon fields at the patient tissue surface. Due to practical treatment limitations, the electron beam is applied over an extended source to surface distance (SSD) in order to avoid physical complications with the patient's shoulder [3].

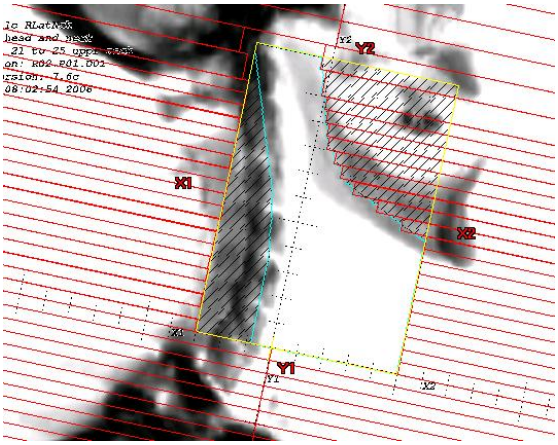

Figure 1: Digitally reconstructed radiograph (DRR) treatment planning image of shielded lateral photon field typical of head and neck cancer RT treatment cases. Here the region overlying the spinal cord is shielded with Cerrobend® (outlined in blue).

The ARBCS is looking into the possibility of replacing Cerrobend® with multi-leaf collimators (MLC) to define the photon beam in head and neck cases. The Varian® linear accelerators (linacs) at ARBCS are equipped with this technology and it is utilised widely for other RT techniques. Dosimetric concerns with regard to the matching of MLC defined photon fields with extended SSD electron fields form the basis of this investigation.

1.2 Literature Review

Briefly described here is previous research relating to technical or/or dosimetric aspects relevant to the abutment of extended SSD electron to MLC defined photon fields and the measurement thereof.

1.2.1 MLC

The MLC supplied with the Varian® EX 2100 Clinacs® at ARBCS consist of 120 leaves, the 40 central pairs each project a 5 mm geometric "shadow" at the treatment isocentre. A tongue-and-groove assembly allows each leaf to be independently driven along a path orthogonal to the beam central axis (CAX) [4].

Utilising MLC instead of Cerrobend® has a number of potential benefits including reduced patient setup times [5, 6] and a reduction of the RT departments mould room facility workload. Concerns arise over the intrinsically stepped shape of the shielding resulting from MLC – especially in regard to treatment situations requiring field matching – and the effects of dose contributions from inter- and intraleaf leakage/transmission [6].

When using MLC to shape small beams, including those used for intensity modulated radiation therapy (IMRT), caution is exercised regarding non-conformity to the beams eye view (BEV) shape of the target volume. Both geometric and dosimetric non-conformity relate inversely to field diameter for circular fields, and it has been suggested that the MLC be aligned along the minor axis of an elliptically-shaped field whenever possible [7]. As may be expected, non-conformity of 5mm MLC is about half that of 10mm MLC [7]. Thinner-leaved products such as BrainLAB's M3 MLC (3 mm leaves) are available and offer tighter penumbra (lateral separation of the 80% and 20% isodose lines) in the direction of leaf travel. However, these are limited to medium field sizes e.g. 9.8 cm × 9.8 cm at isocentre for the M3 [8].

The penumbral properties of photon beams shaped with MLC are also effected by the amount of stepping between adjacent leaves. A previous study showed that lateral separation of the 90% - 10% isodose widths in the direction both across the leaf tip (in-line), and across the leaf edge (cross-line), increased as leaf stepping increased from zero to a ratio of 1:1 (saw-tooth), and decreased again thereafter [9]. The same research found no significant discrepancies between penumbral widths measured across adjacent leaf tip corners due to the tongue and groove assembly. Dose calculation studies involving the

replacement of straight-edged Cerrobend® making selected angles in the plane orthogonal to the CAX with 1 cm stepped approximations, show increasing penumbral width as a function of step size [10].

There are also concerns regarding the ability of commercially available treatment planning systems (TPS) to model the penumbral region of MLC-defined beams accurately. For example, it was shown that the Pinnacle^3 TPS version 7.4f significantly underestimated the magnitude of the dosimetric coldspots on a profile along the average field edge for leaves with 1:1 stepping when compared to film measurements [9]. Pinnacle^3 version 7.6c, as implemented at ARBCS, takes into account the rounded leaf ends of Varian MLC s and also inter- and intraleaf leakage/transmission.

Intrafraction shifts or "feathering" of unstepped MLC has been shown to reduce the magnitude of hot and cold dosimetry resulting across the junction of an isocentric photon half-field match, for example, peak height-trough low values were reduced to a 3rd by two shifts of ±1 cm for double-focussed MLC on a Siemens linac [11]. Others have investigated the feathering of stepped leaves to smooth the resulting isodoses by either adjusting the lateral position of the volume under the beam and readjusting the MLC and asymmetric collimators [12], or by fractionally adjusting only the MLC leaf positions in the direction of leaf travel [13]. Results have shown that increased feathering (4 or 5 shifts) of 1:1 stepped leaves straightens out the 50% isodose line, which converges smoothly along the centre of the original (unfeathered) field edge. However, an increase in lateral spread relative to the 50% isodose of the 80% and 20% isodose lines was observed, leading to an *effective* penumbra significantly wider (≥ 1.7) than that provided by Cerrobend® [12, 13]. Note: that effective penumbra is defined as the separation between peaks of 80% and valleys of 20% isodose lines.

1.2.2 Electron beams at extended SSD

The dosimetric effects of applying high energy clinical electron beams over extended SSD have been investigated [14, 15]. The characteristics of electron beams depend on linac design and collimation method employed. Findings for Varian linear accelerators

with standard electron applicator collimation show small overall effects on the CAX percentage depth dose (PDD) profiles due to extended SSD [3, 16]. It is suggested that two competing interactions affect the surface dose as a function of increased SSD: that the increased mass within the air column leads to the increased preferential removal of lower energy electrons from the primary beam; conversely, that increased amounts of lower energy electrons are produced within a larger air column. However, the later effect only gains significance at very large SSD's such as those used in total body irradiation. For low energy electron beams e.g. 6 MeV, with medium field sizes, a decreased surface dose of between 5 and 10% can be expected for moderately extended (up to 130 cm) SSD's [14]. For 6 MeV electron beams the depth of maximum deposition (d_{max}), and the PDD through depth thereafter, are relatively unaffected by changes in SSD. For higher energy beams (>12 MeV), d_{max} appears to increase with increased SSD, though the flat nature of the PDD curve around this depth renders these changes relatively unimportant [14].

Off-axis dosimetry under clinical electron beams appears to be more sensitive to changes in SSD. The general effect of increased SSD is a loss of beam flatness as measured by the variation of relative dose across the beam width bounded by the 90% isodose at d_{max} [16]. Relative dose profiles taken in the plane orthogonal to the beam CAX appear broader with rounded beam edges [14, 15]. The 50% isodose, being the radiation and optical beam edge definition at standard SSD, shows a lateral shift for extended SSD [14, 17]. When beam divergence over the increased application distance is accounted for, this isodose drift appears outward from the CAX for small fields, and inward for larger fields [14]. The use of tertiary collimators e.g. collimators extending beyond the manufacturers standard applicator cones, has been investigated as a means of reducing the penumbral spread or beam broadening for spinal irradiation treatments. Such methods have proved successful in both reducing penumbral spread and increasing the lateral range of the clinically useful (80-90%) isodoses [18].

Conventional TPS modelling is known to be limited with regard to extended SSD electron beams, especially across the beam edge and dose fall-off region. Task Group 25

[3] recommends that the TPS modelling of extended SSD electron beam treatments be evaluated on an individual basis. Monte Carlo methods provide the most accurate electron transport and distribution modelling available, however the calculation times using current processing hardware render the techniques less than practical for all treatment planning in the clinical setting [16, 19].

1.2.3 Electron-photon field abutment dosimetry

A number of investigations have been made into the dosimetric challenges involved in the matching of clinical photon and electron beams [17, 20-26].

A film-based study by Papiez *et al* (1992) investigated the use of a stepped edge attenuator on a 4 MV photon beam for matching to a 10 MeV electron beam collimated with a lead cut-out preceding an acrylic plate of 1.25 cm thickness in addition to the standard applicator. The effect of using a stepped attenuator was simply a broadening of the photon beam penumbra, while the acrylic plate served to not only spread the penumbra slightly but also space the isodoses under the electron beam edge more evenly through depth. Using a parallel-opposed setup of the matched photon-electron beam pair, the effects of small positioning errors were assessed by varying the junction between the beams in each pair over the range +0.5 cm (overlap) to -1 cm (underlap) at 3 cm depth. Sampling profiles at 1 cm intervals over the depth range 1 to 13 cm within a phantom, they concluded that the beam edge modification led to improved dose uniformity across the junction, and was less sensitive to setup errors [20].

Karlsson & Zackrisson (1993) investigated the potential benefits and drawbacks of matching 20 MV photons with 10, 20, and 50 MeV electrons, using MLC. They measured the lateral distance between the field edge and the 80% isodose for the aforementioned beam qualities. This isodose separation was found to vary as a function of MLC stepping, from a distance of around 6mm for zero stepping to around 2mm from the leaf tips for a saw-toothed (1:1 leaf stepping) shielding shape. In terms of beam matching, around ±10% relative under- and over-doses were observed in small volumes [21].

Johnson & Khan (1994) explored the dosimetry resulting from the abutment of extended SSD 9 MeV electron beams with 6 MV photon beams. Films placed at 1.6 cm deep were exposed to 10 × 10 cm^2, 100 cm SSD photon beams abutted at the surface to 10 × 10 cm^2 electron beams (collimating inserts used to maintain projected surface field size with varied SSD), at selected SSD's from 100 cm to 120 cm. Profiles taken from these films showed the presence of a 20% hotspot which increased in size, but not significantly in magnitude, with increased SSD. On the other hand, a coldspot appeared on the electron beam side of the junction, and increased in magnitude with SSD, becoming significant (10%) at 120 cm SSD [17].

Sidhu *et al* (1995) investigated field abutments involving Cobalt 60 photon beam at 80 cm SSD and 9 MeV electrons at 100 and 115 cm SSD. Here, film was used in a block phantom to determine the dose distributions perpendicular to the beam CAX at 1.92 cm depth, and also parallel to the beam CAX across the field junction. Abutment involving the electron beam at standard SSD produced a 10% hotspot on the side of the photon beam. Extending the electron beam SSD resulted in a hotspot magnitude increase to 20%, and also the appearance of a significant coldspot (10%) near the surface on the electron beam side. This finding of increased hotspot magnitude with increased electron beam SSD contrasted Johnson & Khan's earlier findings, however it is suggested that differences in photon beam divergence (non-divergent in this case) in each study contribute to the observed differences in the behaviour of the hotspot dosimetry. Sidhu *et al* also investigated the effect of introducing a 0.5 cm abutment gap at the phantom surface between the photon and extended SSD electron fields. The effect of this was to reduce the magnitude of the hotspot to 10% but additionally increase the magnitude of the coldspot on the electron field side to 20%. Further film investigation using a cylindrical phantom, centred at the Co 60 beam isocentre and exposed to a parallel-opposed beam match setup, with 115 cm SSD for the electrons, showed consistent results as previously described. They concluded with the suggestion that the setup resulting in a 20% hotspot and 10% coldspot may be clinically acceptable given the

reality of the variance in day to day field positioning that would work to somewhat smooth out the dose imhomogenieties over the course of treatment [22].

Arthur *et al* (1997) describe a technique for matching lateral photon fields with anterior electron fields for the treatment of orbital disease. By employing pseudodynamic collimation of the photon beam edge, the profile across the anterior edge of this beam showed improved gradient reciprocity to the PPD curve of the electron beam. These methods reduced the dosimetric imhomogenieties from ±12% to ±2% though the accuracy of the treatment setup was crucial [23].

Sun *et al* (1998) assessed the surface abutment of laterally opposed isocentric 4 MV photon fields to a lateral 9 MeV electron field at an extended SSD of 110 cm. This investigation considered the effects of angling the lateral photon fields either 0° or 5° anteriorly (anterior oblique setup to avoid patient shoulders), as well as the effects of 2 mm electron field over- and underlaps for the anterior oblique setup condition. A dose of 120 cGy was prescribed to mid-plane from the photon beams, and to 3 cm depth (80% normalization) from the electron beam. Profiles were extracted from films located at 1 and 3 cm depth in one side of the phantom. Results for the non-angled lateral photon field setup showed a dose profile variation between 15% hot and 58% hot at 1 cm depth, and a variation between 10% cold on the electron side and 50% hot on the photon beam side at 3 cm depth. They noted that the normalisation point (120 cGy to 80% PDD) for the electron prescription automatically results in a 25% hotspot at d_{max} independent of photon contribution. The effects of angling the lateral photon fields each by 5° anteriorly had a marked effect on the combined dose profile at 1 cm. The dose contribution from the angled ipsilateral photon field resulted in a second combined profile peak located on the electron side of the abutment. Both peaks represented relative dose hotspot of 54% at 1cm depth. At 3cm deep the dosimetry under the electron beam was 23% hot. The effects of a 2 mm field overlap in the anterior oblique setup led to hotspots of 72% in the photon field and 54% in the electron field at 1 cm depth. The effects of a 2 mm field underlap (gap) in the same setup resulted in decreased magnitudes of the hotspots: 44% inside the photon field and 48% in the electron field at 1 cm depth. Overall, the effect of

the photon beam angulations is to prevent the occurrence of the 10% coldspot at 3 cm deep, however this is at the cost of increasing the magnitude of the hotspot on the photon field side. This angulation also served to prevent the occurrence of the coldspot even for a 2 mm field gap [24].

A computer modelling based investigation with film verification was conducted by Li *et al* (1999). Investigated here was the dosimetry involved in the abutment of a 9 MeV electron beam with a 6 MV MLC-defined photon beam. Here the SSD was 100 cm for both beams. Three cases were considered regarding the MLC-defined photon beam setup: full beam (divergent abutment field edge), half beam blocked (non-divergent abutment edge), and half beam block modified via modulation of the abutted field edge. Sub-cases considered were the variation of the photon-electron beam gap at the reference depth (2 cm) from 4 mm overlap to 4 mm underlap, in order to quantify the dosimetric sensitivity of each case to setup errors. Computer generated dose distribution profiles involving the unmodulated full photon beam, showed the characteristic cold and hot spots at 2 cm depth under the electron and photon beams respectively. Blocking half the photon beam resulted in improved uniformity across the abutment with a decrease in both hot and cold spots: 19% hot to 13% hot under the photon beam, and 16% cold to 14% cold under the electron beam. Intensity modulation of the half blocked photon beam edge resulted in a uniform dose profile at 2 cm across the abutment region. Profiles extracted at 1 and 3 cm in the modulated case were shown to be non-uniform, but this is expected due to the highly differential penumbral width of the 9 MeV electron beam through depth. At 3 cm depth the modulated beam dosimetry remained significantly better than for the unmodulated cases, however at 1 cm the effect of modulation appeared detrimental to dose homogeneity. In terms of technique sensitivity to setup errors, the effect of modulation improved the profile variation markedly over the other conditions for relative dosimetry at 2 cm depth. The authors suggest that this photon beam edge modulation technique could be used concurrently with other previously investigated methods of electron beam modification in order to realise even greater improvements in dosimetry in the region of photon-electron field matching [25].

Essers *et al* (2000) describe a technique for matching electron and photon fields in the irradiation of post-mastectomy treatment sites. They divide the photon contribution into three field segments relative to the electron field edge: 9 mm gap, 0 mm gap, and 9 mm overlap. Here, they employ a MM50 Racetrack Microtron (Scanditronix Medical) which has the ability to collimate both photon and electron scanned fields with MLC. Relative dosimetry measurements using both diodes and film indicate a dose variation between 88% and 109% at the phantom surface. Further work (2001) investigated the utility of a 5 diode array for improving patient *in vivo* dosimetry measurements for these RT techniques. It was demonstrated that the calibrated diode strip detector responded accurately with comparison to film, and had the advantage of on-line readout that the more commonly used thermoluminiscence dosimeters (TLD) don't, leading to decreased calibration, treatment measurement, and analysis times [26, 27].

Kemikler (2006) studied the head and neck abutment situation involving both laterally opposed divergent, and laterally opposed half-beam blocked (non-divergent) 6 MV photon beams abutted with 100 cm SSD, variable-trimmer collimated 9 MeV electron beams (from a Varian Saturne 42 linac). Using film at 1, 2, and 3 cm depths within a solid water phantom, separate exposures were made under both radiation modalities. Profiles were extracted from the films and then combined manually to represent composite profiles for each of the photon beam collimation conditions and 5 abutment situations: field match (no gap) or under- and overlaps of 2 and 4 mm at the phantom surface; repeated at each depth. Larger field overlap generally resulted in increased magnitude of the hotspots, and these were similar for both types of photon beam divergence. Hotspot magnitudes of around 40% were observed for the no gap abutment condition at 2 cm for each photon beam divergence case. Interestingly, the divergent photon beam case appeared favourable across the range of abutment gaps in terms of under dosing (coldspot): the composite dose profile relating to a 4 mm gap hovered above the 90% (10% cold) level, whereas it dipped as low as 72% (28% cold) for the non-divergent case. At 2 cm depth – closer to the d_{max} values for each beam – a significant coldspot (10%) appears for the divergent beam abutted with a 2 mm gap, and this was worse for the 4 mm gap situation. However, coldspot dosimetry was again

worse in the non-divergent photon beam case. It was again confirmed that dosimetry in the abutment region is very sensitive to variation in the abutment conditions [28].

1.3 Project Overview

Despite the head and neck being a specific treatment site among the many others encountered in radiation therapy, the modelling and measurements of the techniques involved in treating this site are strewn with limitations and complexities. Even aside from the differences arising from the selection of available therapy and measurement equipment, there are many variables to be considered as reviewed in the previous section e.g. beam energies, abutment gap/overlap size, beam definition options, depth in phantom/patient, and SSD's, to name a salient few. Not every combination has been investigated. Even some research areas already explored and presented need in-house verification and/or assessment.

The goal of this project was a three-dimensional investigation into the dosimetry resulting from the abutment of 6 MV MLC-defined photon beams with 6 MeV electron beams applied at an extended SSD of 110 cm. The situation requires measurement equipment that satisfies the following requirements:

- Has low energy dependency and high dose sensitivity.
- Provides good lateral spatial resolution in the high-gradient dose region at the beam edges.
- Provides good lateral spatial resolution of the projected MLC leaves defining the photon field edge.
- Provides good spatial resolution through depth of the build-up regions of both radiation modalities, and also the high-gradient dose fall-off region of the electron beam.
- Can be positioned and registered accurately in three dimensions.

We had a selection of dosimetry equipment at our disposal, including radiographic (RG) verification film, film densitometer, computer-controlled film densitometer, ionisation chambers, silicon diodes, and a computer-controlled 3D scanning water-tank. Details of this equipment will be expanded upon in chapter 2. The current TPS is a Pinnacle^3 version 7.6c system.

We investigated the effects of increasing the electron beam SSD from 100 cm to 110 cm. Comparison was made between measured electron beam data and TPS modelled data for this extended SSD situation. Acquisition of relative dose deposition data was made in water separately under the field edges of both the radiation beam types. This data was collected at several depths in the water-tank. Dosimetric data was obtained under selected MLC stepping regimes, as well as under Cerrobend® matching one of these MLC designs. Investigation was conducted into the effects of MLC stepping on the penumbra properties of the photon beam, and comparison was made to the Cerrobend®-defined beam edge. Relative dose data under the photon beam conditions was added to the relative dose data acquired under the electron beam using mathematics computer software in order to create a composite volumetric dosimetry situation. Field abutment shifts were simulated by varying the co-registration of the datasets on the scale of the resolution of the scanned data. A film-based study was conducted to assess the validity of combining the separate beam data in this manner. Precise details on the methods employed are presented in chapter 2.

Analyses of each dosimetric volume composition were designed to assess how the dosimetry was affected as a function of the variables outlined above. Techniques were developed to aid visualisation of the volumetric dosimetry. Results of the analyses are presented in chapter 3, including graphs and tables generated to assist clinical decisions with regard to this treatment challenge. Discussion regarding the results of this project is provided in chapter 4.

Chapter 2

Methods and Materials

This project is an investigation into the relative dosimetry produced within a volume of tissue-equivalent material exposed under the adjoining region of high-energy electron and photon fields. Special concern is given to the situation where MLC is employed to provide the orthogonal definition of the photon beam. Methods were developed to resolve the MLC, and simulate the resulting dosimetry under different combinations of field abutment gap and MLC stepping. A study was conducted to assess the validity of the simulation method. Investigation was made into how the abutment gap size and MLC stepping influences the underlying dose distributions. Additionally, simulations of dosimetry resulting from the use of Cerrobend® to define the photon beam were performed, and methods were developed for which to compare the two shielding modes.

All relative dose measurements were performed using a Wellhofer WP700 dosimetry system, including a water tank, p-type silicon diodes, electrometer, and client software version 3.51.00. A Varian Clinac® 600C/D sn 483 (600/1) was used for a diode depth-dose comparison. Array measurements of relative dose were obtained under the photon and electron beams produced by a Varian Clinac® 2100EX sn 1767 (2100/3). This linac is equipped with a Millennium 120 MLC system for photon beam collimation. The electron beams were collimated using standard Varian 10 × 10 cm^2 applicators. Cerrobend® was shaped and moulded in the departments mould room facility and employed in the shielding of the photon beam in a selected case. Film based dosimetry measurements were conducted using Kodak X-OMAT V radiographic verification film exposed to beams generated from the 2100/3 linac detailed above, then developed and fixed using the departments Kodak X-OMAT 3000 RA processor. Optical density (OD) spot measurements were taken using a Victoreen Digital Densitometer II, and OD profiles were extracted using a Wellhofer WP102 densitometer. The WP102 densitometer provides a practical spatial resolution of 3 mm.

2.1 Experimental Methods

Scan array datasets of relative dosimetry were acquired in water under both photon and electron beams for which to use to simulate variations on field abutment gap and MLC angle. See Figure 2 below for the definition of abutment gap used in this investigation. In order to resolve the MLC leaves, a novel use of the available diode detectors was employed. These methods required validation before we could proceed with the greater investigation. Film was exposed to both radiation modalities under varied field abutment conditions to qualitatively check the results of the simulations. In order to ensure the film results were meaningful, a sensitometric analysis of the film for both beam modes was conducted.

2.1.1 Diode response

A Wellhofer-Scanditronix FP 1949 diode was used in two orientations relative to the beam CAX (see Figure 3) to measure relative dosimetry in the Wellhofer water tank. The FP 1949 diode is a p-type silicon diode with an active element located 0.40 mm ± 0.10 mm below the front face of the detector. This element has a diameter of 2.5 mm ± 0.1 mm, a physical thickness of 0.50 mm ± 0.02 mm, and an effective thickness of 60 μm. The response of this diode to a 6 MV photon beam was compared to the response of another silicon diode – the FP 1942. The FP 1942 diode has a similar construction; however its active element is located at 0.57 mm ± 0.15 mm from the front detector face. Additionally, this diode has tungsten embedded in the detector casing in order to attenuate low-energy scattered photons. The FP 1942 is the diode normally used in photon beam measurements.

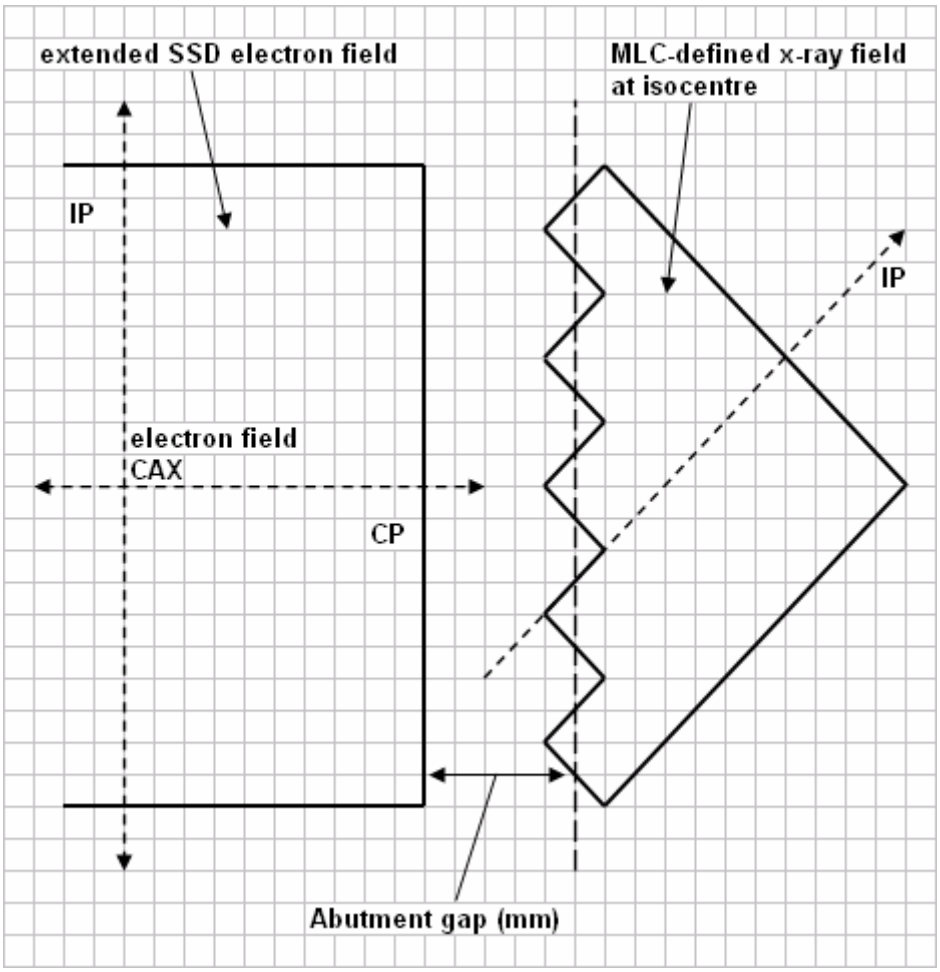

Figure 2: Definition of electron-photon field abutment gap. Not to scale.

Relative dose scans through depth were performed under the 6 MV photon beam of the 600/1 linac using the Wellhofer dosimetry system. Each diode was used in two orientations relative to the beam CAX. The first being oriented so that the front face of the diode faced the direction parallel to the beam CAX, and secondly, so that the front face of the diode was directed orthogonal to the beam CAX (see Figure 3). For the first orientation, the front face of each diode was zeroed at the water surface, and the offset for effective point of measurement (P_{eff}) was set in the Wellhofer software. The offsets used were the physical displacements of the active elements from the front face of each diode. When the diodes were used in the second orientation, the diodes were zeroed so as the water surface covered half of the front face, and no offset was applied. The rotational position of the diode in the second orientation was registered using a small mark on the diode casing.

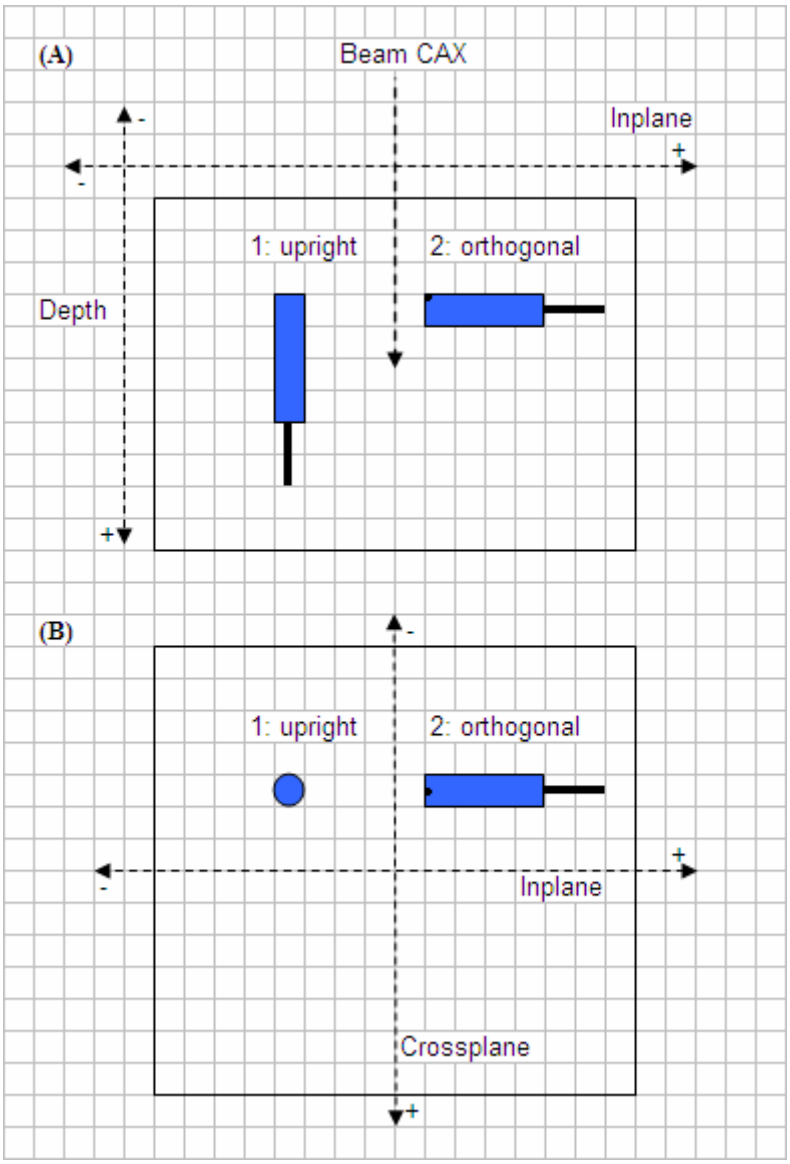

Figure 3: Definition of scan directions and diode orientations. Schematics of a side view of the water tank and diodes (A), and a beams eye view (BEV) of the water tank (gantry angle = 0°) and diode set up (B). Figure not to scale.

For all depth-dose measurements, the SSD was set at 98.5 cm, using the front-pointer rods supplied with the linac. The field size was set at 24 × 24 cm^2. The depth-dose measurements were taken from the water surface to a depth of 60 mm under the beam CAX, and curves of PDD were generated.

2.1.2 Patient data survey

We carried out a basic background survey on a random sample of 12 previous head and neck patient plans, to determine what shielding angles relative to the beam inplane (IP) axis were being used for the Cerrobend® shielding of the spinal cord. We also determined the average field sizes, and the displacement of each field centre from the CAX. These measurements were taken using a ruler, protractor, and pencil, on printed copy plans. From plans involving non-continuous or irregular shielding shapes, we measured the greatest angle that the shielding made with the IP axis. The results of this were used to design the experimental shielding conditions as further described in section 2.1.3 and Figure 4 of this chapter. Details of these results are found in the next chapter.

2.1.3 Beam edge dosimetry

Diode scanning performed using the Wellhofer water tank dosimetry system was conducted to investigate the relative dose distribution in a volume located across the radiation beam edges. Spatially, the measurements were comprised of line scans covering a horizontal area of 50 × 50 mm^2, repeated for seven depths: 5, 10, 15, 20, 25, 30, and 35 mm. For measurements of photon beams defined by either Cerrobend® or MLC, this scan volume extended ±25 mm along the beam crossplane (CP) axis, and was located between +35 mm and +85 mm along the beam inplane (IP) axis. For measurements of the 6 MeV electron beam, this volume was located under the positive CP field edge of a 10 × 10 cm^2 applicator: extending from +25 mm to +75 mm in the CP direction, and ±25 mm in the IP direction. The line scans were sampled along the CP direction for all measurements. Table 1 below outlines the various physical parameters that were used for the water tank measurements under different mode and shielding combinations. For all measurements the gantry angle was set to zero using a spirit level. SSD’s were set using the front pointer rods.

Table 1: Wellhofer WP700 measurement parameters

Mode/Shielding		**Photons - MLC**	**Photons - Cerrobend®**	**Electrons**
Nominal energy		6 MV	6 MV	6 MeV
Dose rate		300 MU/min	300 MU/min	300 MU/min
SSD		98.5 cm	98.5 cm	110 cm
Primary collimator jaw settings	X1	3.5 cm	3.5 cm	20×20 cm^2
	X2	7.5 cm	7.5 cm	
	Y1	0.5 cm	0.5 cm	
	Y2	12.5 cm	12.5 cm	
Diode orientation		orthogonal to CAX (2)	orthogonal to CAX (2)	upright (1)

MLC leaf stepping positions were calculated to generate shielding that would approximate shielding lines angled at 0°, 15°, 30°, and 45° to the beam IP axis. These fields were all situated in the positive IP direction. The linac collimator angle was set to zero degrees, so the collimating leaves were aligned in the direction of the CP axis. Leaf 41 in leaf carriage B was positioned to meet the IP axis for all four MLC edge angles. MLCshaper (version 6.1, © Varian Medical Systems) was used to generate and validate the leaf position files for use in the Vision 4D console version 8 software (build 8.0.16, © Varian Medical Systems, 2005). See Figure 4 for images of the MLC positions for each MLC-defined photon field as taken from MLCshaper. A Cerrobend® block was manufactured to represent an identical shielding line to the mid-leaf MLC shielding line making 30° to the beam IP axis.

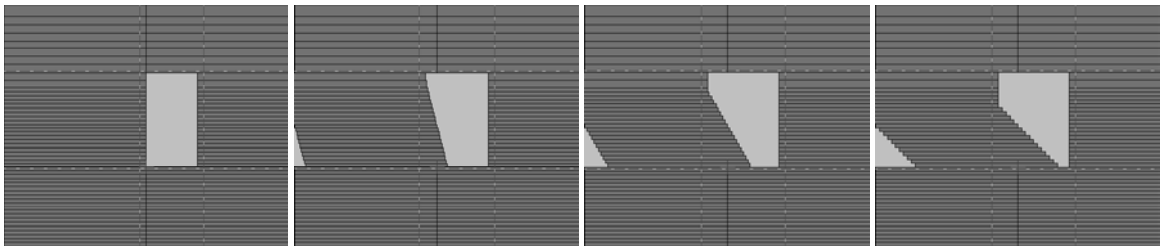

Figure 4: Position of photon fields, and the collimating leaves for MLC angled 0°, 15°, 30°, & 45° relative to the in-plane axis (note: the leaves run in the CP direction).

For our relative dosimetry measurements, the following parameters were set in the Wellhofer software, and are universal for all measurements using diodes discussed here: high voltage set to zero, channel polarity set negative, sensitivity set to low, and background subtraction applied. Software settings specific to radiation mode and/or beam shielding type are outlined in Table 2 below.

Table 2: Wellhofer WP700 software parameters

Mode/Shielding	**Photons - MLC**	**Photons - Cerrobend**	**Electrons**
Correction for P_{eff}	0 mm	0 mm	-0.4 mm
Scan line spacing	1 mm	2 mm	2 mm
Scan speed	3.58 mm/s	5.13 mm/s	5.13 mm/s
Scaling mode	Current position	Current position	Reference position
Norm position (CP, IP, depth)	(3.0, 6.0, 1.5) cm	(3.0, 6.0, 1.5) cm	(0.0, 0.0, 1.5) cm
Field channel gain	50	51	52
Ref channel gain	37	38	40

For the beam-edge scanning using the Wellhofer system, the levelling of the tank was checked to ensure that the detector tracked parallel to the water surface in both the IP and CP directions. The horizontal zero position of the detector was always set using the optical cross to position it on the CAX. The vertical zero position was set as for the diode response investigation detailed above.

Scan times are determined by the detector scan speed and the scan line spacing over the area required. Even at low dose rates, the limit of 999 monitor units (MU) set in the clinical mode provides an inadequate beam-on time. Hence the linac was run in service mode in order to provide an extended amount of 9999 MU as needed. The dose rate was set at 300 MU/min and the dose servo interlock disabled. Given these settings, an actual dose rate of around 320 MU/min was typical for this data acquisition.

Area scans at the seven depths, under the varying shielding and beam modes, were saved in the Wellhofer dosimetry software. Interpolation to 0.3 mm was performed using

the Wellhofer client software cubic interpolation algorithm under the “array” toolbox. Each scan was then exported to ASCII format for subsequent external processing.

Methods were developed to process the relative dosimetry data extracted from the Wellhofer system. Imported to the MATLAB® work space, the scans at depth were delimited (see Appendix B.1.1) and grouped according to field-edge type i.e. MLC (and angle), Cerrobend®, or electron field. A rotation process (see Appendix B.1.2) was applied to the photon scan arrays in order to bring the shielded field edge parallel to the array column edge. Each group was then saved to *.mat format for ease of calling and inclusion in custom MATLAB® script files. Another script file was built to calculate the abutment gap at the surface, and 15 mm depth (d_{max}), based on the geometry of the beams; taking into account beam rotation, divergence under different shielding angles, and the different SSD’s involved (see Appendix B.1.3).

2.1.4 Film sensitometry

The use of radiographic film as a means of qualitative dosimetry for combined modality radiation dose distributions was investigated. A range of MU (10, 20, 40, 50, 60, 80, and 100) exposures from both the 6 MV and 6 MeV beam modes were delivered to film, with 15 mm solid water build-up, and 30 mm of this material to provide full back-scatter conditions. For the photon beams the collimating jaws were set to 10 × 10 cm^2, and each film was placed at the isocentre i.e. an SSD of 98.5 cm was used. For the electron beams, the films were placed under 15 mm build-up at 100 cm SSD, and we employed a 10 × 10 cm^2 applicator. The departments clinical electron applicator factors are normalized to the use of 15 × 15 cm^2 applicator. For the use of a 10 × 10 cm^2 applicator on the 2100/3 Clinac, this factor is 1.00; therefore no adjustment to the MU’s listed above was needed. Using the larger (33 × 41 cm) sized X-OMAT V verfication film, four different radiation fields were delivered per film, spreading the range of MU exposures across two films per radiation mode (see Figure 5 below). Each film contained an exposure from a 50 MU delivery in order to check for any inter-film sensitivity variations. The MU spread for each radiation mode was as such: film A – 10, 40, 50, 100; film B – 20, 50, 60, 80.

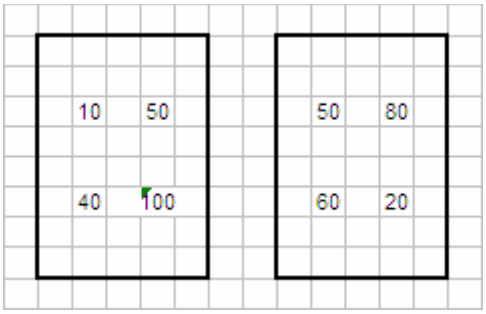

Figure 5: Schematic of MU distribution between two RG films for sensitometry study.

After processing, the average OD from four points in each field exposure were measured and recorded. Background OD was measured and averaged from near each edge of each film, and this was subtracted from the field readings. The OD data was plotted against MU, and curves for each radiation modality were fitted to this sensitometric data.

2.1.5 Film dosimetry

Radiographic film was used to sample the dosimetry resulting from the application of selected treatment conditions as relevant to this investigation. We abutted the MLC photon field (created to approximate a 45° angle to the IP) with the 10 × 10 cm^2 electron applicator field for two pre-determined gap sizes: 6.0 mm field overlap and 7.5 mm underlap; at a depth of 15 mm in solid water. Lines representing the abutment gaps were drawn on the film packets for registration with the optical field edges. In turn, each film was registered to the mid-leaf points on the MLC-defined photon field edge at isocentre. 15 mm build-up was added to bring the SSD to 98.5 cm, and then the film was exposed to 40 MU of the 6 MV photon beam. Subsequently for each, the SSD was adjusted to 110 cm and the build-up removed in order to register the respective abutment gap line to the optical field edge of the 10 × 10 cm^2 electron applicator. With the 15 mm build-up replaced, the films were then exposed to 52 MU from the 6 MeV electron beam (see Appendix A). Additionally, each film was exposed to another identical MLC-defined photon beam under the same set-up conditions for the photon beam above: MLC = 45°, SSD = 98.5 cm, 15 mm build-up, and 40 MU. These exposures were positioned over a

fields length away from the fields involved in the abutment, and were included for normalization purposes. The films were processed as detailed in previous sections.

The two films then represented a combined dosimetry at 15 mm depth in solid water for the use of MLC approximating 45°, abutted with an extended SSD electron field, for two different abutment gaps. From each, we measured OD profiles perpendicular to the adjoining field edges using a Wellhofer WP102 densitometer. These OD profiles were normalised to the un-abutted 40 MU photon field, and then exported at a resolution of 0.3 data points per millimetre to ASCII format for further analysis using MATLAB®.

2.1.6 Beam edge inspection

2.1.6.1 Effects of MLC stepping on photon beam penumbra

The photon beam diode scan arrays were concatenated through depth for each MLC stepping regime (see Figure 4) in the MATLAB® workspace (see section 2.1.3). Using the "mean" function, the 167×167×7 volumetric datasets were converted to 167×7 2D arrays representing the mean beam edge dosimetry across each MLC-defined beam edge. The "contour" function was employed to map isodose lines within these arrays. A script file was designed that measured the lateral separation between the mean position of the 20% and 80% isodoses at the 7 scan depths for each MLC beam edge off the contour data (see Appendix B.1.4). We repeated the process for the photon beam edge as defined by Cerrobend® for comparative purposes.

2.1.6.2 Dose inhomogeneity due to MLC stepping

Further comparison was made between the relative dosimetry resulting from MLC shielding and that resulting from Cerrobend®. Here, volumetric datasets were constructed, in the manner described above, from the photon beam scans employing MLC shielding stepped to make a 30° angle with the beam IP axis (see Figure 4). The corresponding photon beam dataset obtained under the 30° Cerrobend® shielding was subtracted from this structured MLC beam data. Determination of the size of the hot and cold regions within this volume was conducted. To make such volumetric determination we wrote a script in MATLAB® that ran a simple logic statement through the subtraction

dose volume based on a user-defined relative dose threshold (see Appendix B.1.5). This procedure returned a corresponding logic matrix of the same initial matrix size, where entries of unity represented the user-defined hot or cold data elements, and entries of zero represented voxels not exceeding the threshold. The elements of unity within the logic matrix were summed, and this sum in turn divided by the total amount of scan voxels, thus representing the hot or cold regions as a percentage of the total scan volume. VTK techniques were used to visually represent the hot and cold regions.

2.1.6.3 Effects of extending SSD for 6 MeV electron beams

Using the Wellhofer dosimetry system we performed relative dose scanning under the 10×10 cm^2 6 MeV electron beam at 100 cm and 110 cm SSD's using the unshielded electron diode FP 1949 in the upright orientation. This scanning comprised of sampling relative dose both through depth under the beam CAX, and across the CP direction at selected depths in water (10, 15, 20, 25, 30 mm). All scanning was normalised at d_{max} (15 mm). With exception to "scan spacing" and "SSD" all scanning parameters used here are the same as presented in Table 1 and Table 2 for electrons.

The PDD data for both SSD conditions was collected down to 40 mm depth under the water surface. These were exported from the Wellhofer to the MATLAB® workspace via an ASCII format. Here, a subtraction of the extended SSD profile from the standard SSD profile was made for comparative purposes.

We scanned over the range ±85 mm in the CP direction for the beam edge profiles. These CP profiles at each depth were mirrored and averaged using the "mathematics" toolbox in the Wellhofer software. We exported half-profile (from 0 mm to 85 mm CP) relative dose vectors to the MATLAB® workspace via an ASCII format. Here the CP axes of the extended SSD CP profiles at d_{max} were rescaled to account for divergence over the additional CAX distance, and presented against the CP profiles at d_{max} obtained under standard SSD conditions. For CP profiles at the depths where both a 20% and 80% isodose was present, we measured the lateral separation of these isodoses, and presented them for both SSD conditions.

2.1.6.4 Testing TPS modelling of extended SSD electron beams

Using the ARBCS Pinnacle^3 TPS we setup a simple treatment simulation where an *en face* 10×10 cm^2 modelled electron beam exposed a semi-infinite "water phantom" over an extended SSD of 110 cm. Using the "profiles" toolbox we sampled the dose from the CAX to 10 mm CP at depths of 15 and 25 mm. These vectors were imported to the MATLAB® workspace for normalisation, and then compared with the measured electron CP profiles (see section 2.1.6.3) at the corresponding depths. Additionally the MATLAB® curve fitting toolbox was utilised in order to generate Gaussian functions describing each depth profile. Since the resolution of the data obtained from each source differed, we chose to ascertain well-fitted Gaussians with which to then reassert over fresh positional data of equal resolution. This allowed the subtraction of the curve fitted to the TPS data from that fitted to the measured data, in order to determine relative dose differences across the half-beam profiles between measured and modelled extended SSD electron profiles.

2.2 Abutment simulation and analytical methods

As described in section 2.1.3, the scan array data was exported from the Wellhofer system to the MATLAB® workspace, delimited, rotated, and then categorised for subsequent calling. Abutment simulations were produced by adding permutations of the rotationally aligned photon field edge datasets to the electron field edge datasets. Determinations of the abutment size at the surface were made for each combination of abutment conditions. Thus all analysis on the abutment volume could be associated with the abutment gap and shielding type/angle variables.

2.2.1 Composite profile discrepancies

In this part of the investigation we were interested in how a relative dose profile taken perpendicular to the field abutment line may be influenced as a function of the field edge angle approximated by MLC, and abutment gap size. The use of Cerrobend® to define a photon beam edge angled relative to the IP axis results in a field edge that is both straight and continuous. If there are no localized variations in shielding material

thickness or density, or the beam intensity, then any two relative dose profiles taken perpendicular to the abutment will not differ. MLC however, provides a stepped approximation for the shielding line, where the amount of inter-leaf stepping increases with the angle relative to the IP axis.

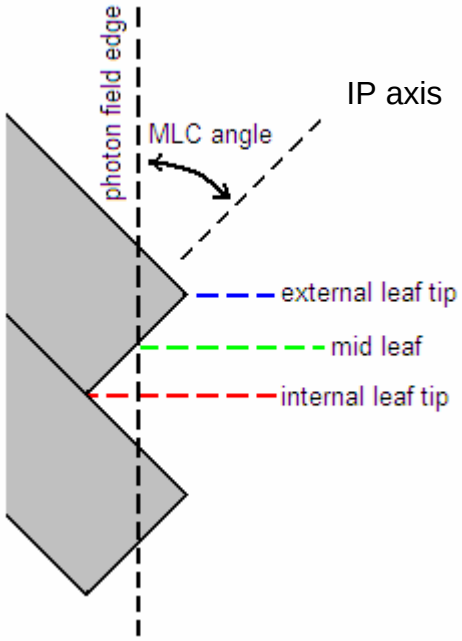

Figure 6: Definition of MLC-defined photon field edge, MLC angle, and locations of orthogonal scan profiles. Figure not to scale.

From the combined relative dose arrays at d_{max}, we extracted profiles from across three different points on an MLC leaf: both leaf tip corners, and the mid-leaf point (see Figure 6). This was repeated for three different leaves involved in the field abutment, and these profiles averaged for each leaf sample point. We conducted an analysis of how relative dose at a set distance along the electron field cross-plane axis could vary as a function of MLC angle, and abutment gap size.

2.2.2 Hotspot magnitudes

We wished to investigate the maximum point dose, or "hotspot" magnitude, that would result from combinations of MLC angle and abutment gap size. In the MATLAB® workspace this can be done through use of the "max" command. For a volume, this command must be nested three times in order to ascertain the singular minimum value. We wrote a short script file that samples the maximum value from each combined dosimetry volume for each volume in the abutment gap range: ~11 mm, for a given MLC/Cerrobend® angle (see Appendix B.1.6).

2.2.3 Hotspot volumes

Here we are concerned with the amount of relative-dose data that exceeds an upper dose threshold value. In this investigation that value was set at 110% relative dose. We investigated how the extent of this volume would change as a function of the abutment gap and MLC angle variables. Comparison with the use of Cerrobend® was also made. These volumetric determinations were made in a similar manner as outlined in 2.1.6.2, except involving composite dosimetry with analytic repetition performed over each abutment and shielding variation (see Appendix B.1.7). Additionally, the percent volume values were converted back to physical dimensions.

2.2.4 Minimum point dose at d_{max}

Essentially the same data analysis methods as detailed in the section 2.2.2, except that we utilise the "min" command in the MATLAB® workspace to sample the minimum relative dose value in composite relative dose dataset (see Appendix B.1.8). We also investigated the effect of MLC stepping and compared MLC to Cerrobend®.

2.2.5 PDD-normalised dosimetry

This part of the dosimetric analysis was designed especially to investigate elements of combined-scan volume below a certain lower relative-dose threshold. By dividing dose data at any depth by the percentage depth dose (PDD) value for that depth, we obtained PDD-normalised scan volumes. Once normalised, relative threshold factors of 90% (0.9) or 110% (1.1) could be applied using a similar logic procedure as described in a previous

section (see Appendix B.1.9). Thus, this method factors out the depth variable contribution to the combined dosimetry, leaving “hot” and “cold” voxels as a function of abutment gap and shielding angle only. However, the situation is complicated by the fact that in the abutment region, we have relative dose contributions from two beam modes which have different PDD characteristics (presented in chapter 3). We are therefore not justified to normalise the entire dataset with PDD data from either beam mode. In order to avoid this issue, we divided our combined-scan volumes into two volumes of interest (VOI) along the geometrical edge (MLC mid-leaf points) of the photon beam – accounting for beam divergence through depth. Once separated, the VOI on the electron beam side of the abutment region was normalised with the relevant PDD data, and the thresholding logic process applied.

2.3 Composite dosimetry volumetric visualisation

For interpretive benefit, a process was constructed to visualise the composite relative dose scan data. The scan arrays were concatenated in MATLAB® as described in a previous section. A MATLAB® script file was written to export the volumes into a *.vtk format (see Appendix B.1.10). This format is utilised by the Visualization Toolkit (VTK) (version 5.0), which is the open-source code of an object-oriented system of 3D graphics and visualisation. The system is built on a compiled C++ class library. Interpretive languages such as Tcl are used to interface with this system [29].

We wrote Tcl code to interpret the scan data as points structured in 3D separated by the respective spatial resolutions in the IP, CP, and depth scan directions. From there a VTK data “pipeline” was constructed consisting of filters, mappers, “actors”, and renderers; with which to interrogate the structured points dataset. Two principle types of interrogation were conducted: planar slices through the x, y, and z directions of the data, mapped through a transparent lookup table with user-controlled window and levelling; and isosurface contour mapping. The later mapper was constructed in two forms: firstly as a variable, user-controlled, iso-surface; and secondly, as set of iso-surfaces, of values defined in the Tcl script (see Appendix B.2).

These visualisation “widgets” were constructed to run concurrently, if necessary, on the structured points data, so that the user could take both planar slice views as related to the iso-surface(s) within the composite scan volume. Through these methods, spatially represented composite dosimetry, as a function of abutment gap and shielding type/angle, could be readily observed.

Chapter 3

Results

3.1 Diode Response

We compared the response of two n-type diodes to a 6 MV nominal energy photon beam through a depth range of zero to 150 mm. In turn, each diode was used in two orientations relative to the CAX – parallel and orthogonal. Figure 7 below shows the results of this depth dose response survey.

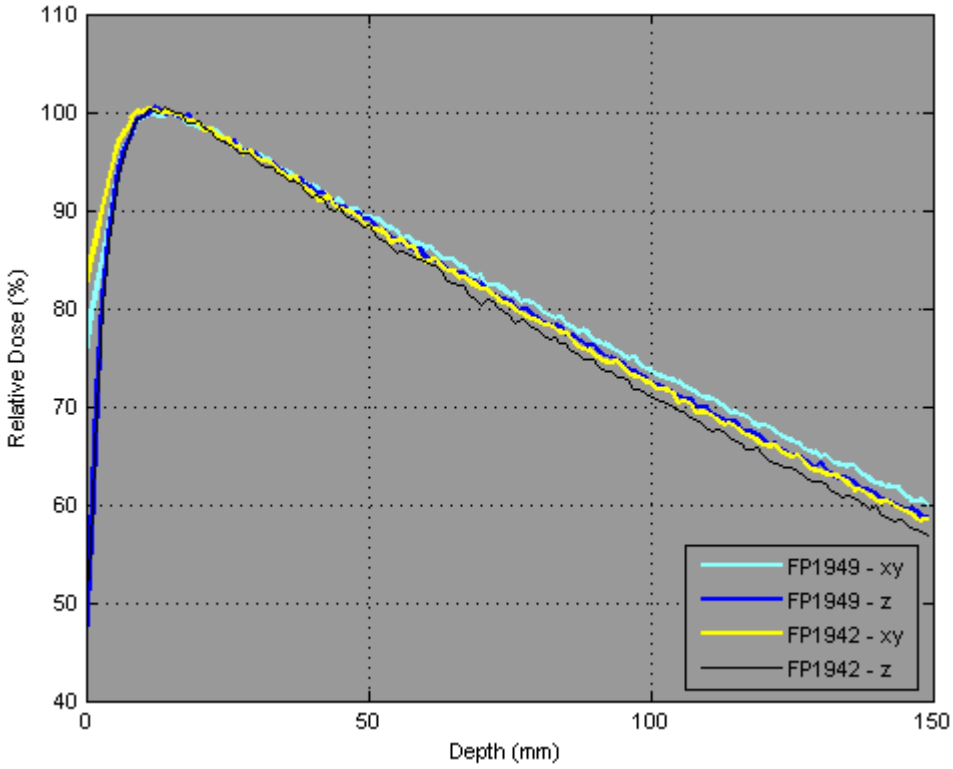

Figure 7: Diode depth dose response comparison. Relative dose responses to a 6 MV photon beam from two diodes sampling through a depth in water of 150 mm in two orientations each. "- xy" denotes the use of the diode orientated in plane orthogonal to CAX, while "- z" indicates the diode orientation was parallel to CAX. The lines connect the data points. The data is normalised to 100% at 15 mm depth for each curve.

Note that the “z” and “xy” suffix indicate the direction to which the diode points relative to the beam CAX. Hence, “z” and “xy” relate to orientations (1) and (2) respectively, as defined in the previous chapter. Each dataset is normalised to 100% relative dose at 15mm depth. The overall trend is similar for each response curve – the characteristic build-up region, followed by gradual decline in measured relative dose through depth. However, we observe a difference in response due to both diode, and diode orientation, most markedly in the build-up region, but also increasingly through depth thereafter.

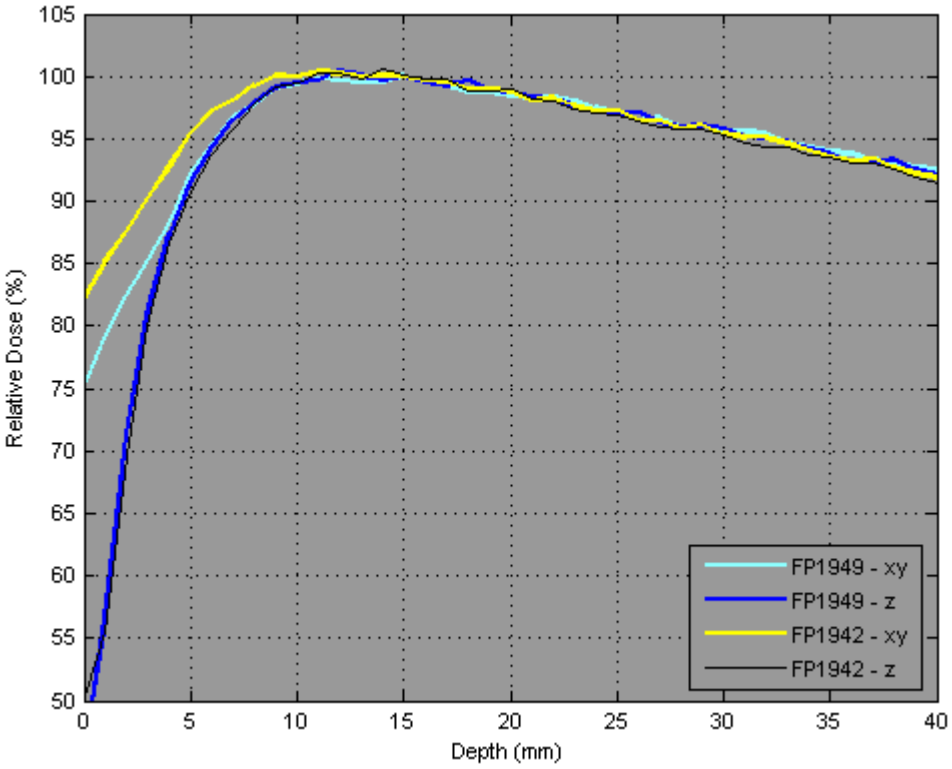

Figure 8: Closer diode depth dose response comparison. Here the percentage depth dose data is shown in the depth range: 0 to 40 mm. We are specifically concerned with diode responses for depths: 5, 10, 15, 20, 25, 30, 35 mm.

Diode FP1942 oriented parallel to CAX (shown as the black curve) is the clinically accepted diode, and orientation thereof, for measurement of 6 MV photon beams. Figure 8 shows how the four combinations of diode/orientation compare within the depth range relevant to this investigation. Figure 9 shows how the uses of the non-standard

combinations of diode/orientation absolutely differ from the depth response of diode FP1942-z within the depth range 0 to 40 mm.

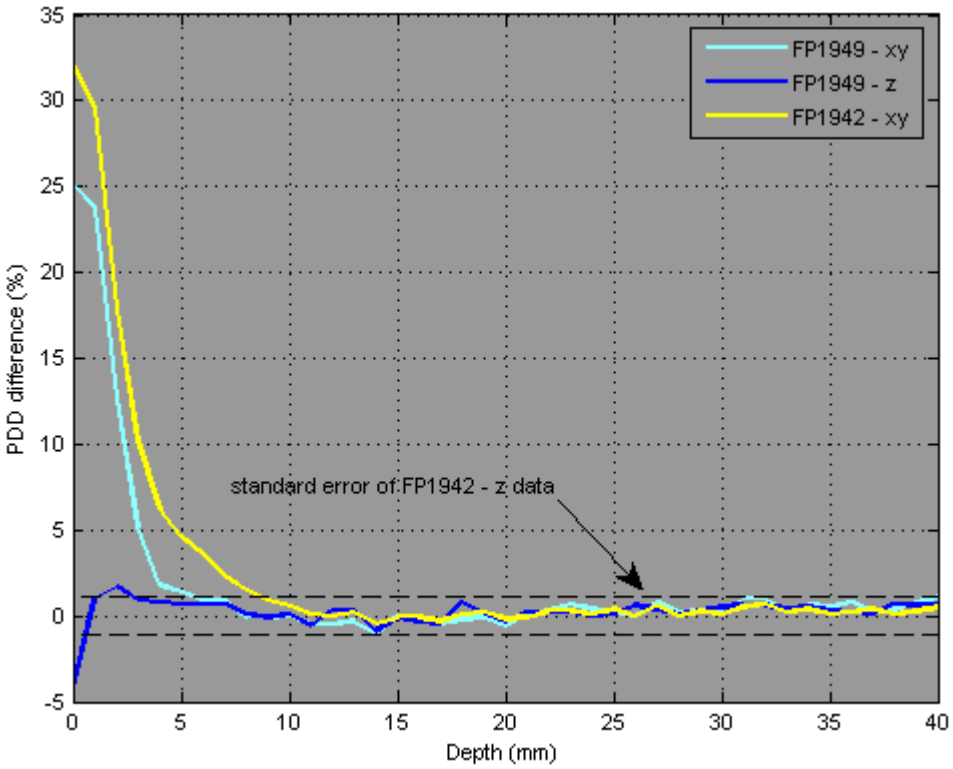

Figure 9: Diode depth response difference comparison. The FP1942-z depth percentage depth dose data are subtracted from the other diode percentage depth dose data. The dashed lines show the standard error of the depth response curve from the FP1942–z. The comparison is shown to a depth of 40 mm and the lines connect the data.

Figure 9 shows that the non-standard diode measurement modes respond within the standard error of FP1942-z for the depth range 8 to 40 mm. At shallower depths however, FP1942-xy deviates significantly – up to 32.1% at the water surface, while FP1949-xy over-responds by 25.1% at this point. Table 3 shows the differences in depth response for the non-standard diode modes relative to FP1949-z, for intervals of 5 mm, between the depths 5 to 35 mm. The depth response values are subject to an uncertainty of ±0.05%, and the positional uncertainties are ±0.05 mm.

Table 3: Depth response differences at selected depths relative to FP1942-z

Depth (mm)	5	10	15	20	25	30	35
FP1949-xy	1.4%	0%	0%	-0.6%	0.2%	0.3%	0.5%
FP1949-z	0.7%	0.1%	-0.1%	-0.3%	0.1%	0.5%	0.3%
FP1942-xy	4.6%	0.6%	-0.1%	-0.2%	0.4%	0.1%	0.1%

3.2 Film Sensitometry

A study was conducted to assess the OD response of the available RG film to varied amounts of delivered MU from both (10×10 cm^2, 98.5 cm SSD) 6 MV photon, and (10×10 cm^2, 100 cm SSD) 6 MeV electron clinical beams under 15 mm build-up material. Figure 10 below presents the results from this study. The data points for the two beam modes are the average of four OD measurements sampled from each MU field exposure, with the film background subtracted. Also shown, is the mean OD for each pair of averaged OD measurements:

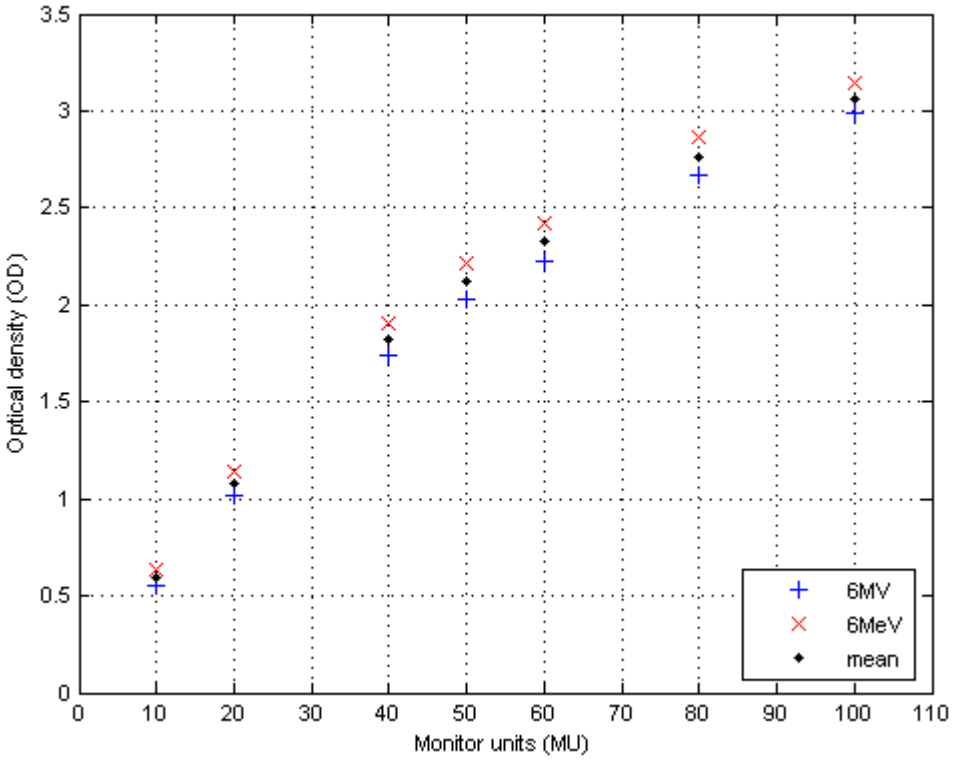

Figure 10: Sensitometry data for 6 Mev electrons and 6 MV photons under 15 mm build-up. Shown is the background-subtracted OD measurements from radiographic film exposed to a range (10 to 100) of MU deliveries from both beam modalities considered in this investigation. The mean between each pair of data points is also shown.

In order to build a sensitometric translation function, an exponential curve was fitted through the data. Figure 11 shows the curve, equation, and correlation coefficient for the fit to the mean sensitometry data:

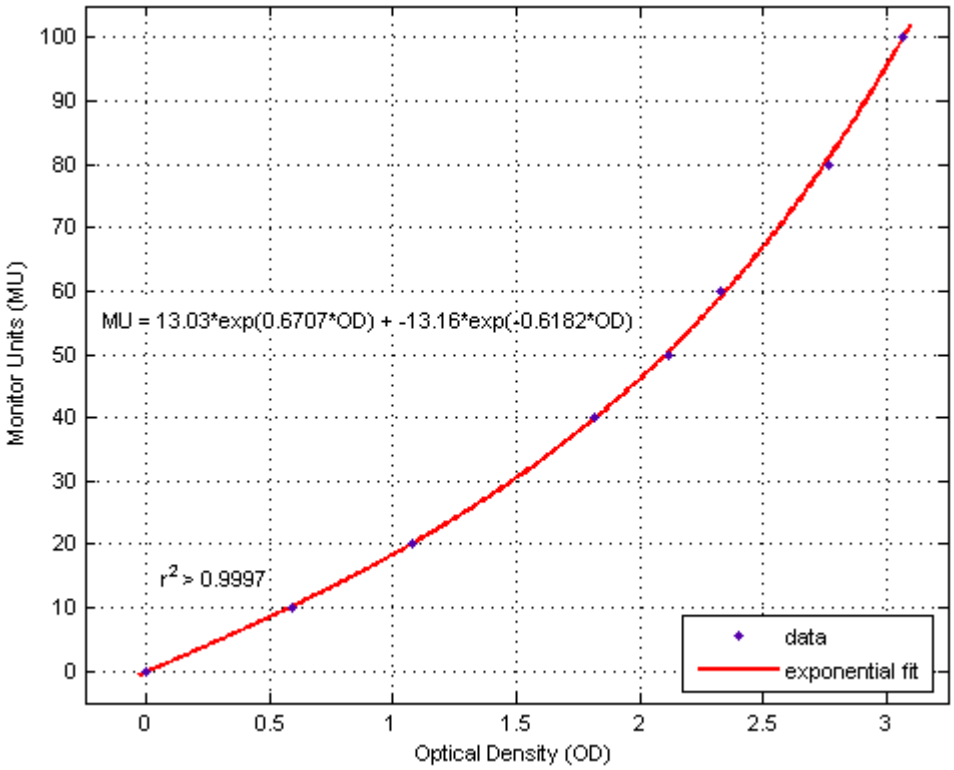

Figure 11: Exponential interpolation of experimental sensitometry data. The red line shows the exponential fit to the mean sensitometry data considered in the previous figure. Here we found a correlation coefficient greater than 0.9997.

The resulting translation function for use in subsequent film dosimetry script files (see Appendix B.1.11) is shown here:

$$MU = 13.03e^{(0.6707A)} - 13.16e^{(-0.6182A)} \qquad (1)$$

Here "A" is the measured absorption of the film expressed in units of optical density (OD).

3.3 Combined dosimetry in the MATLAB® workspace

Relative dose scans were performed in a Wellhofer water-tank using diode FP1949. For the 6 MV photon beam the diode was orientated orthogonal to the beam CAX, for the 6 MeV electron beam the diode was orientated parallel to the beam CAX. Exported from the Wellhofer system, these arrays consisted of 167×167 entries for the 50×50 mm^2 physical scan areas, meaning we obtained a data resolution of 3.34 entries/mm in both dimensions. The relative dose arrays were then combined using MATLAB® to yield simulations of dosimetry for varied abutment conditions. Scaling the relative dose range [0 180] to [0 1] over 256-bits, the data could be exported from the MATLAB® workspace for viewing as Portable network graphics (PNG) format. Figure 12 below shows an example of a composite dosimetry array at 15 mm depth in the abutment region of the 6 MeV electron beam and a 6 MV, MLC-defined, photon beam.

Figure 12: Portable network graphics (PNG) image of a composite relative dosimetry array. This 167×167 array represents combined relative dosimetry of a 50×50 mm^2 area at 15 mm depth under a 6 MeV electron beam at 110 cm SSD and a 6 MV photon beam at 98.5 cm SSD. The photon field is defined by MLC approximating an edge at 45° to the beam inplane axis. Darker areas represent lower relative dose. For this example the gap between the electron field edge and the MLC mid-leaf points at the water surface is -0.1 mm.

Additionally, relative dose profiles were extracted from each array. These profiles were extracted perpendicular to the field abutment edges, and sampled across three locations of an MLC leaf. Figure 13 below depicts profiles extracted from the relative dose arrays – both before and after combination. Two pertinent dosimetric issues can be easily seen here. Firstly, the difference in the beam edge gradients of 6 MeV electron 6

MV photon beams. And secondly, the potential variation in combined dosimetry as a function of how the MLC is employed.

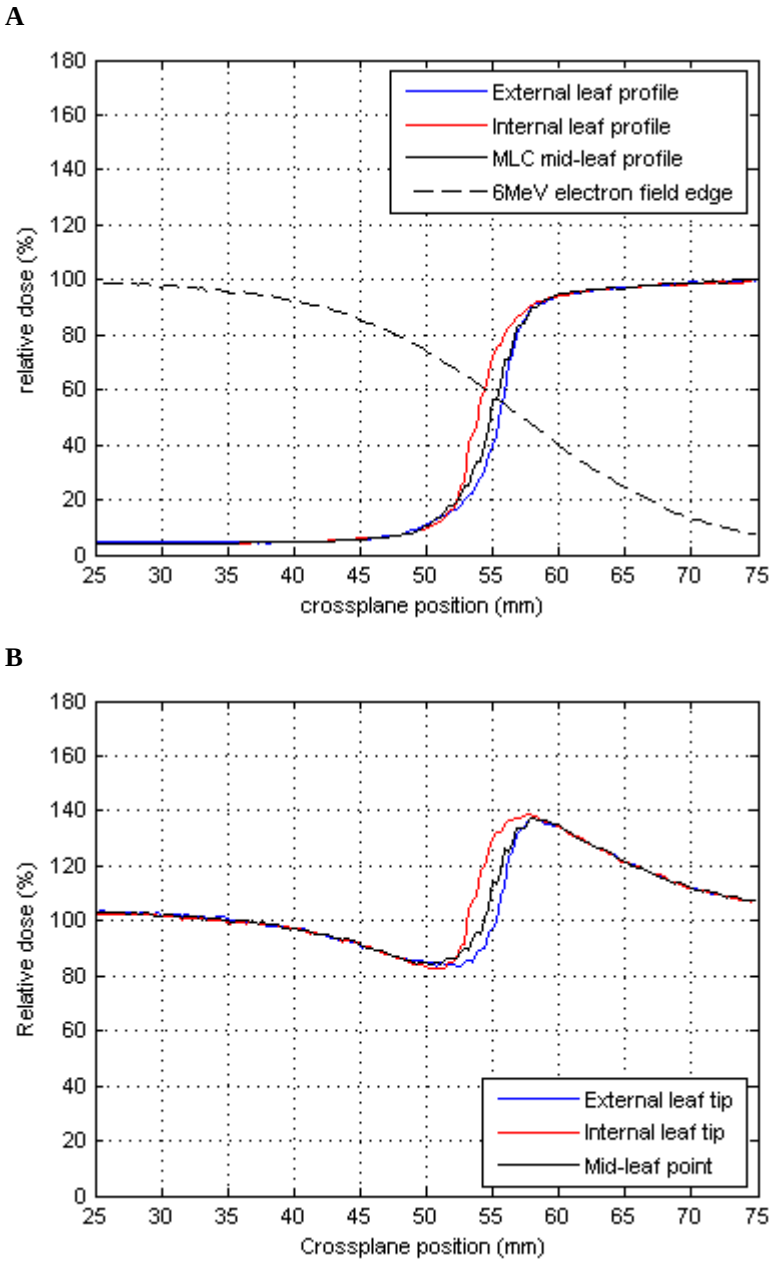

Figure 13: Intra-leaf profiles at d_{max} for a surface abutment gap of -0.1 mm. Shown are the field edge relative dose profiles of the 110 cm SSD 6 MeV electron beam, and the 98.5 cm SSD MLC-defined 6 MV photon beam – positioned relative to the electron beam CAX before combination (A), and after combination (B). The MLC angle approximates 45° to the photon beam inplane axis. The red and blue lines indicate profiles sampled through either edge of an MLC leaf.

The complete dosimetry dataset consists of 2415 arrays being: 7 scan depths of 5 photon shielding angles for 69 variations of abutment gap. Figure 14 below presents profiles resulting from eight of these gap variations; outlining the range of abutment gaps considered in this investigation. The profiles in Figure 14 results from the composite data of a 6 MV photon field edge, defined by MLC approximating 45 to the photon beam inplane axis; combined with the 6 MeV electron applied over the extended SSD. Note that for other shielding angles, the surface abutment gaps differ slightly per iteration since the photon datasets are aligned at 15 mm depth. The differences in geometrical divergence perpendicular to each angled shielding edge results in non-co-registration of the surface abutment scales. Wherever possible we present data in terms of surface field abutment gap.

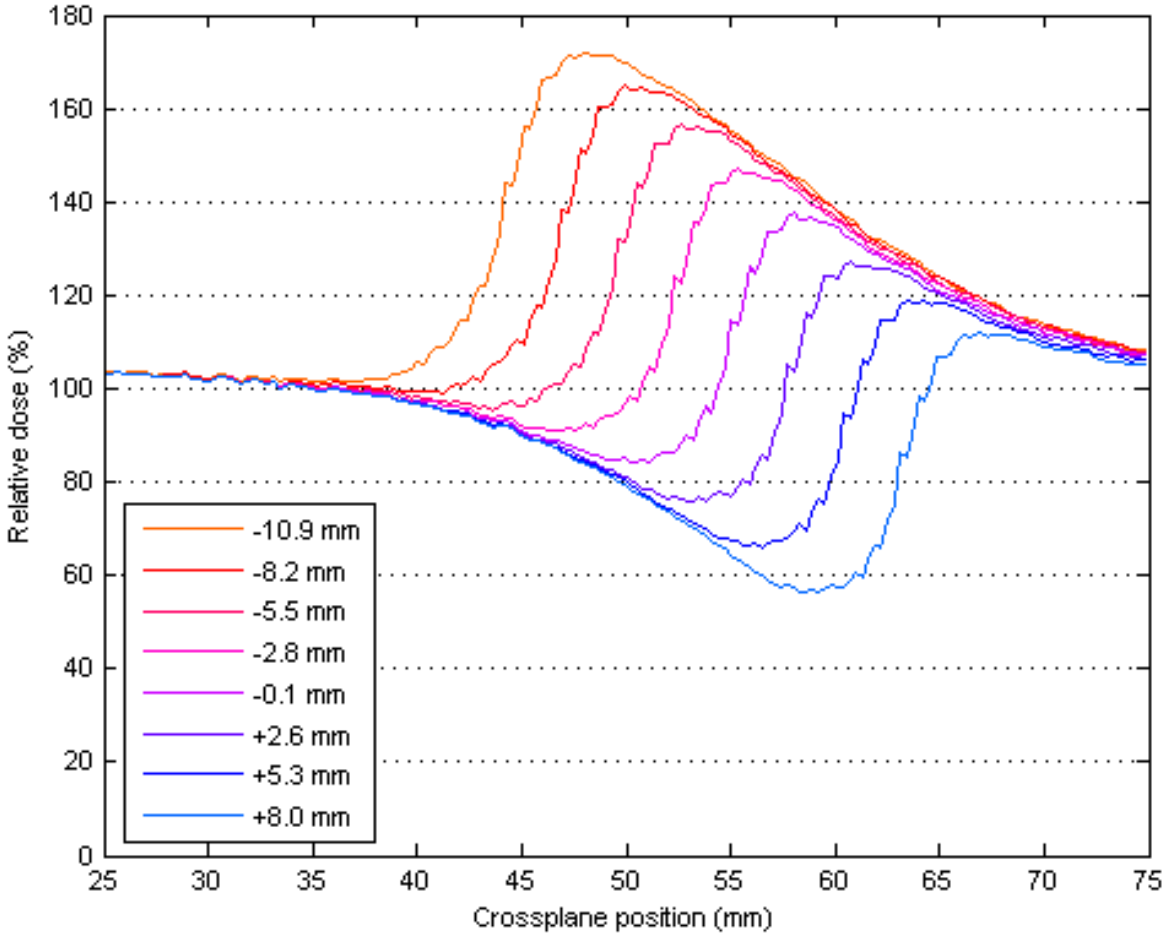

Figure 14: Mid-leaf relative dose profiles at d_{max} for selected abutment gap conditions. Starting with a field overlap of 10.9 mm, eight iterations of a composite dosimetry volume are made over intervals of 9 × 0.3 mm, covering most of the surface abutment gap range explored in this study. Profiles here are sampled from composite dose volumes involving photon scan data under MLC shielding at 45° to the beam inplane axis, combined with extended SSD electron scan data. The lines connect the data.

3.4 Visualising the volumetric dosimetry

VTK proved useful for visualising the relative dose data. Here we built a "widget" that was able to interrogate the dataset in the "XYZ" planes as shown in Figure 15 below. Another widget was developed to map a user-defined value isosurface through the dataset, this is also displayed in Figure 15, and represents the 6 MV photon beam edge as defined by the 45° (saw-tooth) MLC shielding. The planes outlined in red, yellow, and blue represent the x, y, and z planes respectively; which in terms of abutting with the 6 MeV electron beam would be through the IP, CP, and depth directions, relative to

the electron beam CAX. These two visualisation methods demonstrate just how well the dosimetric heterogeneity due to the MLC stepping actually corresponds to that expected, based on geometrical argument. We also observe the slight inward divergence of the photon beam edge due to the field positioning relative to the CAX.

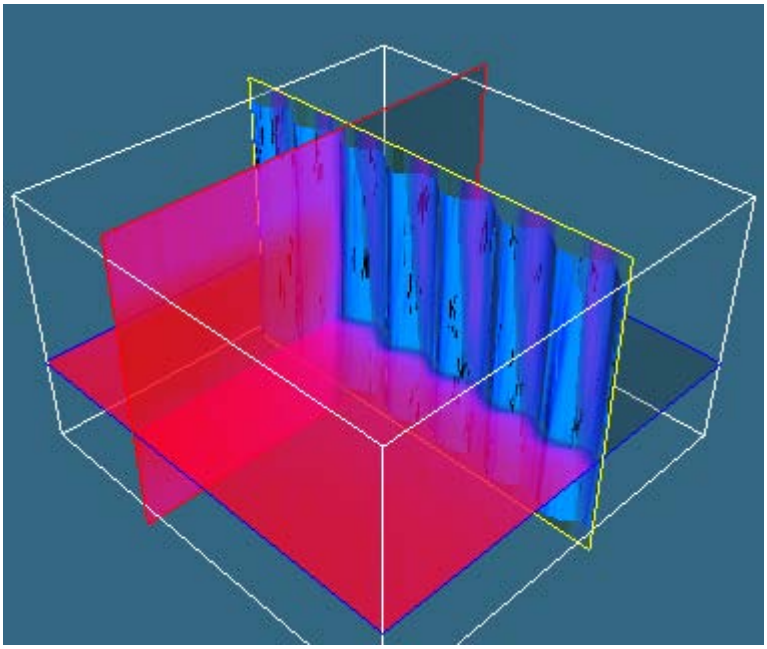

Figure 15: VTK representation of MLC photon beam data. This PNG image is imported from the VTK GUI and shows the combination of both the XYZ plane and isosurface interrogation methods. Here, for the XYZ widget, the relative dose values are run through a lookup table whereby higher doses correspond with red and lower doses correspond with black; an alpha channel controls the transparency. The "rippled" surface represents the 50% isodose – being the definition of the photon beam. The red, yellow, and blue outline the planes in x, y, and z (depth) respectively.

3.5 Film Dosimetry

To qualitatively check the abutment dosimetry results obtained via array combination in the MATLAB® workspace, RG film was exposed for two selected abutment conditions and the dosimetry results compared. Figure 16 below is a PNG image of an RG film scan depicting the layout of the abutted photon and electron fields at 15 mm depth under solid water, with a abutment gap of -7.5 mm (field overlap).

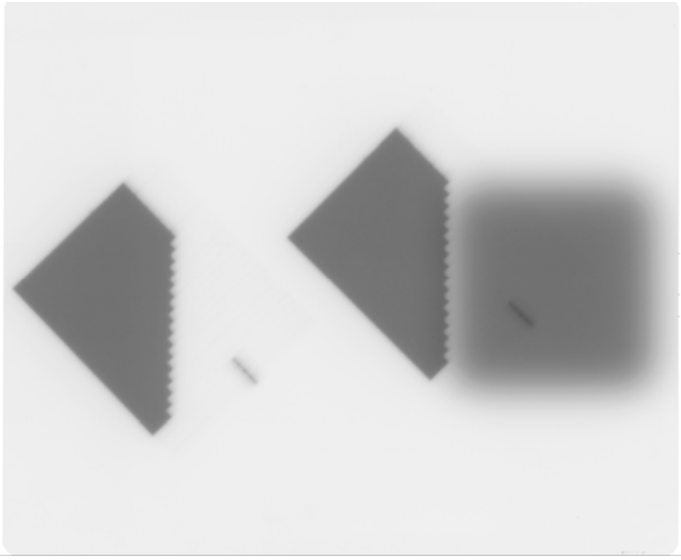

Figure 16: Scan of RG film. Field exposures to an extended SSD 6 MeV electron beam and two identical 6 MV MLC-defined photon fields with 15 mm build-up. Darker areas represent higher exposure. Here the abutment gap is -7.5 mm (field overlap) at 15 mm depth. The un-abutted photon field is used for profile normalisation.

This experimental setup was repeated for an abutment gap of +6.0 mm at 15 mm. The photon fields were located under 98.5 cm SSD + 15 mm build-up, and received 40 MU. The electron field was exposed to 52 MU (see Appendix A) at 110 cm SSD + 15 mm build-up, under a 10×10 cm^2 cone applicator. Using the sensitometric translation function previously determined, the OD profiles were converted to MU profiles, and then normalised so 40 MU = 100% relative dose. See Figure 17 below for film profile and translation results.

A

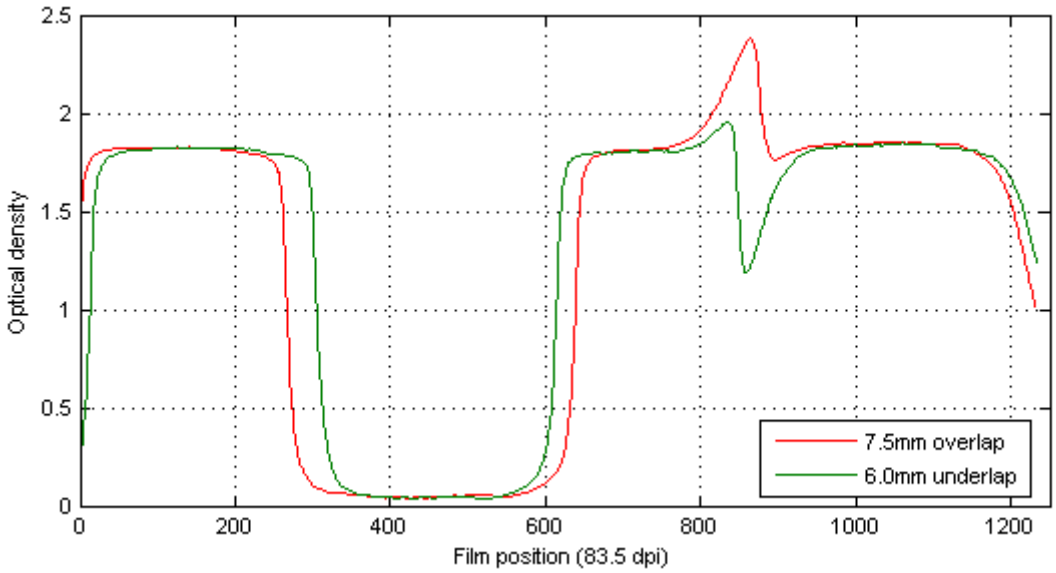

B

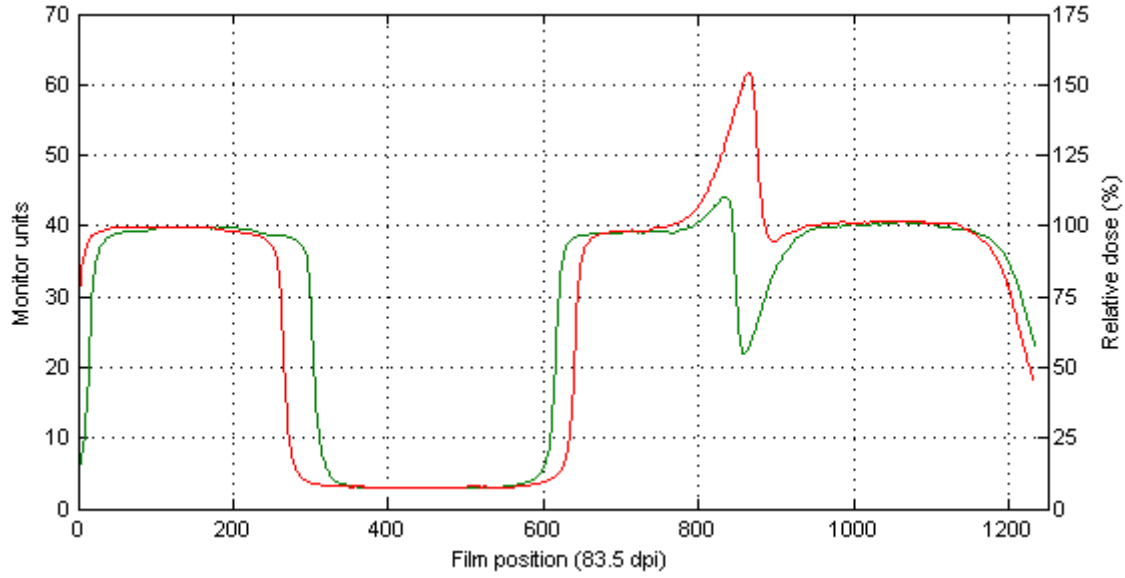

Figure 17: Film profiles of selected abutment gaps. Shown here is the OD profiles (A) taken from RG film exposed to two abutment gap situations: -7.5 mm (field overlap) as the red line, and +6.0 mm (field underlap) as the green line. Also shown is the sensitometric translation of the OD profiles (B). The lines connect data points. No profile registration is made in the positional direction.

3.5.1 Dosimetry comparison

The MU profiles were normalised and sections were extracted from across their respective abutment region. These provided comparison for the relative dose profiles as measured in the Wellhofer water-tank dosimetry system and combined in MATLAB®. Figure 18 (A) below shows the sections of translated film profiles (dashed lines) as registered to the MATLAB®-combined profiles (solid lines).

Here we see a good agreement in general trend, though the Wellhofer profiles consistently present higher relative dose values than the film profiles, across the abutment region. Notably, the film profiles tend to 100.1% and 101.0% for the under lap and overlap respectively as the CP position tends towards the electron CAX, whereas the combined Wellhofer profiles both tend to 103.1%. Figure 18 (B) illustrates the relative dose profile differences between the MATLAB®-combined Wellhofer water-tank data and the sensitometrically translated film data, for the two abutment gaps considered in this case.

Dosimetry method differences of 12.2% are present for the underlap condition, and 10.7% for the field overlap condition. The profiles agree within 5% relative dose for 55% and 81% of the positional range for the overlap and underlap data respectively. The standard errors of the means, for each abutment gap profile across the positional range considered, are: 2.2% and 1.8%, for the overlap and underlap conditions respectively.

A

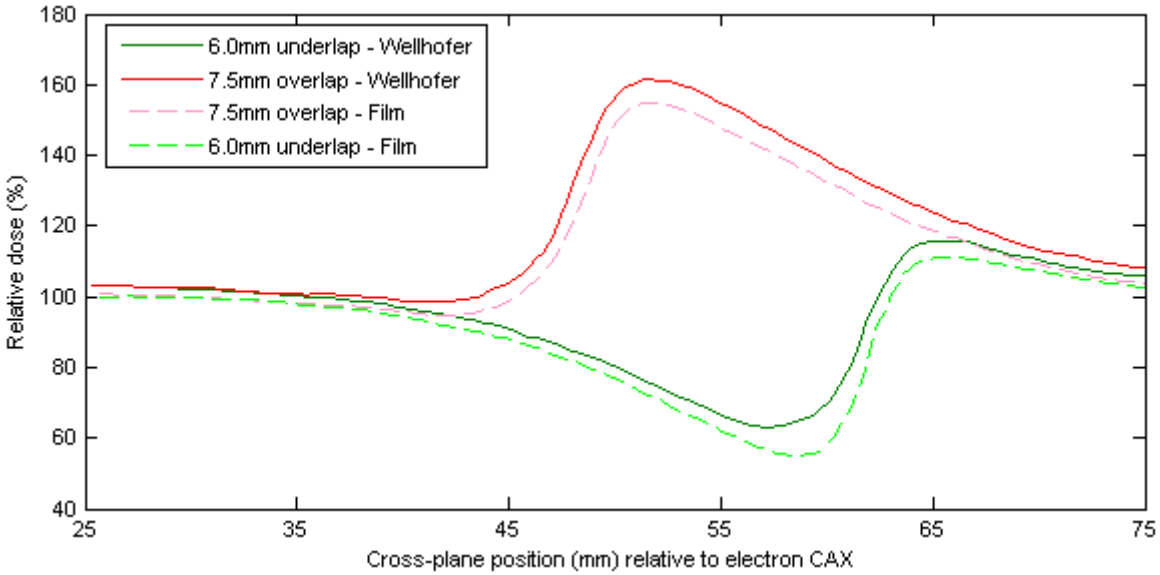

B

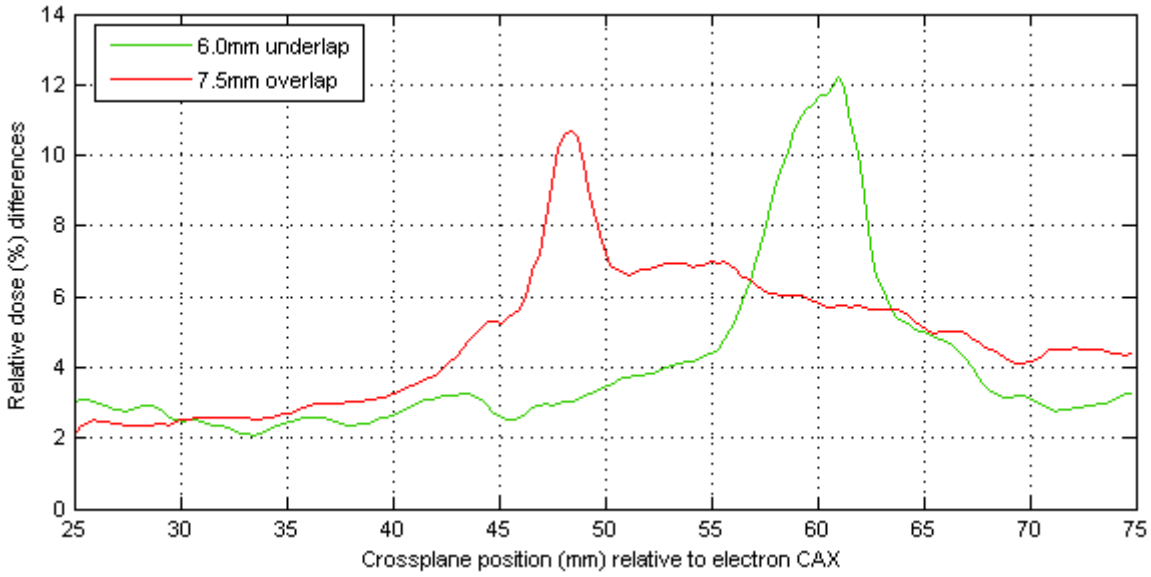

Figure 18: Dosimetry method comparison – Wellhofer vs. film. Shown are profiles extracted from the MATLAB®-combined water tank scans as compared with 50 mm sections of the sensitometrically translated profiles extracted from RG film, for two abutment gap situations – 7.5 mm overlap & 6.0 mm underlap (A). Relative dose profile differences between Wellhofer and RG film (B). The sensitometrically translated RG films profile data is subtracted from the MATLAB® -combined Wellhofer water-tank scan data for two abutment gap situations. The lines connect the data. Here the film profile maxima are positionally registered to the Wellhofer scan maxima.

3.6 Beam edge inspection

An analysis was made to determine dosimetric characteristics of the photon and electron beam edges. Measurements of penumbral width were made for the 6 MV photon beam as defined by the MLC or Cerrobend®. Effects of using an extended SSD electron beam were quantified by comparing penumbral width data and PDD curves for the standard and extended SSD beams.

3.6.1 6 MV photon beam penumbra

Figure 19 below presents isodose contours across the 6 MV beam edge as defined by 30° Cerrobend® (A) and 30° MLC (B). The 20%, 80%, and 100% isodoses are labelled. The beams are geometrically registered at d_{max}, meaning that the optics, and therefore 50% isodose, is positioned laterally identically at 15 mm depth. The two beams have the same geometrical divergence. The choice of shielding has a significant effect on the mean lateral separation of the 20% and 80% isodose lines through depth 5 to 35 mm.

We measured this lateral separation at the seven depths, for all MLC angles, and the Cerrobend at 30°. These results are shown in Figure 20 below. For all shielding angles and shielding type, there is an apparent minimum average penumbral width at 10 mm depth, with an overall trend of larger widths at greater depths. However, the choice of shielding angle and type also influences the average spread of the photon beam penumbra. Larger MLC angles correlate with larger mean isodose separations, while the beam defined by Cerrobend® has significantly lower beam edge spread than any of the MLC-defined beams. At 10 mm deep the penumbral width of the 30° MLC is about 1.5 times larger than that of the 30° Cerrobend®, and this ratio does not vary significantly at the other depths.

A

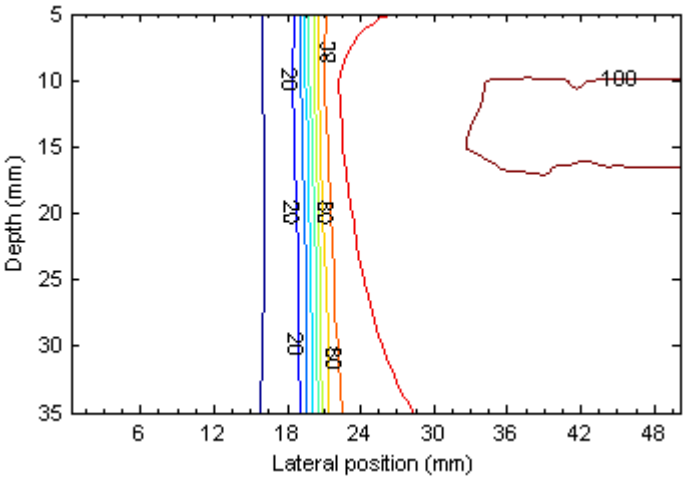

B

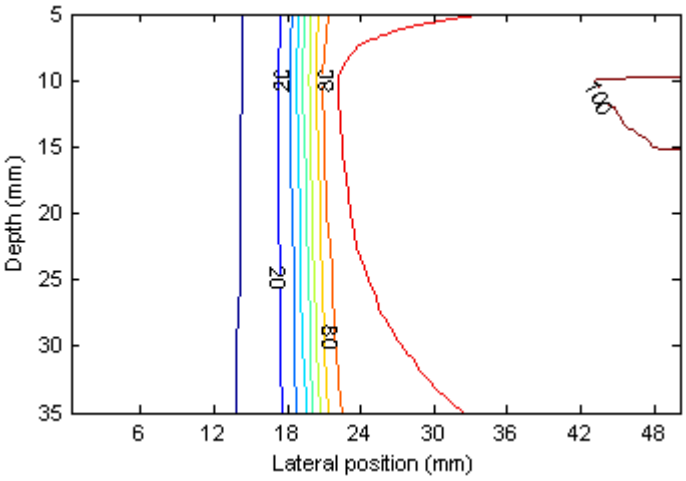

Figure 19: Isodoses across photon beam edges. Contour maps of isodose values from 10% to 100% relative dose under the beam edge of a 6 MV photon beam defined by Cerrobend (A) shielding at 30° to the inplane axis, and MLC (B) at 30° to the inplane axis. The data are shown for the depth range of 5 to 35 mm, and a lateral range of 0 to 50 mm. The 100%, 80%, and 20% isodoses are labelled.

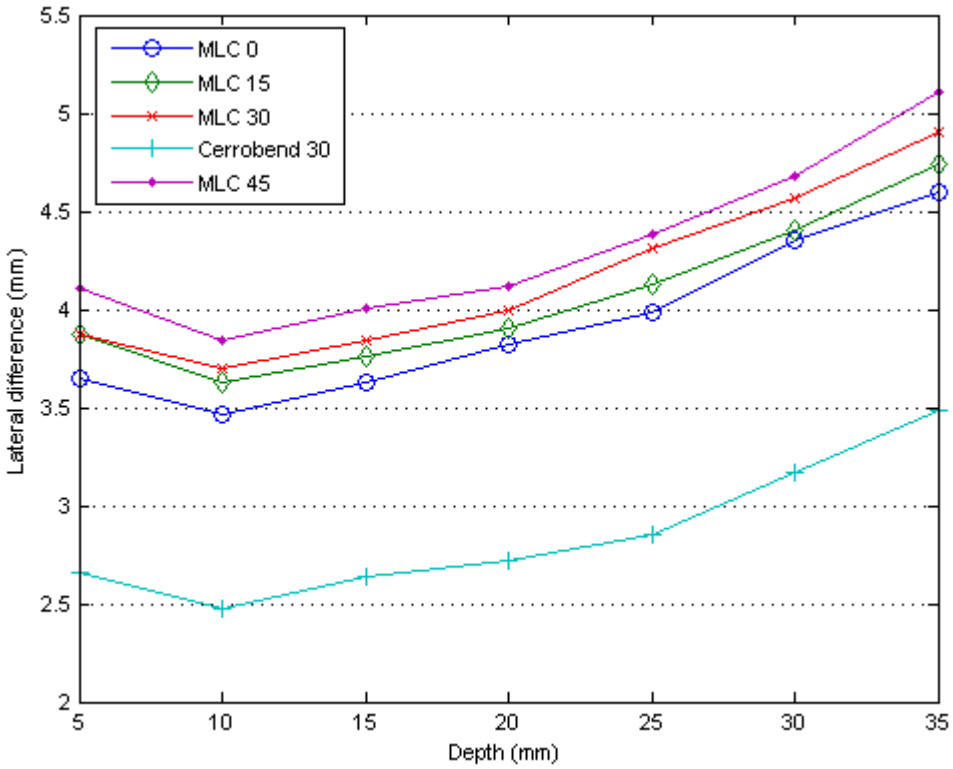

Figure 20: Penumbral widths for 6 MV photons. Shown is lateral separation between the mean location of the 20% and 80% isodoses over the depth range 5 to 35 mm, for the four MLC angles, and the Cerrobend shielding at 30° to beam inplane axis. The lines connect the data.

3.6.2 Comparison of MLC with Cerrobend®

The dose inhomogeneities resulting from the use of MLC as compared to Cerrobend® were investigated. A subtraction of the 30° Cerrobend® relative dose volume from the 30° MLC relative dose volume was made. Figure 21 and Figure 22 below show the results of this subtraction in terms of greyscale and meshgrid images respectively, for the scan data at 15 mm depth. The greyscale range is set across the extent of the data range which is not symmetrical across zero, however the light and dark areas are indicative of hot and cold MLC dosimetry relative to the Cerrobend® data. The meshgrid surface represents the relative dose differences as colour, and height along the vertical axes.

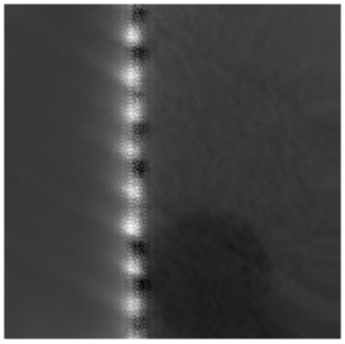

Figure 21: Subtraction image of MLC dose inhomogeneities. The Cerrobend® photon beam data at 15mm depth is subtracted from the MLC data. Both shielding types used make 30° to the IP axis and are laterally located equivalently within the photon beam. Darker areas represent larger cold areas, lighter areas represent larger hot areas.

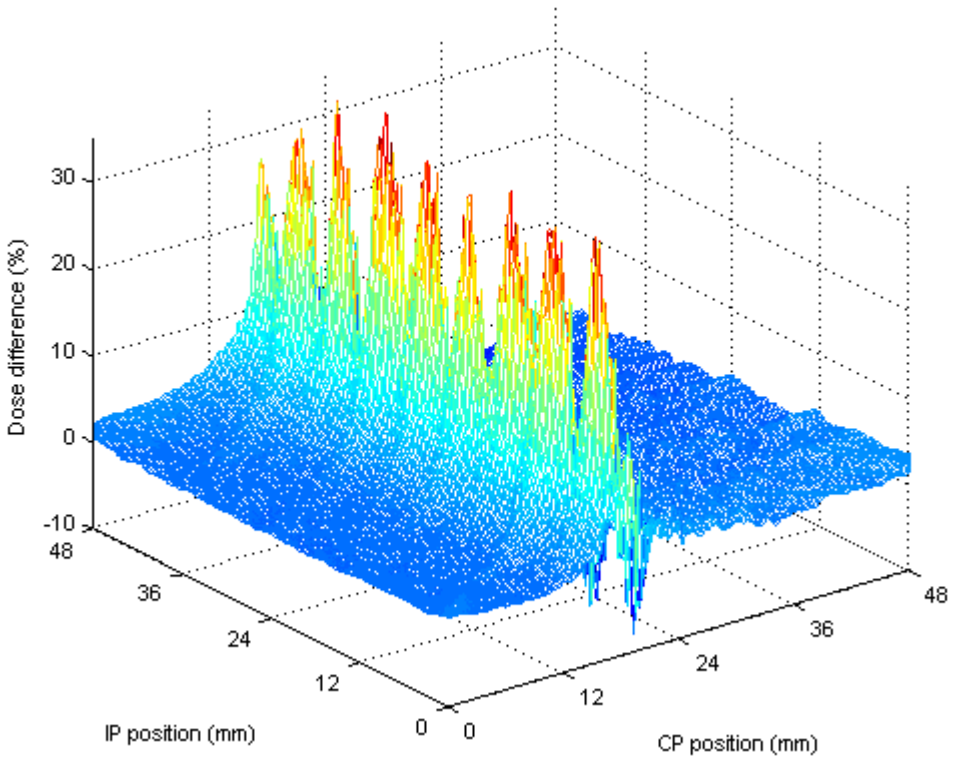

Figure 22: Meshgrid image of MLC dose inhomogeneities at 15 mm depth. The Cerrobend® photon beam data is subtracted from the MLC data. Both shielding types used make 30° to the IP axis and are laterally located equivalently within the photon beam. The vertical axes and colour represent the dose differences over the lateral scan-subtraction plane.

Both figures show an asymmetry in hot/cold difference magnitudes for the use of MLC instead of Cerrobend®. An increased relative dose of 30% to 35% at the internal MLC leaf tip areas is common along the shielding edge. The coldspots at the external leaf tip areas rarely go below 10% (relative dose) of that of the Cerrobend® data. A 3D visualisation of this subtraction data through depth is shown in Figure 23 below.

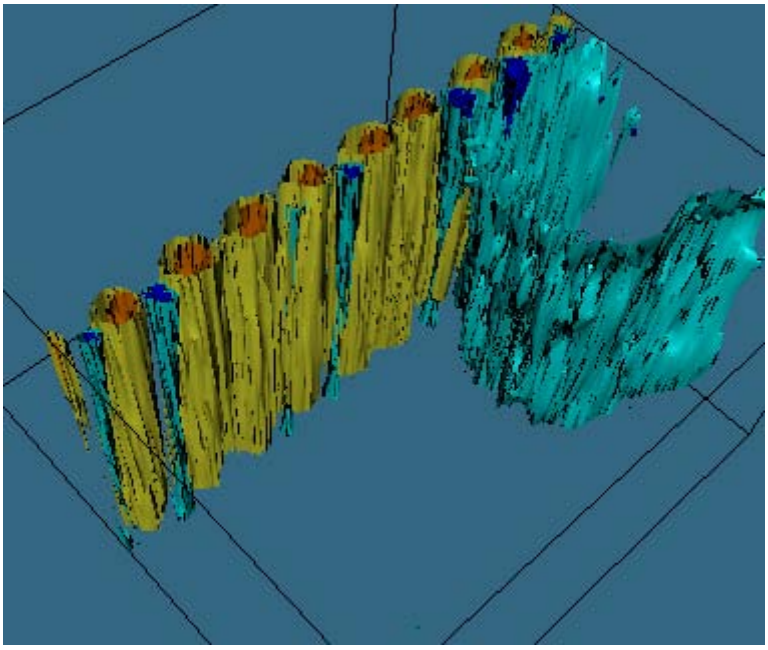

Figure 23: VTK image of dose-volume subtraction data. The 30° Cerrobend® photon beam data is subtracted from the 30° MLC data. The dark blue, light blue, yellow, and orange isosurfaces represent relative dose differences of -8%, -4%, +10%, and +20% respectively; as spatially located within the scan data. The view is obliquely through depth from 5 mm to 35 mm. The black lines indicate the spatial extent of the data.

Here we easily see that the MLC produces regions throughout the volume depth that are significantly hotter or cooler than the dosimetry under Cerrobend® shielding. The yellow and orange surfaces represent isodoses that are hotter by 10% and 20% relative dose, respectively. These regions are under the Cerrobend® shielding, but due to the stepping of the MLC, are left exposed to the primary photon beam. The surfaces in blue represent regions that receive less dose from the MLC regime than the under the Cerrobend® regime. These include regions along the MLC shielding beam edge under the external leaf tips. Again we see that there is significantly more hot, and hotter regions, than the

cold regions, and magnitudes thereof. An interesting feature of this figure is the large cylindrical structure present on the right hand side of the image. It is also present in Figure 21 if one looks closely. The artefact is due to the equipment used for mounting the Cerrobend® shielding blocks – a Perspex plate of 5 mm thickness with 12 mm diameter holes drilled in it for bolting the block. These holes contribute to a photon transmission non-uniformity across the plate, leading to a measurable increase of relative dose of around 5%.

3.6.3 6 MeV electron beam

The dosimetric effects associated with extending SSD for 10×10 cm^2 6 MeV electron beams were investigated. We compared both PDD curves and crossplane profile data for 100 cm and 110 cm SSD's. Figure 24 shows the PDD data under the CAX for both SSD's considered to a depth of 40 mm. Both curves in graph A are normalized to 100% at 15 mm depth. The extended SSD has the greatest effect in the build-up region: between 1 and 2% less relative dose near the surface. However, there is a small effect of around 1% higher dose beyond d_{max}. Overall the differences are small with a mean of -0.0888 and standard deviation of 0.7811.

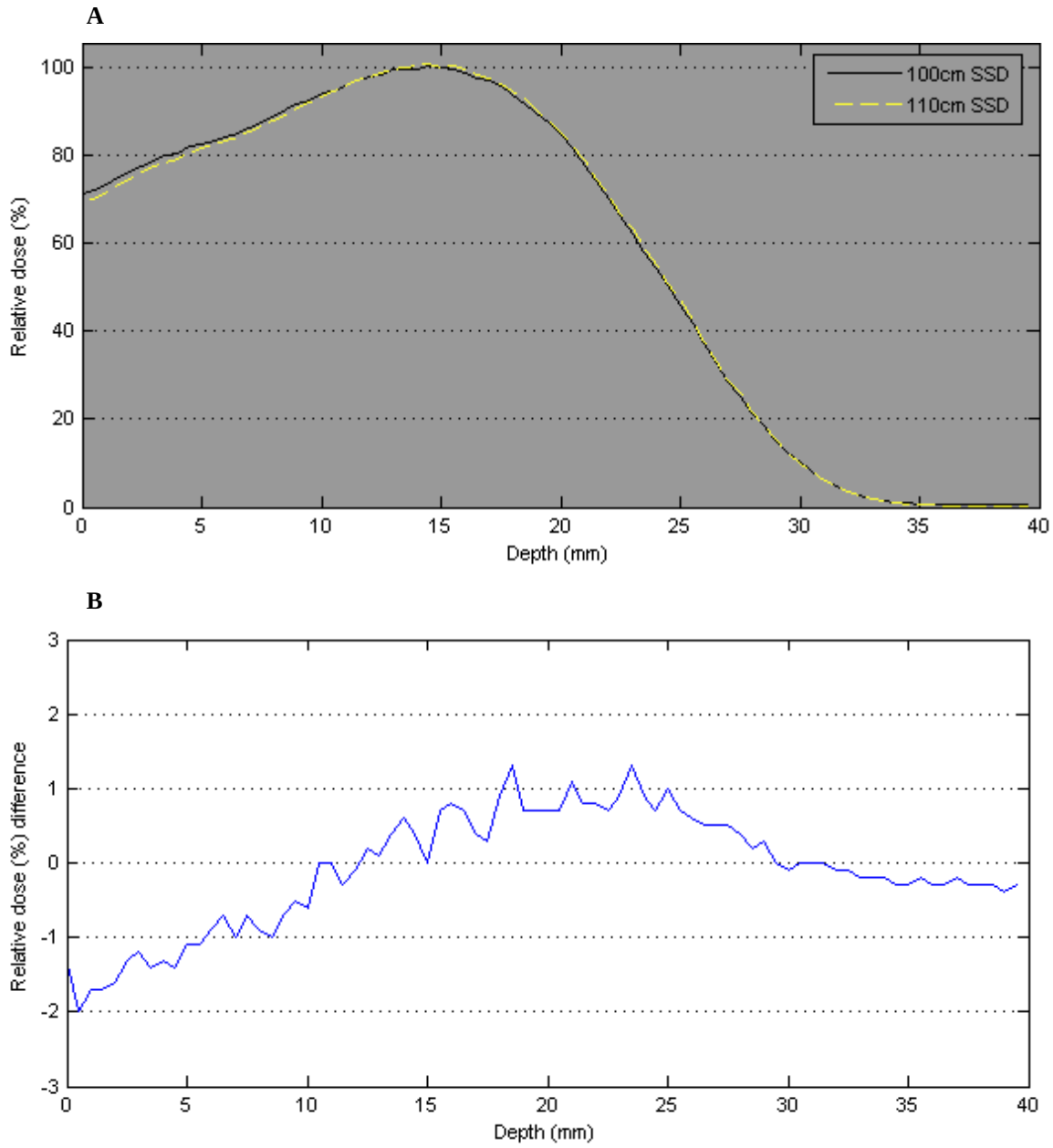

Figure 24: Percentage depth-dose data for 10×10 cm^2 6 MeV electron beam. PDD curves are shown for 100 cm and 110 cm SSD's (A). PDD data at the standard SSD are subtracted from that of the extended SSD data (B). The data were collected with the electron diode FP1949 to a depth of 40 mm. The lines connect the points.

We see a more dramatic effect from SSD variation on the electron beam profiles. Figure 25 below shows a relative dose profile at d_{max} from the CAX outward in the crossplane direction for a 6 MeV beam at 100 cm (solid) and 110 cm (dashed) SSD. The extended SSD profile has been scaled in the crossplane direction to account for beam divergence, and allow direct comparison with the standard SSD profile. As seen from the PPD curves, there are no major discrepancies between profiles at the CAX. However, the effects across the beam edge are significant – we observe a rounding and broadening of the beam edge profiles.

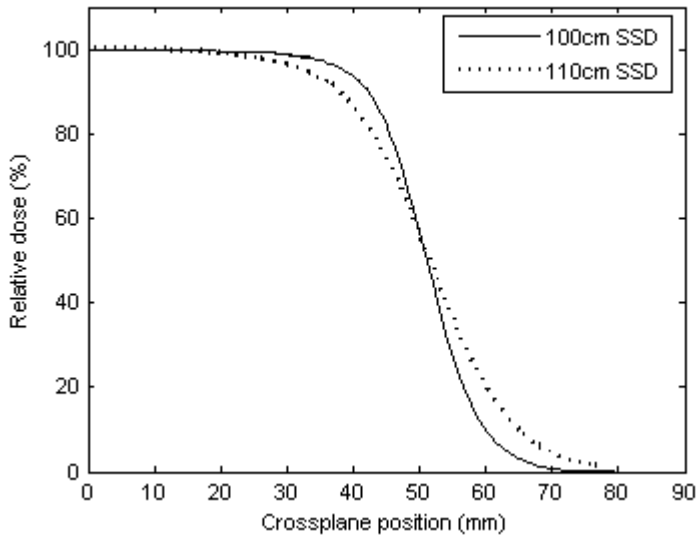

Figure 25: Effects of extended SSD on 6 MeV electron beam. Shown are relative dose profiles from the CAX to 90 mm crossplane at d_{max} under a 10×10 cm^2 6 MeV electron beam at 100 cm and 110 cm SSD's. The crossplane positions of the extended SSD profile have been scaled to account for beam divergence.

The lateral distance from the 80% to 20% isodoses were measured for profiles at selected depths under the standard and extended SSD setup conditions – see Figure 26 below. We observe a general increase in penumbral width at greater depths for beams of both SSD. Most notably, we see an increased penumbral width of around 9.3 mm wider (on average) between standard and extended SSD beams for the depth range 10 to 20 mm.

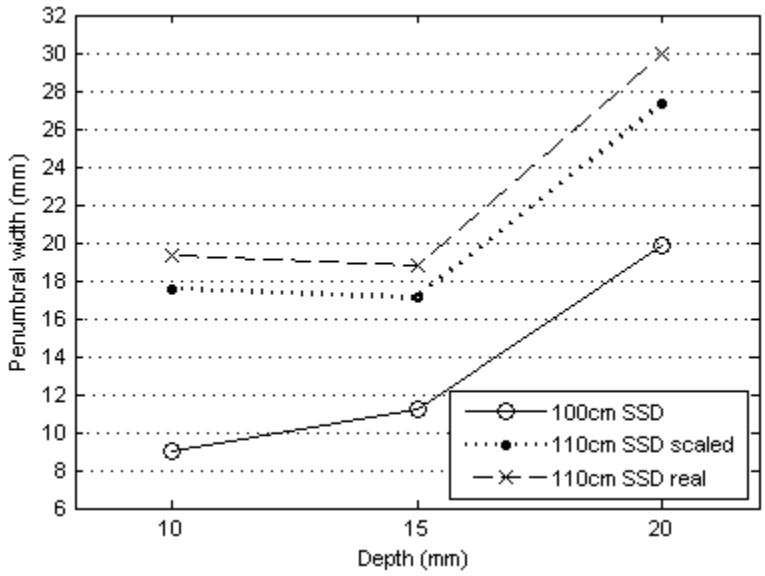

Figure 26: Penumbral widths for 6 MeV electrons at standard and extended SSD. Shown are the lateral separation of the 20% isodose to the 80% isodose from CAX for depths 10, 15, and 20 mm. The solid and dashed lines connect the standard and extended SSD data respectively. The smaller dashed line represents the penumbral widths under 110 cm SSD as projected back to 100 cm SSD for comparison.

3.6.4 TPS modelling of extended SSD electron beam

Measured electron beam edge data was compared to the half-beam profiles generated in the Pinnacle^3 TPS version 7.6c. Figure 27 presents this profile comparison for depths of 15 and 25 mm in water/phantom. At 15 mm depth, Pinnacle^3 agrees well with the measured data in the central and distal regions of the beam. There are significant differences in CP position around the 80% relative dose level. For 25 mm depth the discrepancy between profiles increases. Here the TPS appears to calculate a broader and rounder CP half-beam profile. For the TPS data at the 25 mm depth, the lateral position of the 40% isodose contracts, and the 10% isodose extends away, relative to the measured data.

Figure 28 below depicts the differences between the TPS and measured data at depths of 15 and 25 mm. Gaussian curves were fit to each profile (R^2 values ≥ 0.9998) and a subtraction made. An over 6% underestimation by Pinnacle is observed at 48 mm

CP for the 15 mm depth. Deviations of around ±3.5% are observed at the CP positions of 45 and 69 mm for the 25 mm scenario.

A

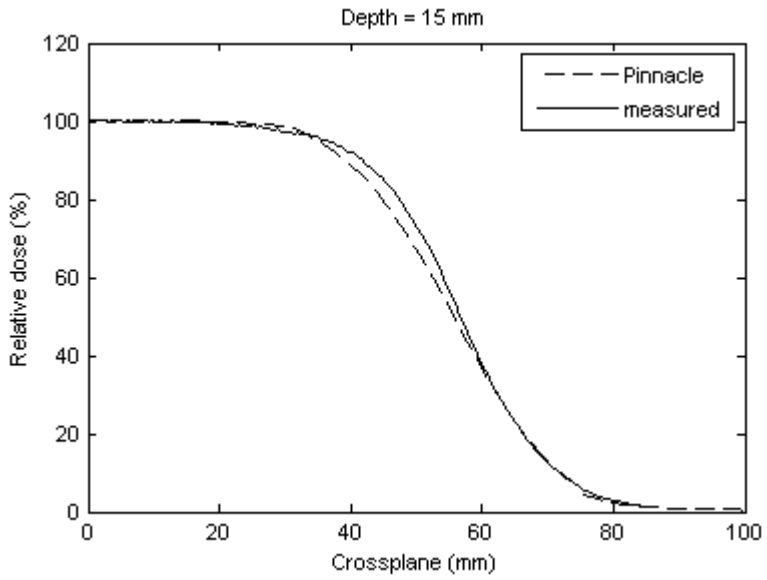

B

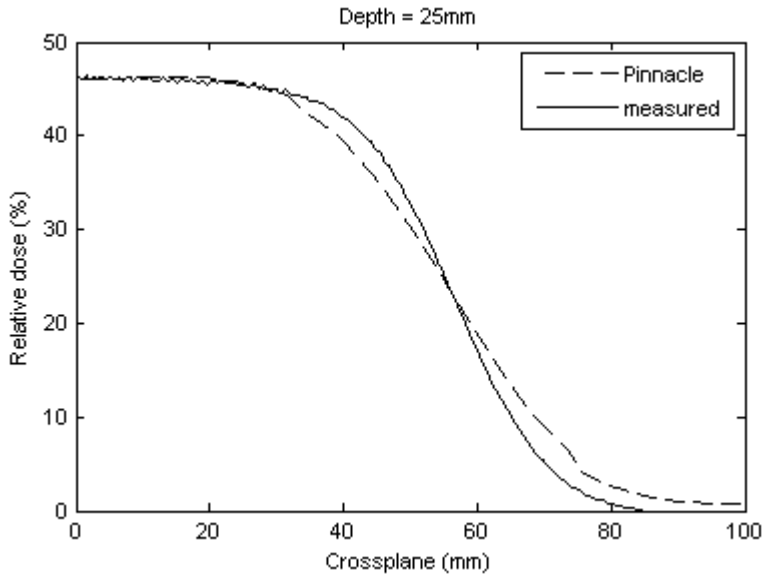

Figure 27: TPS modelling of extended SSD electron beam. Relative dose profiles sampled at 15 mm depth (A), and 25 mm depth (B), across the edge of 10×10 cm^2, 6 MeV electron beam applied at an extended SSD of 110 cm. The solid lines represent measured data, and the dashed lines represent the profiles generated in the Pinnacle^3 v7.6c TPS.

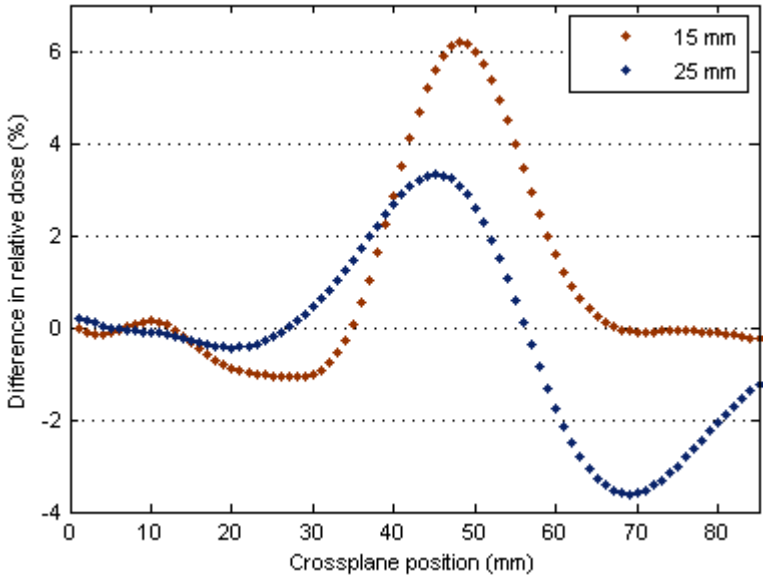

Figure 28: Difference between measured and modelled relative dose profiles across extended SSD electron beam edge at 15 and 25 mm deep. A Gaussian fit of the Pinnacle^3 data at each depth ($R^2 \geq 0.9998$) is subtracted from the respective Gaussian fit ($R^2 > 0.9999$) of the diode measured data. The data are presented for the CP range of 0 to 85 mm.

3.6.5 Visual comparison of the beam edge types

Using VTK we can spatially represent the 80% and 20% relative dose isosurfaces of the 6 MV photon and 6 MeV electron beams. Figure 29 below displays these representations, with the 80% isosurfaces in yellow, and the 20% isosurfaces as light blue. The spatial scales are equal. Both the dose fall-off with depth, and the penumbral widths of the 6 MV photon and 6 MeV electron beams (as detailed previously in sections 3.6.1 and 3.6.3) are clearly shown here to differ significantly.

A

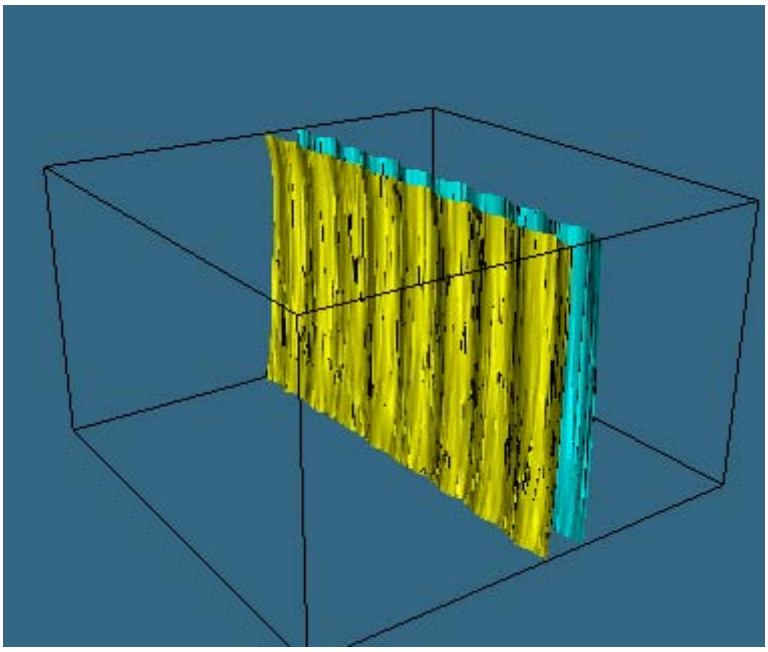

B

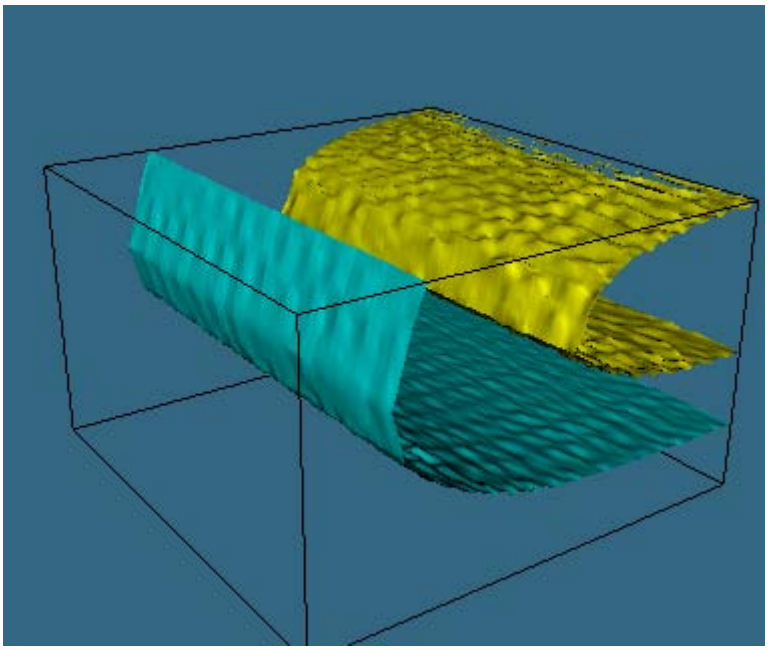

Figure 29: VTK representations of the beam penumbra. The 80% and 20% isodoses are shown as the yellow and blue surfaces respectively; for the 6 MV photon beam (A) and the 6 MeV electron beam (B). Here the MLC angle makes 30° to the IP axis. The black lines represent the spatial limits of the scan data. The vertical black lines are in the z (depth) direction over the range 5 to 35 mm.

3.7 Composite profile discrepancies

Profiles at 15 mm depth were extracted from twelve locations across each combined relative dosimetry array over the range of abutment conditions – gap size, and angle approximated by the MLC. The twelve locations consisted of profiles sampled from three locations on four arbitrary MLC leaves. The leaf locations were: external leaf tip, internal leaf tip, and the leaf mid-point. See Figure 13 (B) for example of profiles taken at three locations across the MLC for the combined field dosimetry. The profiles were averaged for each location type across the four leaves, and the average mid-leaf profile was subtracted from the others. Figure 30 below portrays these difference profiles for the beams matched to -0.3 mm field gap at d_{max}:

A

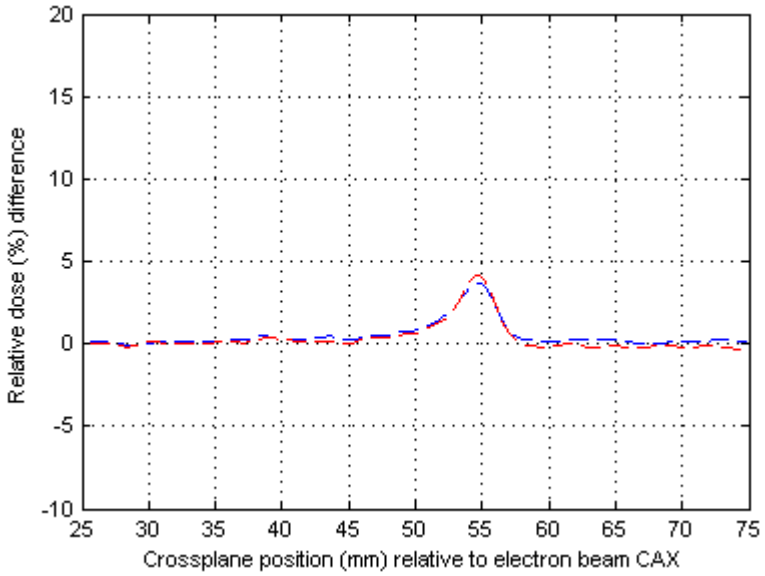
Relative dose (%) difference
20
15
10
5
0
-5
-10
25
30
35
40
45
50
55
60
65
70
75
Crossplane position (mm) relative to electron beam CAX

B

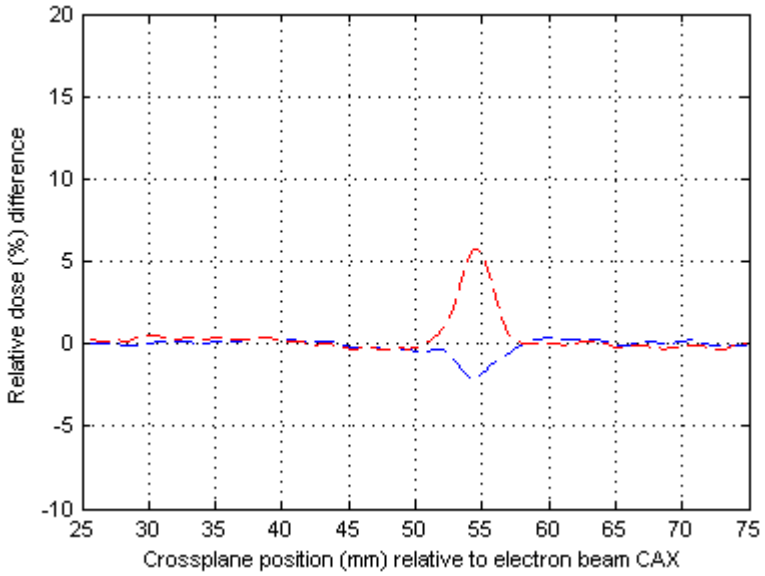
Relative dose (%) difference
20
15
10
5
0
-5
-10
25
30
35
40
45
50
55
60
65
70
75
Crossplane position (mm) relative to electron beam CAX

C

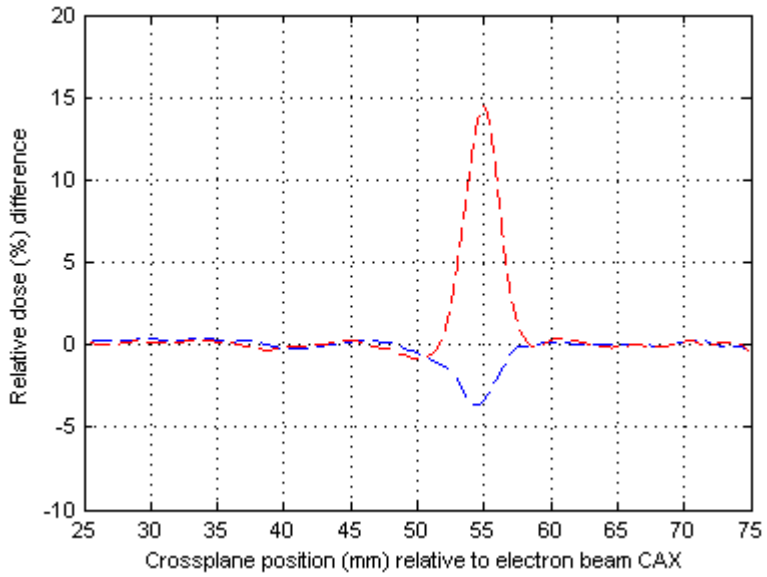

D

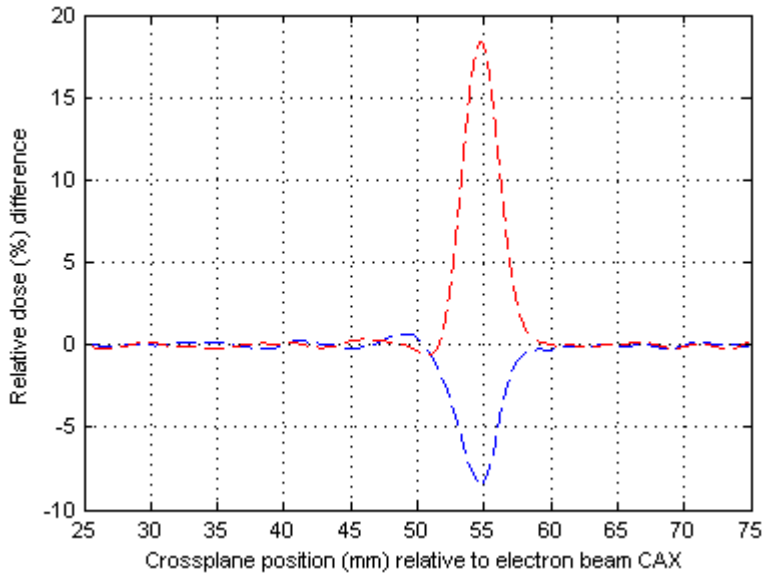

Figure 30: Relative dose profile differences due to MLC angle. Shown are difference plots of mean profiles sampled across the internal (red) and external (blue) MLC leaf points, and the average profile sampled across the MLC mid-leaf point. Graphs (A), (B), (C), & (D) present these results for MLC angles of 0°, 15°, 30°, & 45° respectively. For each, the beam abutment gap is a 0.3 mm field over-lap at d_{max} (15 mm).

The mean maximum deviation from mid-leaf dosimetry values, and standard deviations thereof, across all abutment gaps considered for each MLC angle, are shown in Figure 31 below:

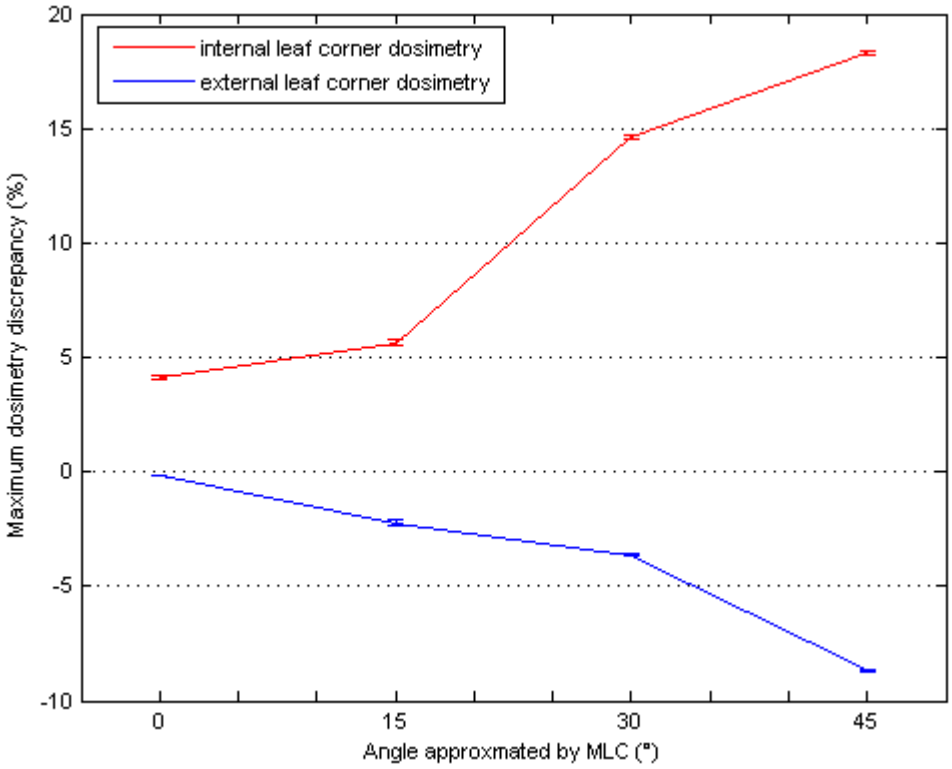

Figure 31: Intra-leaf dose-profile discrepancy variation with the angle approximated by MLC. Mean dosimetry discrepancy between internal leaf profiles (red) and external leaf profiles (blue) relative to the MLC mid-leaf profile is shown for MLC approximating angles of 0°, 15°, 30°, & 45° to the beam inplane axis. The standard deviation of these discrepancies across the abutment gap range -11 mm to +9.6 mm at d_{max} is shown in the error bars.

Here, we observe a trend in maximum positive and negative dosimetry deviation relative to the MLC mid-leaf point across the four MLC angles considered. Generally, larger angles approximated by the MLC correlate with larger intra-leaf dosimetry discrepancies – both positive and negative. The negative deviations are lower in magnitude than the positive deviations for all MLC angles. The profile discrepancy variations over all abutment gap situations are insignificant in contrast to the effect of MLC angle, as shown by the standard deviation error bars.

3.8 Hotspot magnitudes

As suggested in **Error! Reference source not found.**Figure 14, the magnitude of the maximum relative dose found within the composite scan volumes decreases as we move from large field overlaps to large field gaps. Figure 32 below presents hotspot magnitude data for each composite dosimetry permutation with each shielding angle/type. We observe a small spread across the data due to shielding angle/type. Here, we have around a 3% spread across shielding modes, and no mode is consistently placed within that spread.

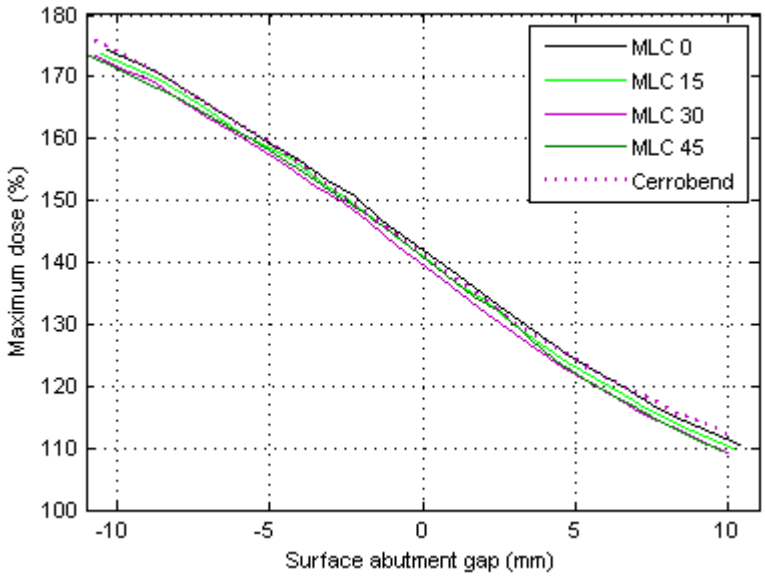

Figure 32: Hotspot magnitude at d_{max} as a function of shielding angle and abutment gap. Maximum dose sampled at 15 mm depth from all composite dosimetry volumes. The data are displayed for the surface abutment gap range ±11 mm. The lines connect the data.

3.9 Hotspot volumes

Analysis of composite scan volumes containing data exceeding a relative dose threshold of 110% was conducted for the range of abutment gaps, and for each photon beam shielding mode. Generally, the number of voxels exceeding the threshold was found to decrease as the dosimetry conditions progressed from large field overlap to large field underlap. Choice of shielding mode had some effect and we found that the use of Cerrobend® resulted in the largest hotspot for any given surface abutment gap.

For a surface field match – abutment gap of 0 mm – there is a 3% spread across the hotspot volumes resulting from each MLC angle. Generally, the higher angles provide smaller hotspot volumes. The 30° Cerrobend®-defined beam results in a hotspot volume over 6.6% larger on average than its 30° MLC counterpart for the gap range ±2.5 mm. Figure 33 below shows the hotspot volume across the range of surface abutment gaps for each shielding angle/mode. Linear approximations were fit to the data for each shielding angle and mode and are also presented below.

$$V_0 = -0.301a + 2.65 \quad (2)$$

$$V_{15} = -0.304a + 2.61 \quad (3)$$

$$V_{30} = -0.288a + 2.56 \quad (4)$$

$$V_{45} = -0.282a + 2.57 \quad (5)$$

$$V_{cerro30} = -0.277a + 2.73 \quad (6)$$

Hotspot volumes (V_θ) are expressed in cm^3 per unit of abutment edge length (cm) at d_{max}, and "a" represents surface abutment gap (in mm). The equations describe linear approximations for the hotspot volume data over the abutment gap range ±2.5 mm, and have R^2 values > 0.9944.

A

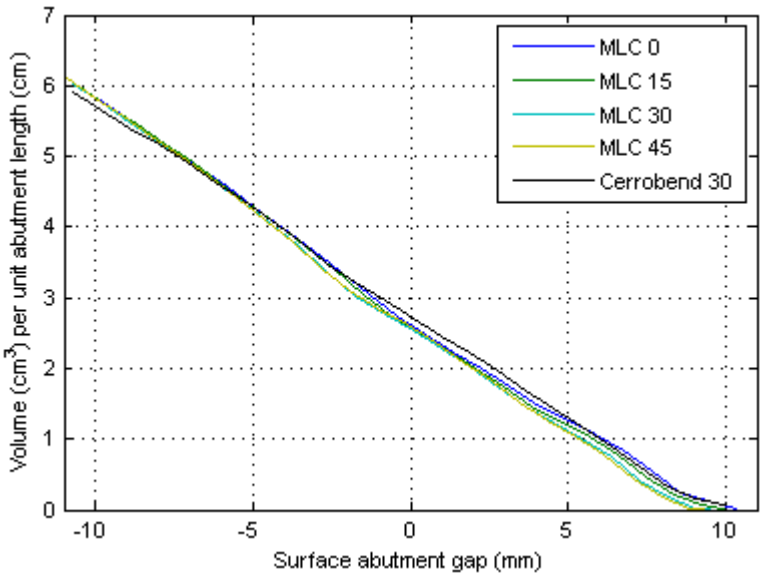

B

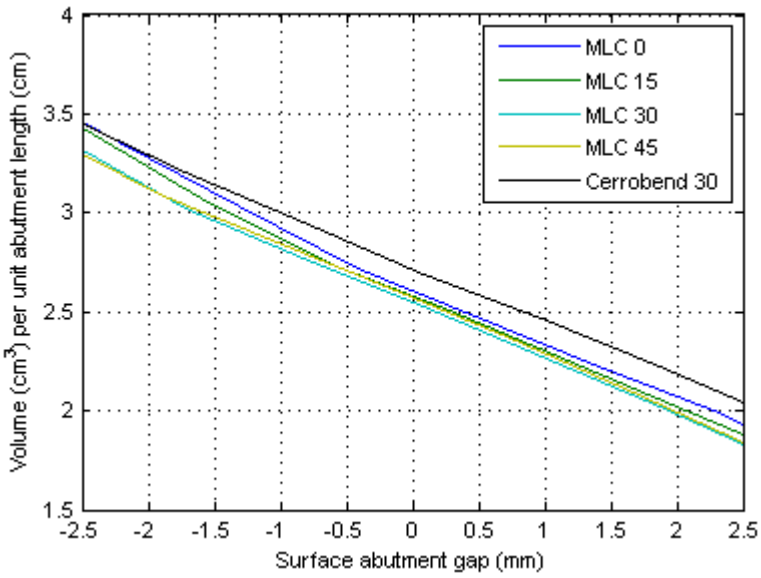

Figure 33: Hotspot volumes as a function of MLC angle and abutment gap size. Volume per abutment edge length, exceeding a 110% relative dose threshold, is plotted for each abutment gap and shielding mode/angle permutation (A). The plots are also shown in the more clinically relevant abutment gap range ±2.5 mm (B). The lines connect the data.

3.10 Minimum point dose at dmax

The combined dosimetry dataset was interrogated to determine the minimum relative dose at 15 mm depth. Figure 34 below presents the minimum relative point dose across

the abutment gap range ±11 mm for each MLC angle (solid colour lines) and the Cerrobend (dashed line) shielding. As we may expect, the minimum dose decreases as we progress from large field overlap to large field underlap for all shielding modes and angles. However, there is observed differences between the coldspot/abutment-gap relationship for the different shielding modes and angles. We observe a spread across the MLC data, with a general trend that the coldspot obtained at any given abutment gap is less pronounced for lower MLC angles. The 30° and 45° MLC data correspond reasonably well, while the 0° MLC generally results in 4% higher minimum dosimetry – the 15° MLC data lying in-between.

We see that for any given surface abutment gap, the minimum dose found in combined dosimetry involving Cerrobend® is significantly colder than dosimetry involving MLC. Conversely, if a minimum dose threshold is to be maintained, the field abutment gap involving Cerrobend® shielding must be around 1 mm to 2 mm less (more overlap) than that involving MLC (see Figure 34). A closer comparison of the shielding types reveals that MLC provides significantly “warmer” coldspot dosimetry than Cerrobend® for shielding making 30° to the beam inplane axis. Figure 35 shows the relative coldspot differences across the abutment gap range. We observe that minimum point dosimetry is between 1% and 7% warmer across the abutment gap range for 30° MLC, and being approximately 5.5% warmer for a field match (0 mm gap).

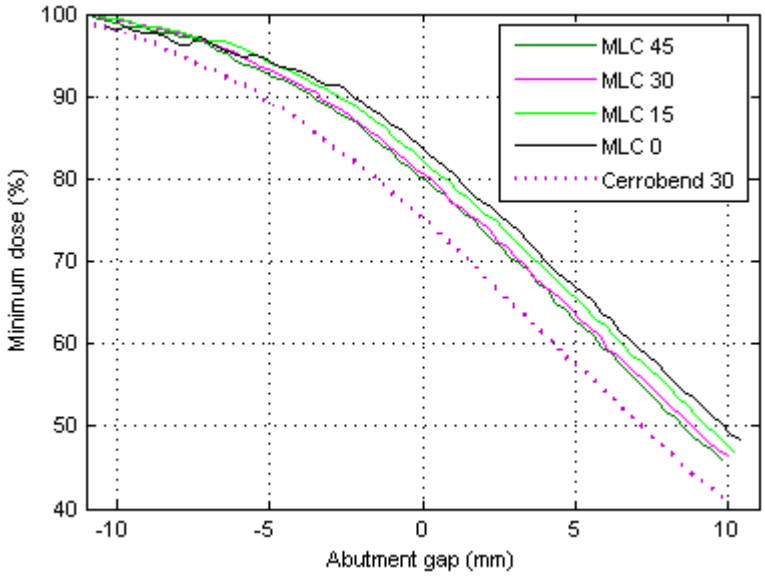

Figure 34: Coldest point doses at d_{max} due to MLC angle and abutment gap. Minimum values obtained from the combined relative dose arrays at 15 mm depth are shown for the range of surface abutment gaps and shielding mode/angles. Here we display data for the surface abutment gap range ±11 mm. The lines connect the data.

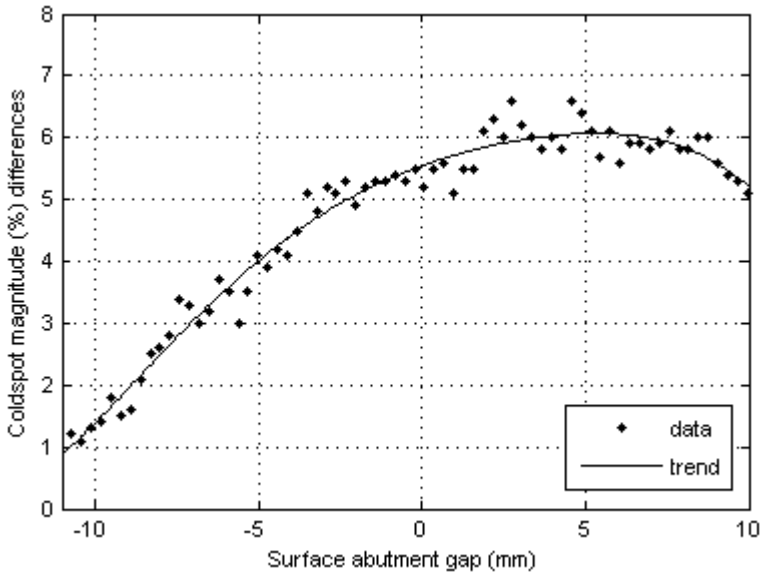

Figure 35: Coldspot differences – MLC vs. Cerrobend. Minimum relative dose sampled from combined dosimetry under Cerrobend is subtracted from that obtained under MLC. The data (with trend line) are shown for the abutment gap range: -11 to +10 mm. The shielding modes both approximate an angle of 30° to the beam inplane axis.

3.11 PDD-normalised dosimetry

A percentage depth-dose normalised dosimetry study was conducted on the combined dosimetry dataset in the MATLAB® workspace. We sought to investigate the amount of dosimetry data in the abutment region falling outside a certain range of expected relative dose given PDD data. Of special interest is the dose-volume region situated on the electron beam side of the geometrical photon beam edge.

Figure 36 below presents the results for this analysis of a beam abutment involving 30° MLC over the gap range -11 mm to +10 mm. The coloured lines represent the percentage of pixels at the selected depths within the VOI, falling above 110% of the expected PDD value for those respective depths. At all depths bar 30 mm, we observe the trend that larger abutment gaps produce dosimetry that decreasingly falls outside the 110% PDD threshold. Notably, at 30 mm deep the 110% PDD threshold is exceeded invariably across the abutment gap range. Additionally, we observe that PDD-normalised dosimetry improves i.e exceeds the 110% PDD threshold less, across the gap range, as we tend in depth towards d_{max} (15 mm).

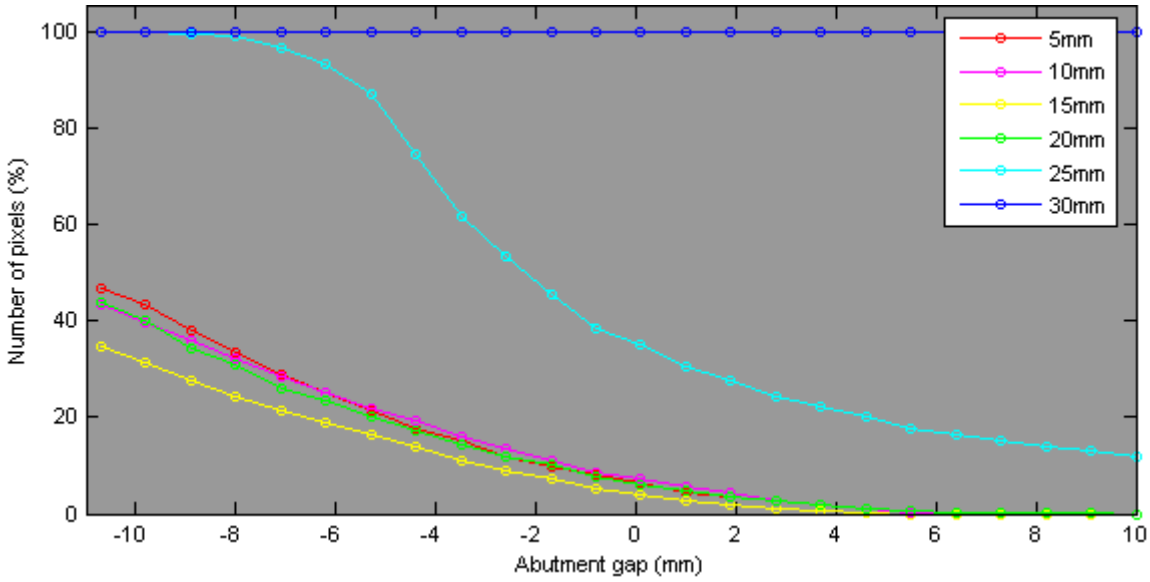

Figure 36: Relative dose exceeding 110% of PDD value. Displayed is the relationship between abutment gap and the amount of dose elements in the electron beam VOI that exceed 110% of the relative dose given PDD data for depths 5 mm through 30 mm. The lines connect the data – shown over the abutment gap range -11 mm to +10 mm, involving the use of 30° MLC-defined 6MV photons and the 10×10 cm^2 collimated 6 MeV electron beam.

Applying a similar analysis for relative dose elements falling below 90% of PDD yields results as presented in Figure 37 below. Here, as we may expect from data presented in the previous figure, the dose elements at 30 mm depth never fail to meet the 90% PDD value. At all other depths we observe the general trend that field gaps larger than -3 mm, produce increasing proportions of dose elements that fail to meet the 90% PDD threshold. Larger field overlap (>3 mm overlap) produces dosimetry above 90% of expected PDD at all depths. As before, we observe a trend as a function of depth: that for any given abutment overlap greater than 3 mm, the PDD-normalised dosimetry worsens as we tend towards d_{max} (15 mm) – that is, that a higher proportion of dose elements fail to meet the PDD threshold.

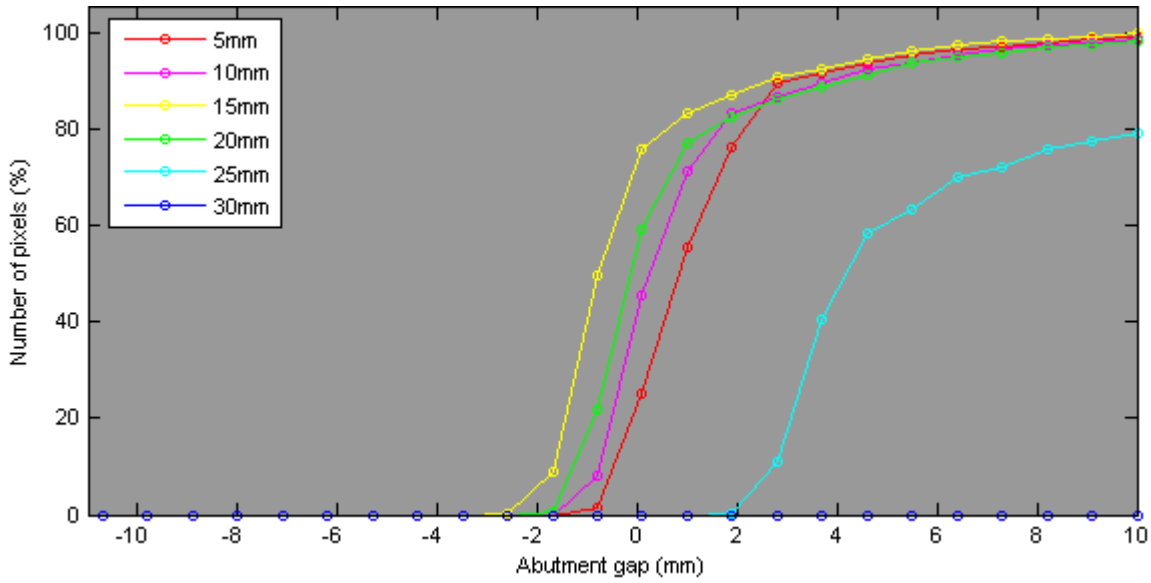

Figure 37: Relative dose less than 90% of PDD value. Displayed is the relationship between abutment gap and the amount of dose elements in the electron beam VOI that fails to exceed 90% of the relative dose given PDD data for depths 5 mm through 30 mm. The lines connect the data – shown over the abutment gap range -11 mm to +10 mm, involving the use of 30° MLC-defined 6MV photons and the 10×10 cm^2 collimated 6MeV electron beam.

In addition to the previous analyses, we can take the average of the dose element percentages through depth. Figure 38 below displays this result for dose volume elements exceeding the 6 MeV PDD data by a factor of 1.1 (red), failing to meet 0.9 of PDD data (blue), and falling within the two limits (green) for combined dosimetry employing 30° MLC. As expected the red and blue curves follow the general shape of the data in Figure 36 and Figure 37 respectively. Interestingly, the data falling within the 0.9 – 1.1 range peaks around field gaps of -2 mm, approximately coinciding with the meeting of the axis by the data falling below 90% PDD. From there, larger gaps see on average more dose elements failing to register 90% of PDD and less falling over or within the limits. Surface abutment gap of -0.4 mm see equal amounts of dose elements outside the 0.9 – 1.1 of PDD range.

Results for PPD normalised dosimetry involving the other MLC/Cerrobend® angles are presented in table format in the subsequent section.

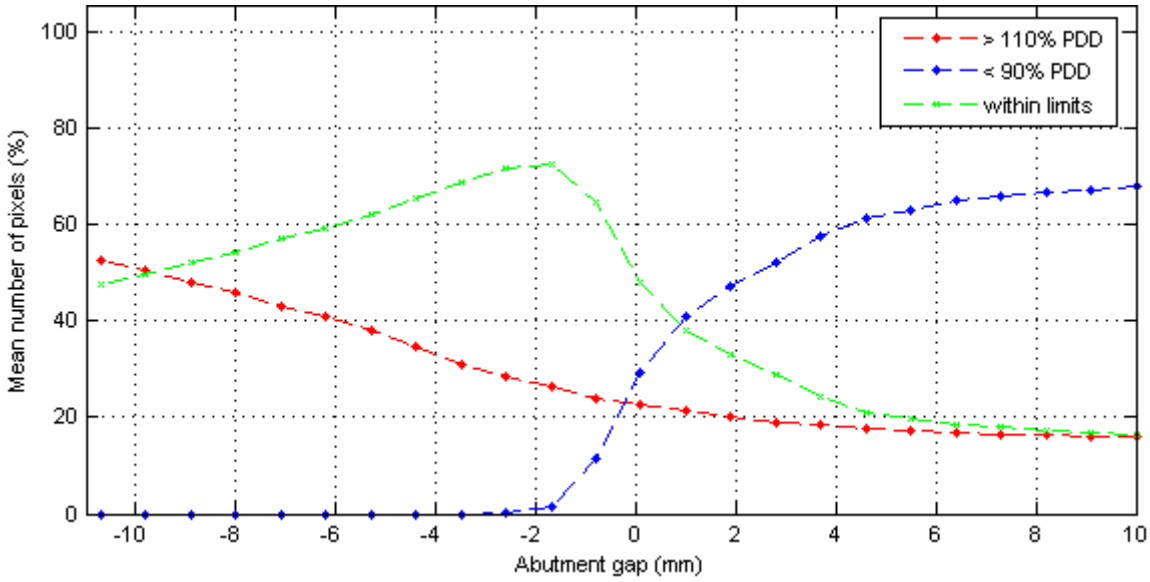

Figure 38: Mean PDD-normalised dosimetry for 30° MLC. The graph shows the average amount of dose elements over 110% PDD values (red), under 90% PDD values (blue), and within the ±10% of PDD range (green), for dosimetry within a VOI registered to the geometrical 30° MLC shielding edge and extending through depth from 5 mm to 30 mm under the 6MeV electron beam. The analysis was made across the surface abutment gap range: -11 mm to +10 mm.

3.12 Summary and clinical situation

Presented here are tabulated summaries of the results portrayed in the previous sections. The tables in this section offer clinically accessible results relating to the abutment of 6 MV photons defined by selected angles of MLC or Cerrobend® to 6 MeV electrons at extended SSD. Table 4 and Table 5 deal with aspects of dosimetry such as penumbral widths (prior to beam combination) and profile discrepancies resulting from use of MLC and/or extended SSD electrons. Table 8 to Table 10 deal with dosimetric considerations arising from the variation of abutment gap in addition to the employment of MLC when abutting with an extended SSD 6 MeV electron beam. For clinical relevance, we have presented this data at intervals of 0.5 mm over the tighter abutment gap range of ±2.5 mm.

Table 4: Penumbral widths. Shown are lateral displacements (mm) between the 80% and 20% isodose lines at selected depths under the 6 MV photon beam and the 6 MeV electron beam. The photon beam data is shown for beam shielding angled at 0°, 15°, 30°, and 45° to beam inplane axis defined by either MLC or Cerrobend®, and is stated for the mean orthogonal profile across this shielding. The electron data is presented for standard (100 cm) and extended (110 cm) SSD.

	6 MV photons (SSD = 98.5 cm)					6 MeV electrons	
Depth (mm)	MLC 0°	MLC 15°	MLC 30°	MLC 45°	Cerro 30°	SSD 100	SSD 110
5	3.6	3.9	3.9	4.1	2.7	-	-
10	3.5	3.6	3.7	3.8	2.5	9.0	19.3
15	3.6	3.8	3.8	4.0	2.6	11.2	18.8
20	3.8	3.9	4.0	4.1	2.7	19.9	30.0
25	4.0	4.1	4.3	4.4	2.8	-	-
30	4.4	4.4	4.6	4.7	3.2	-	-
35	4.6	4.7	4.9	5.1	3.5	-	-

Table 5: Profile discrepancies. Shown are relative dose deviations from mid-leaf dosimetry due to shielding angle. The values are averaged across, and standard deviations given, for the beam abutment gap range of: -11.1 to 9.6 mm at d_{max}. The data for Cerrobend® are theoretical and limited by construction accuracy.

Angle	max Δ%	δ	min Δ%	δ
MLC 0°	4.1	0.1	-0.1	0.0
MLC 15°	5.6	0.1	-2.3	0.1
MLC 30°	14.6	0.1	-3.6	0.0
MLC 45°	18.3	0.1	-8.7	0.1
Cerro 30°	0.0	-	0.0	-

Table 6: Hotspot Magnitudes. Shown are maximum relative dose (%) values found in the abutment region for the composite dosimetry involving the shielding angles or types shown for the abutment gap range ±2.5 mm.

	Surface abutment gap (mm)										
Angle	**-2.5**	**-2**	**-1.5**	**-1**	**-0.5**	**0**	**0.5**	**1**	**1.5**	**2**	**2.5**
MLC 0°	149.8	148.0	146.1	144.2	142.4	140.6	138.8	137.1	135.2	133.4	131.6
MLC 15°	148.0	146.2	144.3	142.6	140.7	138.9	137.2	135.4	133.6	131.7	129.9
MLC 30°	146.3	144.5	142.7	140.8	139.0	137.3	135.5	133.7	131.9	130.0	128.1
MLC 45°	145.4	143.5	141.8	139.9	138.1	136.4	134.6	132.8	130.9	129.0	127.2
Cerro 30°	146.0	144.2	142.4	140.5	138.8	137.1	135.3	133.4	131.6	129.6	127.8

Table 7: Hotspot volumes. Shown are volumes (cm^3) per abutted field edge length (cm) exceeding 110% relative dose in the combined dosimetry employing either MLC or Cerrobend® at the angles selected, for a surface abutment gap range of ±2.5 mm.

	Surface abutment gap (mm)										
Angle	**-2.5**	**-2**	**-1.5**	**-1**	**-0.5**	**0**	**0.5**	**1**	**1.5**	**2**	**2.5**
MLC 0°	3.46	3.29	3.10	2.92	2.75	2.61	2.47	2.34	2.20	2.07	1.94
MLC 15°	3.43	3.24	3.04	2.86	2.71	2.58	2.44	2.30	2.17	2.03	1.88
MLC 30°	3.32	3.12	2.96	2.82	2.69	2.55	2.41	2.27	2.13	1.99	1.84
MLC 45°	3.28	3.12	2.98	2.84	2.71	2.58	2.43	2.29	2.15	2.00	1.84
Cerro 30°	3.45	3.29	3.15	3.00	2.85	2.71	2.58	2.46	2.33	2.19	2.05

Table 8: Minimum point dose at d_{max}. Shown are lowest relative dose (%) data within a 6 MV photon – 6 MeV electron combined dosimetry involving the use of either MLC or Cerrobend® at the angles selected, for a surface abutment gap range of ±2.5 mm.

	Surface abutment gap (mm)										
Angle	**-2.5**	**-2**	**-1.5**	**-1**	**-0.5**	**0**	**0.5**	**1**	**1.5**	**2**	**2.5**
MLC 0°	90.7	89.4	88.0	86.6	85.3	83.7	82.1	80.6	78.6	77.0	75.7
MLC 15°	89.4	88.2	86.9	85.3	83.8	82.2	80.6	79.2	77.6	75.8	74.6
MLC 30°	87.9	86.5	85.2	83.6	82.0	80.6	79.2	77.0	75.7	74.4	72.4
MLC 45°	87.5	86.3	84.5	83.2	81.7	80.1	78.5	77.2	75.4	73.6	71.9
Cerro 30°	82.7	81.5	79.9	78.3	76.7	75.3	73.6	71.8	70.2	68.2	66.4

Table 9: Normalised dosimetry exceeding 110% PDD. Shown are percentages (%) of the volume elements within the combined dosimetry that exceed the percentage depth-dose values by the stated threshold. The data represents the situation in the abutment region mostly under the 6 MeV electron beam in a VOI defined laterally by the geometrical edge of the 6 MV photon beam through depths 5 to 35 mm. The analysis uses the PDD data from a 6 MeV electron beam.

	Surface abutment gap (mm)										
Angle	**-2.5**	**-2**	**-1.5**	**-1**	**-0.5**	**0**	**0.5**	**1**	**1.5**	**2**	**2.5**
MLC 0°	31.1	29.6	28.2	26.8	25.5	24.2	22.9	22.1	21.3	20.5	19.7
MLC 15°	30.6	29.2	27.7	26.6	25.5	24.4	23.4	22.4	21.6	20.7	20.1
MLC 30°	28.3	27.0	25.8	24.5	23.6	22.8	22.0	21.2	20.6	20.0	19.4
MLC 45°	27.5	26.5	25.5	24.6	24.0	23.3	22.6	22.0	21.4	20.8	20.3
Cerro 30°	17.7	17.3	17.0	16.5	16.2	16.0	15.9	15.7	15.6	15.5	15.4

Table 10: Normalised dosimetry below 90% PDD. Shown are percentages (%) of the volume elements within the combined dosimetry that fall short of the percentage depth-dose values by the stated threshold. The data represents the situation in the abutment region mostly under the 6 MeV electron beam in a VOI defined laterally by the geometrical edge of the 6 MV photon beam through depths 5 to 35 mm. The analysis uses the PDD data from a 6 MeV electron beam.

	Surface abutment gap (mm)										
Angle	**-2.5**	**-2**	**-1.5**	**-1**	**-0.5**	**0**	**0.5**	**1**	**1.5**	**2**	**2.5**
MLC 0°	0.0	0.0	0.0	1.6	4.2	13.7	25.0	33.7	41.5	45.3	48.3
MLC 15°	0.0	0.2	0.3	4.8	10.4	20.4	29.2	36.3	41.4	45.1	47.8
MLC 30°	0.2	0.9	3.6	9.3	17.5	27.3	34.5	41.0	44.3	47.6	50.3
MLC 45°	0.7	1.9	7.5	14.4	23.7	32.2	37.7	42.4	46.0	49.6	53.3
Cerro 30°	12.1	20.0	27.3	33.7	39.3	44.2	48.3	52.3	57.3	61.9	65.1

Currently, our clinical procedure is to match the optical field edge of the extended SSD 6 MeV electron beam to the optical field edge of the 6 MV Cerrobend® defined photon field at the treatment volume surface. From the data presented in the previous tables we can make the following statements:

1) At 15 mm depth we have electron penumbral width of 18.8 mm to match to the 2.6 mm penumbral width of the Cerrobend® defined photon beam.

2) There is theoretically no discrepancy between any two relative dose profiles sampled orthogonally across a field abutment involving Cerrobend® shielding for the photons.

3) The magnitude of the local maximum hotspot is 137.1% relative dose.

4) The size of the dose volume exceeding 110% relative dose is 2.71 cm^3 per unit length of abutted field edge.

5) A local minimum relative point dose of 75.3% will be observed at 15 mm depth in the abutment region.

6) On average, 16.0% of the dose volume in the abutment region outside the geometrical edge of the photon beam exceeds the 6 MeV PDD data by a factor of 1.1 (110%).

7) On average, 44.2% of the dose volume in the abutment region outside the geometrical edge of the photon beam fails to meet the 6 MeV PDD data by a factor of 0.9 (90%).

Chapter 4

Discussion

4.1 Measurements and data acquisition

4.1.1 Use of diode detectors

For combined dosimetry simulation we collected relative dose data using an unshielded p-type silicon diode (no. FP1949) used in two orientations for the two beam modes. Manufacturers documentation states the diode has a detector face diameter of 2.5 mm, and a thickness of 0.5 mm (see Appendix C.1). The use of the diode orientated orthogonally to the photon beam CAX (orientation 2) meant an increased resolution potential of the 5 mm Millennium MLC projected leaf widths, by presenting a thinner detector edge (0.5 mm) to the beam. However, the change of orientation put the P_{eff} into question, as the detector thickness in the CAX direction increased to 2.5 mm.

Construction asymmetries – the location of the detector and centring plate within the epoxy substrate – have been shown to potentially exist for Scanditronix p-type diodes [30]. Angular dependency of the diode detectors was not tested experimentally. However, locating one side of the cylindrical diode structure toward the beam source for all measurements in orientation (2) eliminated the angular dependency concerns. The diode used in this manner was compared, along with use in the upright orientation, to the photon diode (no. FP1942) in both its upright and orthogonal orientations, for relative dose response over 15 cm depth.

We observed that the unshielded diode, orientated orthogonally to the beam CAX, responded to within the standard error of the depth-dose response of the shielded photon diode used in its standard orientation, over the depth range 5 mm to 35 mm. When used in the upright position this diode compared even better, especially in the build-up region, but this use gave no advantages for MLC leaf resolution. The shielded photon diode

orientated orthogonally to beam CAX compared the closest to its upright depth response through larger depths but performed poorly in the build-up region. This is not unexpected, as this diode has tungsten mixed with the epoxy in the lateral region surrounding the active element [30] that, for upright use, attenuates laterally scattered radiation – correcting the diodes response through depth. Oriented orthogonally however, the tungsten serves to attenuate the primary beam, significantly increasing the effective depth of the active element.

From this comparison, the use of the unshielded diode (no. FP1949) used orthogonally to beam CAX is justified for the photon beam-edge profile scans within the depth range mentioned. Further departmental investigation should be conducted to assess the internal structure and/or angular dependency of the diodes if work outside the experimental limits mentioned here is required.

4.1.2 Composite dose volumes

Having found that the unshielded diode, used in an orientation orthogonal to the 6 MV photon beam CAX, responded comparatively to the upright shielded diode through depths 5 to 40 mm, relative dose scanning across the photon beam between these depths was justified. Collection of scan data in the IP-CP direction under each MLC or Cerrobend®-defined photon beam, and the electron beam was machine-time intensive. With the scan line spacing and scan speeds required for adequate resolution of the MLC shielding, the beam data collection was many hours of work aside from clinical interruptions, equipment setup time and failures, operating errors, and other delays. However, with this acquisition complete, composite relative dose volumes could be created via the manual summation of each photon scan at each depth with the corresponding scans of the electron beam edge. These summations were made straightforward through the use of MATLAB®. Furthermore, permutations made to the photon datasets prior to combining with the electron dataset, allowed for the simulation of a large range of beam abutment gaps. These composite relative dose volumes are characterised by good data resolution in the IP and CP directions (1 entry per 0.3 mm), and coarser yet adequate resolution through depth (1 entry per 5 mm).

4.1.3 Film comparison

An attempt was made to prove the validity of constructing composite relative dose volumes from data collected separately under different beam modalities using RG verification film. We built a sensitometric curve from exposures to film from both 6 MV photon and 6 MeV electron beams under standard field size and SSD conditions. Sensitometric response of RG film to the different beams was comparable but not exact. The mean OD response was taken for the data pair at each MU exposure level. An exponential equation was fit to this data and used for the subsequent processing of profiles obtained from film exposed to two abutment situations. The sensitometric equation had a correlation coefficient of greater than 0.9997. The profiles obtained from the two abutment situations resulted from variations in abutment gap only, and not depth or MLC shielding angle. We made no comparison between MLC and Cerrobend® shielding in this part of the investigation. A set dose of 40 MU was delivered with the 6 MV photon beam. The corresponding linac MU settings for 6 MeV electrons, given applicator size and SSD considerations, was determined experimentally to be 52 MU. These MU settings put the film exposure level to around the mid-point of our sensitometric data. In terms of data processing using the sensitometric equation, this allowed for the expected “double-up” of dose along the abutment edge due to field overlap, as per one of the abutment conditions.

The two film profiles obtained from the two abutment conditions were compared with two profiles extracted from the corresponding composite relative dose datasets. Here we observed a qualitative match in the shape of the profiles for each abutment gap scenario. However, significant quantitative differences were observed – up to a difference of 11% and 12% relative dose for the overlap and underlap conditions respectively; with the diode scan data consistently indicating higher dose than what the film showed. Initially, this suggests that the diode scan combination is invalid if film is to provide the standard. However, it must be noted that these differences are a function of the positional registration of the diode scan data with the film data. In this case we registered the local maxima of the profile pairs, leading to the qualitative but not necessarily quantitative matches. While the diode scan data positions are recorded in the

Wellhofer software, the film registration information was only recorded on the packet and may move relative to the film itself between exposing and fixing. It is recommended that future work solely targeting quantitative differences provide some means of recording the exact position on the film relative to the field edges in order to transfer to the film profiles. Here, gentle pin pricks through the film packet may suffice, though these may have to be located off the intended scan profile.

Other factors exist that should be considered before casting doubt upon the validity of the diode scan composition method. While film has an excellent spatial resolution, the OD scan equipment has an aperture of 12 mm, providing a spatial resolution of 3 mm with the receiving electronics set to the 10-90% range (see Appendix C.2). This resolution is not adequate to discern dosimetry on the intra-leaf scale, especially when scanning perpendicular to the shielding edge defined by stepped leaves. In addition to the spatial averaging, the data quality suffers from a “moving average” smoothing method across the data. Thus areas of high magnitude hot and cold spots on the film may be under-represented when transferred to electronic format.

Another clue is provided in Figure 13 (A) for the composite dose data. Here we observe the profile outside the photon field tracks significantly above 0% towards smaller CP positions, this is due to inter- and intraleaf transmission/leakage. Other research suggests average transmission/leakage through the MLC can be expected to be around 2% [31, 32]. Because the film profiles were normalised to a separate photon field, and the MU for the electron beams were experimentally adjusted for equivalency, we expect to see at least 100% relative dose within the electron field region, if not over 100% due to the dose contribution transmitted through the photon shielding. The diode scan profiles tend to 104% towards the electron field side (smaller CP position) of each abutment situation. However, the film profiles both tend to 100% relative dose in the direction of the middle of the electron field. Hence we have reason to doubt the ability of our film method to accurately represent the dosimetry situation.

The cause of this may reside in the underlying sensitometry methods employed. It was stated earlier that the sensitometry data for the photon and electron beams were comparable but not identical. The mean OD for each MU setting was used to generate an equation that was in turn used to convert the film abutment OD profiles back into MU, for final conversion to relative dose profiles. This equation was shown to represent the mean data extremely well over the range of MU's considered, but the fact remains that the sensitometry data for each beam modality differed – e.g. by around OD of 0.25 at 50 MU. In terms of converting the OD profiles, this difference of 0.25 leads to differences of around 10 MU, or ±5 MU from the mean. With reference to the raw sensitometry data, using the mean OD results in under-representing the MU from 6 MV photons for any given OD, and an MU over-representation for the 6 MeV electron data. After rescaling to relative dose, these MU differences may well comprise the differences observed when comparing with the direct diode scan profiles. Hence the attempt to utilise one sensitometric curve to convert film data from two beam types is potentially limited from the outset, and cannot necessarily be used to make quantitative comparisons. Avoiding this issue by constructing two sensitometric curves requires separate (non-abutted) exposures to film from each beam, and subsequent individual profile sampling before final summation to simulate abutment conditions. However that approach provides no advantage over the diode data compositional methods employed here. The use of other beam energies or film placement depths may provide for more comparative sensitometry. For exposures from 6 MV photons and 6 MeV electrons at 15 mm deep, as relevant to this study, the use of film is restricted to qualitative analysis; only in this manner is the validity of the diode scan compositional methods assured.

4.2 Dosimetric characteristics

Here we report on the findings and implications of both our investigation into the effects of the experimental conditions on the characteristics of the radiation beams; and on the various volumetric analyses performed on the composite dosimetry dataset.

4.2.1 Treatment beams

We conducted analyses into the effect on photon beam penumbra due to MLC stepping/angle; the effect on CAX PDD and off-axis dosimetry of the electron beam due to extended SSD, and also the ability of the TPS to accurately account for the extended SSD.

4.2.1.1 Photon field definition

Determination of the mean dosimetry through depth across each photon beam edge defined by either MLC or Cerrobend® was made. Isodose contour maps were generated, and the lateral separation between the 80% and 20% isodoses measured. We observed that this separation increased at all depths as the MLC stepping was increased from a shielding angle making 0° to the beam IP axis, to a saw-toothed shape making 45° to the beam IP axis. We also observed that the penumbral width under the MLC making 30° to the beam IP axis was significantly larger (~1.5 times) at all depths than the penumbral width under the photon beam defined by the equivalent Cerrobend® shielding. On top of differences in shielding transmission e.g. at the MLC leaf tip, this effect may in part be due to the different distances each shielding type is located from the radiation source. When used, the Cerrobend® blocking and mounting is inserted below the primary and secondary (MLC) collimation systems. It is therefore more proximal to the patient/phantom, and this in turn contributes to a tighter penumbra.

Taking the average beam edge mathematically is not dissimilar from the results reported by Galvin *et al* (1996) and Hwang *et al* (2002), who employed intra-fraction leaf shifts to blur the stepped field edge. Hwang *et al* observed a penumbral width increase due to a “feathered” MLC edge of around 1.9 times greater than that resulting from Cerrobend® for their equivalent (labelling conventions differ, here: 30°) shielding designs [13]. Galvin *et al* restricted their study to a sawtooth (here: 45°) MLC shape utilising MLC with leaf widths of 1 cm. At d_{max} the ratio of *effective* penumbra width of MLC to Cerrobend® was 2.2, resulting from an absolute effective separation of the 80%-20% isodose lines of 4.0 and 8.9 mm, for Cerrobend® and MLC respectively. Using a 4

segment regime they managed to reduce this ratio to 1.7, being a MLC isodose width of 6.8 mm [12].

In our study we observed a mean 80%-20% width of the 45° beam edge at 15 mm depth to be 4 mm. However, here the thinner (5 mm) leaves were used. This mathematically averaged field edge is what the physical feathering would achieve ideally. If we were to take the effective penumbral width value of 4 mm for 45° Cerrobend® as in the work done by Galvin *et al*, then it appears that the effective penumbral width converges to the mean penumbral width for 5 mm leaves under an ideal feathering regime. However, positional differences of the shielding within the fields for each study, and hence divergence of the beam edges, need to be considered. Given our data for 30° shielding, it is fair to say that the beam edge dosimetry under MLC would not match that under equivalent Cerrobend® shielding even with ideal feathering. As mentioned we see an increased 80%-20% lateral isodose separation of ~1.5 times that under Cerrobend® which supports the effects reported in the other research.

Beam edge feathering was not something in this study. However, making determination of the mean penumbral widths due to un-feathered MLC shielding angle is pertinent to understanding the optimisational challenge of abutting these beams with extended SSD electron beams. Left unmodified, the abutting electron beam edge is straight rather than stepped. Altering the MLC shielding angle, and hence the stepping, may somewhat improve the lateral positional match between the complementary isodoses of the beam modalities. On the other hand, increased MLC stepping leads to intra-leaf dosimetric discrepancies in the direction perpendicular to the shielding line. This we discuss in a later section relating to the compositional dosimetry.

In addition to the spreading of the average beam edge dosimetry relative to Cerrobend®, stepped MLC use also introduces relative hot and cold dosimetry along the beam shielding edge. To demonstrate this, we subtracted the photon dose-volume data obtained under Cerrobend® shielding from the data obtained under the equivalent MLC

shielding. Shielding equivalency, in this case, means that the geometrical field edge of the Cerrobend® block matches the geometrical positions of the mid-leaf MLC points along a projection from the beam source. The geometrical non-conformity of the MLC to the Cerrobend® shaping leads to dosimetric non-conformity. It was shown that the projection of the external MLC leaf tips into the primary field (over-blocking) resulted in cold spots relative to that observed under the Cerrobend®. Conversely, the geometrical gap between the 'ideal' edge and the internal MLC leaf tips (under-blocking) results in hot regions relative to the Cerrobend® dosimetry.

We observed an asymmetry between the hot and cold regions in terms of both the size and magnitudes of these dosimetry inhomogeneities. This asymmetry may be due to the physical limitations of the experimental setup. There are limitations on the accuracy of the construction of the Cerrobend® block, inaccuracies involved with the positioning of the block on the mounting plate, and also an inherent "play" of the mounting tray within the insertion system on the linac treatment head. A conservative estimate of the total uncertainty here would be around ±0.5 mm in the lateral directions. On the other hand, the MLC system incorporates infra-red laser leaf positioning system leading to an overall clinical tolerance of ±0.2 mm. While our scan volume was set identically for each beam measurement, a slight mismatch in shielding co-registration within the volume, due to the abovementioned reasons, may have led to the dosimetric inhomogeneity asymmetry observed here. However, the observations may instead be due to the characteristics of the MLC system on the intra-leaf scale. This we discuss further in section 4.2.2.2.

Without the required Cerrobend® data we could not make comparisons for the other shielding angles. Work by Zhu *et al* (1998) showed that dosimetric non-conformity (1 cm width MLC vs. Cerrobend®) of both 90% and 50% isodoses in the BEV plane, increased with smaller approximated circular field size [7]. In terms of leaf stepping, the variation of circular field size is similar to the variation of shielding angle used in our study, with smaller circles and higher angles corresponding to increased stepping, and increased geometrical non-conformity. Based on their work, and our findings for the 30°

shielding angle, it is reasonable to assume that the size of hot and cold regions are proportional to the shielding angle, as defined in this study. We surmise that the magnitude of the dose heterogeneities within these regions is also proportional to the geometrical shielding non-conformity, as all isodoses shift laterally with the leaf edge at a local scale. Specifically, as the size of the lateral displacement of the internal/external leaf tips from the ideal shielding edge approach the lateral width of the beam penumbra, then there should be increasing relative dose variation along the idealised shielding line at any depth. This would manifest as increased inhomogeneity, seen by taking a subtraction of the MLC and Cerrobend® data, as conducted in this study. However, as pointed out by Zhu *et al*, dosimetric non-conformity is reasonably, but not perfectly, predicted by geometric non-conformity, as other factors including scatter work to smooth out the penumbral dosimetry [7].

The other dosimetric issue observed in the subtraction investigation was the presence of a hot region in the Cerrobend® dataset due to holes in the block mounting tray. A typical mounting tray has 81 holes of 6 mm radius. Centre to centre, they are equally spaced over 20 cm in the IP and CP directions, therefore comprising over 18% of this interior portion of the tray. Compared to the open field dosimetry provided by MLC shielding, these holes allow an increased transmission of around 5% to 6% relative dose. Or conversely, the tray attenuates the beam by 5-6% over 82% of the beam area. In delivering a fixed MU to a patient/phantom, a tray factor has to be incorporated into the dose calculation that accounts for an overall attenuation by the tray. Nonetheless, while Cerrobend® provides a smooth and continuous beam edge shape, the resulting dosimetry suffers from inhomogeneities from these other causes that MLC use negates.

4.2.1.2 Extended SSD electron beam

The effects of increasing the SSD from 100 to 110 cm were mixed. We observed a decrease in surface relative dose of 2%, but mostly the percentage depth responses agreed within ±1%. These results agree in principle with the work of Das *et al* (1995), who reported a surface relative dose decrease of 5% for 110 cm SSD for the same field size and beam energy conditions [14]. Here we have further evidence that the increased

preferential removal of lower energy electrons from the beam outweighs the increased production of low energy electron within the air column; for small to moderate increases in SSD.

The effects on the off-axis dosimetry were considerable: a significant increase in penumbral width (80-20% isodoses) was observed, due to a lateral retraction of the higher isodoses, and a lateral spreading of the lower isodose lines. This resulted in a loss in beam flatness via an overall average penumbral width increase of 9.3 mm through depths 10 to 20 mm. These results support the findings of Saw *et al* (1995) and Das *et al* (1995).

Notably, we found that our TPS failed to accurately model the dosimetry resulting within a homogenous phantom exposed to the extended SSD electron beam. In order to make direct quantitative comparison between the measured and modelled data we fit Gaussian curves to the beam profiles. We found an extremely good fit to each dataset ($R^2 \geq 0.9998$), therefore this form of data representation was valid. The subtraction of the Gaussian representations at the corresponding depths gave close approximations to the dosimetry discrepancies between the measured and modelled data over the half-beam CP positions. The CP positions between 45 to 50 mm had the largest discrepancies – over 6% at 15 mm deep, and over 3% at 25 mm deep. The TPS overestimated the dose in the distal penumbra region, seen by the difference of -3.5% at 69 mm CP position, at 25 mm depth. The above gives grounds against the unconditional acceptance of the output of the TPS system for extended SSD electron dosimetry calculations involving heterogeneous media, especially in sensitive dosimetric situations such as with electron-photon field abutment for head and neck treatments. While version 7.6c of the Pinnacle^3 TPS models MLC with sufficient accuracy, the limitations inherent in extended SSD electron beam modelling render the current system inadequate for dosimetry modelling as relating to the clinical treatment conditions investigated here. These findings support the recommendations of the AAPM task group 25 report that call for radiation oncology department staff to assess the electron modelling abilities of their TPS on an individual basis [3]. A case is provided for the implementation of Monte Carlo techniques in the

absence of improvements to conventional TPS with regard to electron beam dosimetry modelling.

The increase of the SSD of the 6 MeV electron beam is necessary to avoid conflicts between the applicator and the patients shoulder. However the resulting modification to the beam penumbra significantly adds to the challenge of optimising the abutment of these beams to MLC-defined photon beams. While the use of tertiary collimators for extended SSD spinal irradiation treatments improves the penumbral properties of the electron beam [18], the use of such devices is defeated by the practical limits involved with head and neck treatments as outlined above. Therefore we did not consider the use of tertiary collimation in this study.

4.2.2 Composite abutment dosimetry

We conducted a number of analyses on the composite dosimetry data, including effects of abutment gap and MLC stepping on dosimetric intra-leaf discrepancies across the abutment region at d_{max}, hot and coldspot magnitudes within the abutment region, and size of volume over 110% relative dose. Furthermore, we report on the method and findings relating to PDD-normalised dosimetry.

4.2.2.1 Composite dosimetry methodology

Using the Wellhofer watertank dosimetry equipment to scan across the beams at various depths allowed for the reconstruction of coarse dosimetry volumes. This allowed for the measurement of hot and coldspot volumes as additional to just the magnitudes thereof, as per the referenced previous research. While film stacked in a phantom could be scanned to collect composite dose data, issues may arise with the sensitometry (as outlined previously), and the co-registration of the scans post-conversion to electronic format. TPS can be used to ascertain volumetric data, however these are potentially limited when modelling aspects of the beams involved – such as the electron beam penumbra in our case. Gel could be used to obtained 3D dosimetry incorporating patient geometry, however extensive resources and special equipment are needed for the preparation and measurement thereof. In this regard, currently only Monte Carlo

methods conducted on real patient 3D data can provide more accurate volumetric analysis taking into account all aspects of the beams and patient geometry; and additionally, patient tissue heterogeneities. In the absence of such modelling capabilities, we suggest that our scanning and composition techniques provided adequate insight into the underlying dosimetry resulting from the treatment conditions involved in this study.

4.2.2.2 Composite profile discrepancies

We conducted measurements on our composite dosimetry dataset to ascertain the effects of MLC stepping and abutment gap on relative dosimetry inhomogeneities near the MLC-defined field edge. Relative dose profiles extracted across the leaf tip corners were compared with profiles extracted from across the mid-leaf point. These points were selected based on geometrical determinations of the intra-leaf positions. We repeated this sampling for four arbitrary leaves, and determined the inter-leaf averages. The average profile across the mid-leaf point was subtracted from those across both the internal and external leaf-tip points, for each MLC shielding angle across the abutment gap range.

Greater MLC stepping means greater displacement of the internal and external leaf-tip points in the direction perpendicular to the shielding edge. As discussed in section 4.2.1.1, we expect larger dose inhomogeneity for larger MLC shielding angles across this edge. We deemed it pertinent to include the electron edge contribution prior to this sampling and comparison, as the dose contribution from the electron beam is differential in this sampling direction. Hence this analysis was performed on the composite dataset and not the un-combined photon beam data alone. We found that the MLC angle influenced the intra-leaf profile discrepancies strongly, although these differences were not moderated significantly by the abutment gap. Here, the rounded nature of the electron beam CP profile at d_{max} may reduce the effect of the abutment gap on these intra-leaf profiles. More highly differential CP profiles, such as those from electron beams at smaller SSD's or employing tertiary collimation, may indeed lead to significant moderation of the intra-leaf composite profile discrepancies with abutment gap. Therefore restricting such an analysis for an abutment dosimetry investigation as

described here to MLC-defined photon data alone, should not be performed without due consideration to the characteristics of electron penumbra involved.

At this point we highlight a further dosimetric trade-off when using stepped MLC photon field definition. That is, while the mean penumbral beam edge increases to more closely complement the electron beam penumbra with increased stepping, the magnitude of the resulting relative dose intra-leaf inhomogeneities also increases. For a saw-toothed shape these inhomogeneities may be up to 18% relative dose hotter, and 9% relative dose colder, than that found across the MLC mid-leaf point – where the beam edge, and therefore abutment gap, is geometrically defined for this study.

Also of note is the intra-leaf profile discrepancy for 0° (unstepped) MLC shielding (see Figure 30 A). As previously mentioned we observe a increased dose of around 4% hotter across each leaf-tip corner. This is presumed to be due to intra- and interleaf transmission. However, we do not see this raised dose level across the CP direction under the shielding as one may expect due to the profile tracking along under the interleaf tongue-and-groove seam. The subtraction of the mid-leaf profile accounts for the direct intra-leaf transmission. We observe that under the shielding, away from the leaf-tip, the difference returns to zero. Therefore, away from the shielding edge, the effects of leakage/transmission are the same under mid-leaf as on the inter-leaf margin. Yet we clearly observe a 4% hotter relative dose area at the leaf-tip corners. The MLC leaf tips are rounded in the CAX direction to maintain radiation and optical agreement over the range of possible field sizes, however the leaf tips are also slightly rounded in the plane orthogonal to beam CAX. It is this rounding towards each interleaf junction that may be causing the localised hotpots we observe here. This may to some extent also explain the asymmetry observed in the plot of maximum hot and cold discrepancies as a function of MLC shielding angle (see Figure 31), and the asymmetry between hot and cold dosimetry relative to Cerrobend® shielding as described previously in section 4.2.1.1. The geometry under a rounded leaf corners scenario suggests, that for stepped leaves, the shielding gap at the internal leaf points extend further away than the shielding at the external leaf points, relative to the MLC shielding edge definition (through mid-

leaf points). Therefore, we observed larger magnitude relative hot dosimetry than cold dosimetry across all MLC stepping regimes, including the unstepped scenario; independent of intra- and interleaf transmission/leakage.

In addition, with regards to the film comparison discussed earlier, the scale of this leaf rounding is well below the practical spatial resolution of the densitometry system, and hence the hot and cold spots are likely to be under-represented via the film dosimetry method – where both spatial and moving averaging effects smooth the data more than the diode system approach.

4.2.2.3 Hotspot magnitudes

Sampling maximum relative dose resultant at d_{max} confirmed that hotspot magnitudes are inversely proportional to abutment gap size. Shielding angle moderated the results slightly, with around a 3% difference in relative dose spread across the data at any given abutment gap. However, the relationship of the shielding angle data within this spread was not consistent. There appeared to be a small difference between Cerrobend® and MLC data of around 2% on average (standard deviation of 0.5%). So while MLC use introduces hot and cold regions relative to the Cerrobend® dosimetry (as discussed in section 4.2.1.1), this does not lead to an overall increase in the magnitude of maximum dose found in the composite dosimetry, in fact, to a small extent we see the reverse. This could be due to the overall tighter penumbra of the Cerrobend® beam edge, meaning higher isodoses are laterally closer to the geometric field edge (50% isodose), compared to the MLC situation, resulting in higher dosimetry when abutted with the electron beam. Notably, the maximum dosimetry only tends to below 110% relative dose for large abutment gaps at the extreme of our dataset (10 to 11 mm surface gap).

4.2.2.4 Hotspot volumes

At ARBCS we generally attempt to avoid delivering over 107% relative dose to any volume, though this target may have to be exceeded depending on the specifics of any given patient plan. We investigated how the volume of a relative hotspot – here defined as dosimetry exceeding 110% – varied as a function of abutment gap and shielding angle

and/or type. The value of 110% was chosen to provide a buffer to the ideal limit of 107%.

We found hotspot size to be inversely proportional to abutment gap size, and the relationship slightly moderated by shielding angle and type. The hotspots appeared for surface abutment gaps of 8 to 10 mm, and not surprisingly were vertically centred around 15 mm depth – being the d_{max} for both beam modalities. The Cerrobend® shielding condition appeared to provide significantly larger hotspot volumes for any given abutment gap size than the corresponding MLC condition (30°). Once again, this is probably due to the relatively smaller penumbral width and higher relative dose located nearer the Cerrobend® beam edge (see Figure 19).

We provided linear approximations to the hotspot volume data for each shielding condition. These were structured to provide the hotspot volume as a function of the length of the abutted field edge at d_{max} for any given surface abutment gap between ±2.5 mm. These equations should be of clinical use given that no computer treatment planning involving electron beams is currently implemented at ARBCS radiation therapy department. The coarse nature of the data through the depth dimension should be taken into consideration therein.

Overall, abutment gap size influences both hotspot size and magnitude markedly, with employment of MLC resulting in somewhat smaller volumes and magnitudes than that resulting under Cerrobend® over the entire gap range studied here.

4.2.2.5 Coldspot magnitudes

To assess the behaviour of cold composite dosimetry magnitudes, we performed very similar analysis as for the hotspot dosimetry described in section 4.2.2.3 above, except that we limited this to data sampling to 15 mm depth. This is because dose naturally drops off with depth, and we required an analysis of cold dosimetry in the abutment region as a function of abutment gap and/or shielding conditions. Similar to hot dosimetry, the cold dosimetry behaves inversely proportionately to abutment gap size.

Therefore if the ‘magnitude’ of the coldspot is defined as being the deviation from 100% relative dose, then we see that this magnitude is proportional to surface abutment gap. Here, there is a larger response spread across the shielding conditions with larger MLC shielding angles resulting in colder dosimetry. Here we infer that the dose inhomogeneities due to MLC stepping, as described in sections 4.2.1.1 and 4.2.2.2 previously, are contributing to overall measured cold dosimetry quite significantly. The 30° Cerrobend® block notably provided significantly colder point dosimetry than the MLC counterpart – relative dose differences of between 4% and 6% over the abutment gap ranges -5 to +5 mm respectively, and 5.5% colder for a field match (0 mm gap). Overall it appears coldspot dosimetry is somewhat more sensitive to the shielding conditions than the hotspot dosimetry.

4.2.2.6 Percentage depth-dose normalised dosimetry

To investigate the size of cold dosimetry within the abutment region under the electron beam, we employed a technique whereby the composite dose data is normalised to the PDD data. This eliminates the natural influence of depth to the dosimetry, leaving the size of cold and/or hot regions as a function of abutment gap size and shielding conditions. The volumes we investigated received dose from two beam types, with two depth dose distribution characteristics. Only one set of PDD data can be applied to the composite dataset at a time, depending on which part of the volumetric dosimetry we are interested in. Given that the position of the photon beam shielding is determined by the underlying physiology e.g. spinal cord, and the electron beam is applied so as to boost the remaining dosimetry; we determined the VOI in the boost region as relative to the geometrical photon beam edge. We then used the 6 MeV electron beam PDD data to analysis this boost VOI, acknowledging some contribution from the photon beam. The idea here being that the combination of the photon penumbra with the electron penumbra may bring the composite dosimetry within certain limits of what would be expected under full electron beam application.

While we looked at both normalised over and underdose, it is the later which is of greatest importance, as the former is mostly dealt with through determining non-PDD-

normalised hotspot volumes (as described previously). A scripted logic statement run through the volume elements is unable to differentiate between colds voxels resulting naturally from depth and those resulting from the abutment conditions. Such a method can however, compare each voxel with the relevant PDD data. Therefore PDD-normalisation is an improved method to assess cold dosimetry in a volumetric fashion.

Assessing relative cold dosimetry in this boost area is of major clinical importance since the only intention behind the use of the electron beam is to boost the superficial dose while sparing the tissue at depth. Failure to adequately boost the dose to the required volume is unacceptable. We found that a field overlap of 2 mm reduces the average amount of voxels not achieving 90% of the PDD value through depth to near 1% for all MLC angles. This also coincides with the maximum number of voxels agreeing with the PDD data by ±10%. PDD-normalised dosimetry under Cerrobend® is a different story, with the above qualities applying to a field overlap of 4 mm. Therefore we require more field overlap when using Cerrobend® to avoid significant amounts of volume from not achieving near the expected dosimetry given full beam depth data. However, this has obvious implications regarding both the size and magnitude of the hotspot resulting from this setup.

4.2.2.7 Dosimetry trade-offs

Abutment gap is the most significant determinant of the underlying dosimetry – both magnitudes of hot- and coldspots, and volumes thereof. For the beam energies considered here, there is no obvious set of conditions that provide for an acceptably low level of dosimetry heterogeneity i.e at the d_{max} depth, no combination of abutment gap and shielding angle or type results in the relative dose remaining in the range of 90% – 110% across the abutment region. While MLC use is detrimental to the dosimetry in terms of introduction of inhomogeneities for all angle from 0° to 45°, it appears its use is favourable over Cerrobend® when the magnitudes and overall volumes of hot/cold spots in the composite dosimetry are considered.

Clinical decisions regarding choice of abutment gap conditions need to first prioritise the importance of the abovementioned effects, which may be case specific, and the work herein may be referred to outline the expected results of such decision; assuming reasonable tissue density homogeneity of the treatment site.

4.2.2.8 Current clinical situation

The current practice of matching the electron field to the Cerrobend®-defined photon field at the patient surface results in hotspots of significant magnitude and volume, some cold dosimetry at d_{max} well below 90% relative dose, and significant amounts of the composite dosimetry under the electron beam falling outside a reasonable range of the PDD data. Furthermore, changing the abutment gap at the surface to mitigate any one of these dosimetry issues results in the escalation of another.

Additionally, the practical accuracy of the field matching needs consideration. The current method involves drawing the edge of the photon field to the patient immobilisation shell with a marker pen. This introduces the potential for inexact matching of abutment gap, on top of the limits of the patient immobilisation equipment, couch positioning etc. We estimate the uncertainty in the field match could be around ±1 mm due to thickness of the marker line. The data presented in this investigation can be used to determine the dosimetric variation due to this abutment gap uncertainty; for instance a ±1 mm positional uncertainty leads to a hotspot magnitude uncertainty of around ±3.5% on the stated 137.1% relative dose for an exact match. On the other hand, any inter-fraction variation may work to smooth out these effects over the course of the patient treatment, effectively “feathering” the junction to some extent. While potentially beneficial to the dosimetry, as shown in the work of Galvin *et al* and Hwang *et al*, there is the problem that this is somewhat random and not a guaranteed or controlled effect.

The use of MLC alters various aspects of the difficult dosimetry situation presented here. Firstly, the accuracy of the positioning of the leaves is far improved over the combined inaccuracies inherent to Cerrobend® block positioning. This implies reduced inter-fraction positional variation as well, however, the issues of patient and couch

positioning remain. A surface match with the equivalent MLC shielding provides for comparable hotspot magnitude, but reduced overall hotspot (>110% relative dose) volume compared with Cerrobend®. We see a reduced coldspot magnitude, and a reduction in the amount of dosimetry failing to make 90% of the electron PDD data. However, we see increased inhomogeneity in the match region, and increased amounts of the volume exceeding 110% of the PDD data. Given that the reason for the electron beam is to provide a superficial dose boost, it is suggested that MLC provides significant improvement over the use of Cerrobend® blocks. This suggestion is limited to the shielding angles, and field positions relative to the photon beam CAX, investigated here.

4.2.2.9 Further investigation

Further investigation could be conducted into the use of other electron beam energies, e.g. 9 MeV; other photon beam shielding angles i.e. MLC > 45°; and photon beam edge modifiers. While the experimental conditions involved are not all equal, other research using 9 MeV appeared to result in somewhat less inhomogeneous composite dosimetry [17, 22, 24, 25, 28]. A volumetric composite dosimetry comparison between the use of 6 and 9 MeV could be justified. Based on our results and the work of Li *et al* (1999), it is reasonable to suggest that the development of photon beam edge modification techniques be pursued within the radiation therapy department.

With regards to the later, simulation of “feathered” dosimetry – whether due to controlled techniques or a determined setup error variation, could be executed using the same photon scan data, as we can duplicate each relative dose scan, then divide each through by the number of duplications made. If each scan is then shifted relative to the others before recombining, this results in approximated intra-fraction “feathering”. This technique could be applied to both Cerrobend® and MLC defined photon data.

Chapter 5

Conclusion

This study set out to investigate the characteristics of the dosimetry resulting in a homogenous medium due to the abutment of *en face* high energy photon and electron beams as applicable to radiation therapy of the head and neck region. Specifically, we explored how replacing conventionally used Cerrobend® with 5 mm MLC to define the photon beam would affect the underlying dosimetry. Conjunctively, we assessed the effects of increasing the SSD of the 6 MeV electron beam for purposes of avoiding the patients shoulder, and this in turn was compared with the predictions of the current TPS electron beam model. We made novel use of the dosimetry equipment available, and these techniques were validated. We simulated composite abutment dosimetry in a volumetric fashion, and were able to control selected shielding type/angle and abutment gap variables. Selected simulation conditions were compared with measurements taken with film. Inhomogeneities due to the stepped edge MLC shielding, and beam combination were assessed. These inhomogeneities we compared to that seen under the continuous edged Cerrobend® and measured for relative dose magnitudes and volumes. We also implemented a measurement technique whereby the composite dosimetry in a VOI was compared to the PDD data for that VOI in order to assess cold dosimetry. All these results were presented and discussed. The 6 MeV electron beam delivered at the extended SSD of 110 cm provides a problematically large penumbra for which to match to an unmodified photon beam edge. We found that MLC provided for significant dosimetric advantages over the equivalent Cerrobend® photon shielding given a fixed surface abutment gap variable, though not without drawbacks. We found that for beam energies of the order employed here, no set of the abovementioned variables gave rise to composite dosimetry entirely between the acceptable limits of 90% and 110% at 15 mm depth. We outlined the compromises involved when adjusting these shielding and abutment gap variables in order to aid clinical decisions regarding this dosimetric challenge. The dataset is large, and can be used to provide dosimetric information regarding photon-electron abutment issues of this nature as customised to the requirements of departmental protocol.

Appendix A

Monitor unit determination

Using the international atomic energy agency (IAEA) radiation therapy dosimetry protocol technical reports series (TRS) No. 277 (1987) we calculated the dose to water (D_w) from 6 MV photons and 6 MeV electrons to the d_{max} depth. This protocol was followed via an national radiation laboratory (NRL) adaptation of the IAEA international code of practice. The ratio of these numbers was then used to determine equivalent MU settings to use for each radiation modality for the film dosimetry study.

A.1 6 MV photons

Monitor unit setting:		= 200 MU
Raw average reading:	$\mathbf{M^0_u}$	**= 1.870**
Range scale factor:	k_r	= 1.000
Dosimeter calibration factor:	N_D	= 0.977 Gy/div
Pressure:	P	= 101.07 kPa
Temperature:	T	= 21.4 °C
Correction factor:	p_{TP}	= 1.0071
Humidity correction:	k_h	= 1.000
Recombination correction:	p_s	= 1.006
Corrected average reading:	$\mathbf{M_u}$	$\mathbf{= M^0_u . k_r . p_{TP} . k_h . p_s}$
		= 0.9473 div/100 MU
Effective point of measurement:	Z_{eff}	= 1.5 cm – 0.26 cm = 1.26 cm
Correction factor:	$S^w_{air} . p_u . p_{cel}$	= 1.116
Absorbed dose to water:	$\mathbf{D_w(Z_{eff})}$	$\mathbf{= (M_u . N_D . S^w_{air} . p_u . p_{cel})}$
		= 1.0329 Gy/100 MU
	$\mathbf{D_w(Z_{max})}$	**= 1.0329 / 0.9891**
		= 1.0443 Gy/100 MU

A.2 6 MeV electrons

Monitor unit setting:		= 200 MU
Raw average reading:	$\mathbf{M^0_u}$	**= 1.540**

Range scale factor:	k_r	= 1.000
Dosimeter calibration factor:	N_D	= 0.977
Pressure:	P	= 101.07 kPa
Temperature:	T	= 21.4 °C
Correction factor:	p_{TP}	= 1.0071
Humidity correction:	k_h	= 1.000
Recombination correction:	p_s	= 1.019
Polarity correction:	k_p	= 0.9954
Electron fluence correction:	h_m	= 1.000 (for water phantom)
Corrected average reading:	$\mathbf{M_u}$	$\mathbf{= M^0_u . k_r . p_{TP} . k_h . p_s . k_p . h_m}$
		= 0.7866 div/100 MU
Range of 50% ionisation:	R^J_{50}	= 2.32 cm
Practical range of beam:	R^J_P	= 2.93 cm
Mean energy at surface:	$\bar{E}_0$	= 5.58 MeV
Effective point of measurement:	Z_{Peff}	= 1.5 cm
	Z_{Peff}/R^J_P	= 0.512
	$\bar{E}_Z / \bar{E}_0$	= 0.411
Mean energy at Z_{eff}:	$\bar{E}_Z$	= 2.293 MeV
Stopping power ratio water/air:	S^w_{air}	= 1.086
Perturbation factor:	$p_u . p_{cel}$	= 0.9599
Absorped dose to water:	$\mathbf{D_w(P_{eff})}$	$\mathbf{= M_u . N_D . S^w_{air} . p_u . p_{cel}}$
		= 0.8011 Gy/100 MU

A.3 Absorbed dose ratios

Taking the ratio of the above detemined dose-to-water values gives us:

R = 1.0443 / 0.8011 = 1.3036. Multiplying the 40 MU delivered by the 6 MV photon beam by this ratio gives us the equivalent MU setting for the same dose from the electron beam at 1.5 cm deep. This results is a setting of 52 MU, as the nearest whole number, for the 6 MeV electron beam.

Appendix B

Script code

In this section we present the custom script code written in MATLAB® and Visualization Toolkit (VTK) used for some data handling, analyses, and visualisation performed in this investigation.

B.1 MATLAB® Routines

B.1.1 Delimitation of scan data

```
% showit.m
%
% script that will open an (n x m) array from ASCII, remove all odd columns
% (in this case containing unwanted positional scan data), truncate appropriately
% to get an (m x m) matrix and display it.
%
% Jared Steel - 2006
%-------------------------------
r = input('please type variable name: ');
x = r;
a = size(x);
b = a(:,1);
c = a(:,2) -1;
x(:,1:2:c) = [];
clear r b c a d
imview(x,[]);
% end
```

B.1.2 Array rotation and alignment

```
% spin2.m
%
% This file takes a square array, pads and rotates it through a user defined angle,
% then crops the result appropriately to bring the array dimensions back to the original size.
% Update: Can now assign any and negative angles.
%
% Jared Steel - 2006
% ---------------------------------------------------------------------------------------------
R = input('please type array to rotate: ');
S = input('what angle to rotate through?   ');
%
flipper = flipud(R);
R = flipper;
radians = (2*pi*S)/(360);
F = size(R);
```

```
N = F(:,1);
%
syze = abs(sin(radians)*N + cos(radians)*N);
lines = abs((syze - N)/2);
LINES = ceil(lines)
%
padded = padarray(R, [LINES LINES],'replicate','both');
spun = imrotate(padded, -S, 'crop');
%
G = size(spun);
H = G(:,1);
trunc = ((H - N)/2);
Trunc = trunc - 1;
%
spun(:,1:trunc) = [];
spun(1:trunc,:) = [];
%
G = size(spun);
H = G(:,1);
%
trunc = N+1;
spun(:,trunc:H) = [];
spun(trunc:H,:) = [];
clear R S radians factor F lines LINES padded G H trunc Trunc N syze flipper
% end
```

B.1.3 Abutment gap calculation

```
% optidepth.m
%
% script to calulate surface abutment gaps based on geometry of abutment situation, including
% different divergence under different shielding angles, the SSD's for beam beam type, and the
% rotation of the photon fields to align with the electron field edge.
%
% Jared Steel - 2006
% -----------------------------------------------------------------------------------------------
userinput = input(...
'which angle MLC field to use for this analysis?(0 15 30 45, 3000 for cerrobend30
data)');
if userinput == 3000;
   shieldquery = 30;
else shieldquery = userinput;
end
Shieldquery = 2*pi*shieldquery/360; % Converts from degrees to radians
%
y    = [0:5:40];                % set depth range
boxy = [5:5:35];                  % diagram depth limits
boxx = [2.5:0.5:7.5];             % diagram crossplane limits
%
A = ((6.0-5.25)*sin(Shieldquery) - (6.0-5.25)*sin((45/360)*2*pi));  % (cm)
%
```

```
% A is an offset applied to bring non-45 degree MLC fields in line with the
% 45-MLC data. 5.25mm is the inplane mid-leaf position of leaf 41B. 6.0mm
% is the inplane position to the xray field centre (of rotation). The angle
% that the MLC has to be rotated to be brought in line with the Electron
% field edge determines how much the post-rotated field has to be offset.
%
%
Rtheta  = 5.25*sin(Shieldquery);    % Gives orthogonal displacement of MLC edge to x-ray
                                    %CAX in crossplane direction
RthetaE = 6.0*sin(Shieldquery);     % Gives orthogonal displacement of x-ray CAX to centre
                                    % of scanned Electon field
CAXsep  = 5.0 - RthetaE;            % Gives displacement of x-ray CAX to Electron CAX in the
                                    %direction of the
                                    % Electron field Crossplane
%
Rd  = (((y/10)+98.5)/100)*Rtheta;       % Gives radial position of optics through depth y
                                        %relative to x-ray CAX
RdE = Rd + CAXsep +A;               % Gives radial position of optics through depth y
                                    %relative to Electron CAX
%
shift = input('what range of shift to apply over?  ');
interval = input('what shift interval to sample at? ');
   %
   cplim1(1:7)  = [2.5];
   cplim2(1:7)  = [7.5];
   iplim1(1:11) = [5];
   iplim2(1:11) = [10];
   iplim3(1:11) = [15];
   iplim4(1:11) = [20];
   iplim5(1:11) = [25];
   iplim6(1:11) = [30];
   iplim7(1:11) = [35];
   %
for n = 0:interval:shift
   convertshift2x = (n*0.2994)/10;    % converts from columns to distance
   eop = ((110+(y/10))/100)*5;     % Gives position of Electron optics through depth y
   xop = RdE + convertshift2x;        % Gives position of x-ray optics relative to Electron CAX
                                      %for each y and for every abutment shift
   surfposE = 5.5;                    % the known surface position of the electron field edge
   surfposX = RdE(1)+convertshift2x;      % gives surface position of x-ray optical field
edge
   abutdist = ((surfposX - surfposE)*10);  % gives optical abutment gap
   %
   dmaxdist = ((RdE(4)+convertshift2x)-eop(4))*10;
   %
   plot(boxx,iplim1,'--k');
   hold on
   plot(boxx,iplim2,'--k');
   plot(boxx,iplim3,'--k');
   plot(boxx,iplim4,'--k');
   plot(boxx,iplim5,'--k');
   plot(boxx,iplim6,'--k');
```

```
    plot(boxx,iplim7,'--k');
    %
    plot(eop,y,'m','LineWidth',2);
    %hold on
    axis([0 8.0 0 40]);
    title(['Scan volume schematic: Optical field edge, ',int2str(shieldquery)...
        ,' degree MLC'],'FontSize',16);
    if abutdist < 0
        text(0.25,10,{['abutment gap =
'];[num2str(abutdist,'%+03.1f'),'mm'];['[field overlap]']},...
        'HorizontalAlignment','left',...
        'BackgroundColor',[.7 .9 .7],...
        'Margin',5,...
        'FontSize',14);
      text(0.25,20,{['gap at 15mm'];['depth =
',num2str(dmaxdist,'%+03.1f'),'mm']},...
        'HorizontalAlignment','left',...
        'BackgroundColor',[.7 .9 .7],...
        'Margin',5,...
        'FontSize',14);
    elseif abutdist > 0
        text(0.25,10,{['abutment gap =
'];[num2str(abutdist,'%+03.1f'),'mm'];['[field underlap]']},...
        'HorizontalAlignment','left',...
        'BackgroundColor',[.7 .9 .7],...
        'Margin',5,...
        'FontSize',14);
      text(0.25,20,{['gap at 15mm'];['depth =
',num2str(dmaxdist,'%+03.1f'),'mm']},...
        'HorizontalAlignment','left',...
        'BackgroundColor',[.7 .9 .7],...
        'Margin',5,...
        'FontSize',14);
    end
    set(gca,'YDir','reverse')
    plot(xop,y,'g','LineWidth',2);
    %
    xlabel('crossplane position (cm) relative to electron CAX','FontSize',16);
    ylabel('depth from water surface (mm)','FontSize',16);
    if userinput == 3000;
        filename =
['C:\matlab7\thesis\mergetest\images\optidepth\Cerro',int2str(shieldquery),...
        'opdepth',num2str(n,'%02.0f'),'.png']
    else filename =
['C:\matlab7\thesis\mergetest\images\optidepth\MLC',int2str(shieldquery),...
        'opdepth',num2str(n,'%02.0f'),'.png']
    end
    %filename = ['C:\matlab7\thesis\mergetest\images\optidepth\Cerro',int2str(shieldquery),...
    %    'opdepth',num2str(n,'%02.0f'),'.png']
    %print('-dpng', filename,'-zbuffer','-r55');
    hold off
end
%
```

```
clear shift interval y n convertshift2x *lim* *op filename box* surfpos* abutdist
dmaxdist *theta* A CAXsep *hieldquery
% end
```

B.1.4 Photon beam edge

```
% penwidth.m
%
% script that takes scan data (electron or photon), takes the mean slice (CP vs depth) and determines
% the lateral seperation of the 80% and 20% isodose contours at each relevant depth. Displays the %
% derived contour lines through depth, and the lateral seperation on a separate graph.
%
% Jared Steel - 2007
% ------------------------------------------------------------------------------------------------------
-
MLCquery = input('which angle MLC field to use for this analysis? (0 15 30 45 3000
6) ');
if MLCquery == 0
   load('c:\matlab7\thesis\6X00\MLC00z.mat');
elseif MLCquery == 15
   load('c:\matlab7\thesis\6X15\MLC15z.mat');
elseif MLCquery == 30
   load('c:\matlab7\thesis\6X30\MLC30z.mat');
elseif MLCquery == 45
   load('c:\matlab7\thesis\6X45\MLC45z.mat');
elseif MLCquery == 3000
   load('c:\matlab7\thesis\6Xcerro30\cerro30z-finalcorr.mat');
elseif MLCquery == 6
   load('c:\matlab7\thesis\6E\Electronarrays.mat');
elseif MLCquery ~= 0|15|30|45|3000
   error('There is no data for that MLC angle')
end
%
if MLCquery == 6;
   vol = cat(3,a05,a10,a15,a20,a25,a30,a35);
else
   vol = cat(3,A5,A10,A15,A20,A25,A30,A35);
end
%
clear A* a*
slice = rot90(squeeze(mean(vol)))/10;
%
[C,h] = contour(slice,[20 80]);
close
%
x20(1:C(2,1))= [C(1,2:C(2,1)+1)];
y20(1:C(2,1))= [C(2,2:C(2,1)+1)];
%
x80(1:C(2,C(2,1)+2))= [C(1,(((C(2,1)+3):(C(2,1)+2+(C(2,(C(2,1)+2)))))))];
y80(1:C(2,C(2,1)+2))= [C(2,(((C(2,1)+3):(C(2,1)+2+(C(2,(C(2,1)+2)))))))];
```

```
%
figure
plot(x20,y20,'g','LineWidth',2);
xlim([0 167]);
ylim([1 7]);
set(gca, 'YTickMode', 'manual','YTickLabel',[35 30 25 20 15 10 5]);
hold on
plot(x80,y80,'m','LineWidth',2);
xlabel('Scan position (0.3mm units)','FontSize',14);
ylabel('Depth (mm)','FontSize',14);
legend('20% isodose','80% isodose');
hold off
%
xi20 = interp1(y20,x20,[7 6 5 4 3 2 1]);
xi80 = interp1(y80,x80,[7 6 5 4 3 2 1]);
%
shieldlabeller = ['isodiff',int2str(MLCquery),' = (xi80 - xi20)*0.2994;'];
eval(shieldlabeller);
%
figure
xdeep = [5 10 15 20 25 30 35];
plotcall = ['plot(xdeep,isodiff',int2str(MLCquery),');'];
eval(plotcall);
xlabel('Depth (mm)','FontSize',14);
ylabel('Penumbra width (mm)','FontSize',14);
grid on
%
%
clear x* y* shieldlabeller C h vol MLCquery plotcall %slice
% end
```

B.1.5 Dose inhomogeniety due to MLC stepping relative to Cerrobend®

```
% diffvol.m
%
% This script performs a subtraction between the MLC and Cerrobend scan
% volumes. The subtraction dataset is interrogated for determination of the
% amount of voxels exceeding a user-defined dose-difference threshold. The
% user is given the option of viewing the raw scans, subtraction array, and
% a contour map of the subtraction array; for 15 mm depth data.
%
% Jared Steel - 2007
% -----------------------------------------------------------------------------
load('C:\matlab7\thesis\6XCerro30\cerro30z-finalcorr.mat');
Cvol = cat(3,A5,A10,A15,A20,A25,A30,A35);   % compile the scan data.
C15 = A15;
clear A*
%
load('C:\matlab7\thesis\6X30\MLC30z.mat');
Mvol = cat(3,A5,A10,A15,A20,A25,A30,A35);
M15 = A15;
clear A*
```

```
%
Diffvol = (Mvol - Cvol) / 10;
Diffscan = (M15 - C15) / 10;
%
S = size(Diffvol);  % determine size dimensions of dataset.
x = S(1);
y = S(2);
z = S(3);
%
I = input('Define upper or lower threshold? 0 = low, 1 = high            ');
T = input('Define threshold:                                             ');
%
% We now interogate the dataset with the threshold...
if I > 0
   if T < 0
      error('Must choose a positive threshold value!');
      break
   else
      thresh = 100*(sum(sum(sum(Diffvol > T ))) / (x*y*z));
fprintf('\nFor 30 degree shielding...');
fprintf...
   ('\nPercentage of MLC volume over %g hotter than Cerrobend = %g\n',...
   T,thresh);
   end
else
   if T > 0
      error('Must choose a negative threshold value!');
      break
   else
      thresh = 100*(sum(sum(sum(Diffvol < T ))) / (x*y*z));
fprintf('\nFor 30 degree shielding...');
fprintf...
   ('\nPercentage of MLC volume over %g colder than Cerrobend = %g\n',...
   T,thresh);
   end
end
%
clear Diffvol S x y z I T Mvol Cvol
%
Q = input...
  ('\nDo you want to view the Dmax difference arrays? 0 = no, 1 = yes  ');
if Q > 0    % Viewing stuff...
   figure
   subplot(1,3,1); imshow([0 167],[0 167],C15,[]);
   subplot(1,3,2); imshow([0 167],[0 167],M15,[]);
   subplot(1,3,3); imshow([0 167],[0 167],Diffscan,[]);
   figure
   [C,h] = contourf(Diffscan,[-30 -20 -10 -5 0 5 10 20 30]);
   set(gca,'DataAspectRatio',[1 1 1]);
else
end
clear Diffscan C15 M15 C Q h thresh
% end
```

B.1.6 Hotspot magnitudes

```
% maxdose.m
%
% This M-file creates a composite relative dose volume based on MLC photon
% data specified by the user. Total abutment shift range and sampling
% interval are also user defined. The script then samples the maximum
% relative dose found within each iteration over the abutment permutations.
% Abutment gap at 15 mm depth is geometrically converted to surface
% abutment gap. Plot of maximum dose as a function of surface abutment gap
% is diplayed.
%
% Jared Steel – 2006
% ------------------------------------------------------------------------------
MLCquery = input...
    ('which angle MLC field to use for this analysis? (0 15 30 45) ');
if MLCquery == 0
    load('c:\matlab7\thesis\6X00\MLC00z.mat');
elseif MLCquery == 15
    load('c:\matlab7\thesis\6X15\MLC15z.mat');
elseif MLCquery == 30
    load('c:\matlab7\thesis\6X30\MLC30z.mat');
elseif MLCquery == 45
    load('c:\matlab7\thesis\6X45\MLC45z.mat');
elseif MLCquery == 3000
    load('c:\matlab7\thesis\6Xcerro30\cerro30z-finalcorr.mat');
elseif MLCquery ~= 0|15|30|45|3000
    error('There is no data for that MLC angle')
end
%
% Concatenate the MLC x-ray arrays
VolX = cat(3,A5,A10,A15,A20,A25,A30);%,A35);
clear A*
%
% Now load the Electron array data....and concatenate...
load('c:\matlab7\thesis\6E\electronarrays.mat');
EVol = cat(3,a05,a10,a15,a20,a25,a30);%,a35);
clear a*
%
% Define total amount of shift, and interval within to sample at...
shift = input('what amount of shift to investigate over?    ');
interval = input('what interval to sample the shift range with?  ');
initial = input('what amount of shift to start script with?     ');
%
colsize = ((shift-initial)/interval)+1;
allocater = ['maxdoses',int2str(MLCquery),' = zeros(colsize,1);'];
eval(allocater);
clear allocater
    %
    for n = initial:interval:shift
        Varnamer = ['VolXshifted',num2str(n,'%02.0f'),' = VolX;'];
        eval(Varnamer);
```

```
        % Crop and Pad the X-ray volume according to a value
        % (0:interval:shift) - emulates a relative shift for adding to the
        % Electron volume...
        if n == 0
            Volcombiner0 = ['TDV',num2str(n,'%02.0f'),' = (VolXshifted',...
                num2str(n,'%02.0f'),' + EVol)/10;'];
            eval(Volcombiner0);
            layerget = ['dmax = mean(TDV',num2str(n,'%02.0f'),'(:,:,3));'];
            eval(layerget);
            clear Volcombiner0
        elseif n > 0
            Varcropper = ['VolXshifted',num2str(n,'%02.0f')...
                ,'(:,(168-',int2str(n),'):167,:) = [];'];
            eval(Varcropper);
            Varpadder = ['VolXshifted',num2str(n...
                ,'%02.0f'),' = padarray(VolXshifted',num2str(n...
                ,'%02.0f'),',[0 ',int2str(n),' 0],''replicate'',''pre'');'];
            eval(Varpadder);
            % Add the shifted X-ray volume to the Electron volume:
            Volcombiner = ['TDV',num2str(n,'%02.0f'),' = (VolXshifted',...
                num2str(n,'%02.0f'),' + EVol)/10;'];
            eval(Volcombiner);
            clear VolXshifted* Varnamer Varcropper Varpadder Volcombiner
        end
        %
        % Find the maximum point dose:
        maxfinder = ['maxdose = max(max(max(TDV',num2str(n...
            ,'%02.0f'),')));'];
        eval(maxfinder);
        %
        clear maxfinder
        %
        % Display data on-screen:
        fprintf('\nMaximum Point-Dose in Volume: %5.0f\n',maxdose);
        %
        h = ((n-initial)/interval)+1;
        maxlabel = ['maxdoses',int2str(MLCquery),'(h,1) = [maxdose];'];
        eval(maxlabel);
        shiftdata(h,1) = [n];
        clear ClinRatio *ClinicalLimits TotalSize TotalOut
        clear VoxelCheck* L Binned* TDV* maxdose
        %
    end
%
% Plotting Stuff.....
if MLCquery == 0
    shieldlabel = 'MLC 0';
    % describes initial surface position of MLC in crossplane units (mm)
    physIni = -10.3+0.2994*initial;
    % describes the shift interval in terms of real displacement (mm)
    physInt = 0.2994*interval;
    % describes final shift of MLC in crossplane units (mm)
```

```
    physExt = -10.3+0.2994*shift;
elseif MLCquery == 15
    shieldlabel = 'MLC 15';
    physIni = -10.5+0.2994*initial;
    physInt = 0.2994*interval;
    physExt = -10.5+0.2994*shift;
elseif MLCquery == 30
    shieldlabel = 'MLC 30';
    physIni = -10.7+0.2994*initial;
    physInt = 0.2994*interval;
    physExt = -10.7+0.2994*shift;
elseif MLCquery == 45
    shieldlabel = 'MLC 45';
    physIni = -10.9+0.2994*initial;
    physInt = 0.2994*interval;
    physExt = -10.9+0.2994*shift;
elseif MLCquery == 3000
    shieldlabel = 'Cerrobend 30';
    physIni = -10.7+0.2994*initial;
    physInt = 0.2994*interval;
    physExt = -10.7+0.2994*shift;
end
%
axisdef = ['xaxy',int2str(MLCquery),'(1:((',int2str(shift),'-',...
    int2str(initial),')/',int2str(interval),')+1) = [',num2str(physIni...
    ,'%+02.4f'),':',num2str(physInt,'%+02.4f'),':',num2str(physExt...
    ,'%+02.4f'),'];'];
eval(axisdef);
plotter = ['plot(xaxy',int2str(MLCquery),',maxdoses',int2str(MLCquery)...
    ,',''--ro'',''LineWidth'',2,''MarkerSize'',4,''MarkerFaceColor'',',...
    '''r'',''MarkerEdgeColor'',''r'');'];
eval(plotter);
xlim([-10 10]);
ylim([100 180]);
grid on
%
title([shieldlabel],'FontSize',16);
xlabel('Surface abutment gap (mm)','FontSize',14);
ylabel('Maximum dose (%)','FontSize',14);

clear shift* n colsize EVol VolX *data interval table* MLCquery maxlabel...
filename above* Vol* phys* hot* axisdef shieldlabel h initial plotter...
maxdose* xaxy*
% end
```

B.1.7 Hotspot volumes

```
% hotspot.m
%
% This M-file takes a relative dose volume as created by Vbut* and prompts
% the user for an upper dose value. It then creates a binary matrix via
% calling a logic statement which uses the clinical range to threshold the
```

```
% data. All values in the binary matrix are summed. Values outside the
% clinical range will contribute nothing to the sum. The percentage of the
% volume that this sum represeents is displayed on-screen.
%
% Jared Steel – 2006
% -----------------------------------------------------------------------------------------------
MLCquery = input('which angle MLC field to use for this analysis? (0 15 30 45) ');
if MLCquery == 0
   load('c:\matlab7\thesis\6X00\MLC00z.mat');
elseif MLCquery == 15
   load('c:\matlab7\thesis\6X15\MLC15z.mat');
elseif MLCquery == 30
   load('c:\matlab7\thesis\6X30\MLC30z.mat');
elseif MLCquery == 45
   load('c:\matlab7\thesis\6X45\MLC45z.mat');
elseif MLCquery == 3000
   load('c:\matlab7\thesis\6Xcerro30\cerro30z-finalcorr.mat');
elseif MLCquery ~= 0|15|30|45|3000
   error('There is no data for that MLC angle')
end
%
% Concatenate the MLC x-ray arrays
VolX = cat(3,A5,A10,A15,A20,A25,A30);%,A35);
clear A*
%
% Now load the Electron array data....and concatenate...
load('c:\matlab7\thesis\6E\electronarrays.mat');
EVol = cat(3,a05,a10,a15,a20,a25,a30);%,a35);
clear a*
%
% Define total amount of shift, and interval within to sample at...
shift = input('what amount of shift to investigate over?    ');
interval = input('what interval to sample the shift range with?  ');
initial = input('what amount of shift to start script with?     ');
%
TU = input('Set Upper Threshold dose value:          ');
%
colsize = ((shift-initial)/interval)+1;
aboveVox = zeros(colsize,1);
aboveReal = zeros(colsize,1);
abovePerCM = zeros(colsize,1);
aboveRatio = zeros(colsize,1);
   %
   for n = initial:interval:shift
      Varnamer = ['VolXshifted',num2str(n,'%02.0f'),' = VolX;'];
      eval(Varnamer);
      % Crop and Pad the X-ray volume according to a value
      % (0:interval:shift) - emulates a relative shift for adding to the
      % Electron volume...
      if n == 0
         Volcombiner0 = ['TDV',num2str(n,'%02.0f'),' = (VolXshifted',...
            num2str(n,'%02.0f'),' + EVol)/10;'];
```

```
        eval(Volcombiner0);
        clear Volcombiner0
    elseif n > 0
        Varcropper = ['VolXshifted',num2str(n,'%02.0f'),'(:,(168-',...
            int2str(n),'):167,:) = [];'];
        eval(Varcropper);
        Varpadder = ['VolXshifted',num2str(n,'%02.0f'),...
            ' = padarray(VolXshifted',num2str(n,'%02.0f'),',[0 ',...
            int2str(n),' 0],''replicate'',''pre'');'];
        eval(Varpadder);
        % Add the shifted X-ray volume to the Electron volume:
        Volcombiner = ['TDV',num2str(n,'%02.0f'),' = (VolXshifted',...
            num2str(n,'%02.0f'),' + EVol)/10;'];
        eval(Volcombiner);
        clear VolXshifted* Varnamer Varcropper Varpadder Volcombiner
    end
    %
    % Create the Binary (Logical) matrix:
    Binning1 = ['BinnedUp = TDV',num2str(n,'%02.0f'),' > TU;'];
    eval(Binning1);
    %
    clear ROIL ROIR Binning*
    %
    VolSizer = ['VolSize = numel(TDV',num2str(n,'%02.0f'),');'];
    eval(VolSizer);
    HotSize = sum(sum(sum(BinnedUp)));   % The number of Voxels in the Hotspot
    VoxSize = 0.2994*0.2994*5.0000;      % The Volume of one Voxel in mm^3
    RealSize = HotSize*VoxSize;          % Gives volume of hotspot in mm^3
    SizePerCM = RealSize/5000;           % Volume of hotspot per cm of abutment length
    HotRatio = 100*HotSize/VolSize;      % Gives percentage of volume that is Hot
    %
    % Display data on-screen:
    fprintf('\nTotal Voxels in Volume: %5.0f\n',VolSize);
    fprintf('\nTotal Voxels Above Clinical Range  = %5.0f\n',HotSize);
    fprintf('\nPercent of Volume Above Clinical Limits  = %5.2f%%\n',HotRatio);
    %
    h = ((n-initial)/interval)+1;
    aboveVox(h,1) = [HotSize];
    aboveReal(h,1) = [RealSize];
    abovePerCM(h,1) = [SizePerCM];
    aboveRatio(h,1) = [HotRatio];
    shiftdata(h,1) = [n];
    clear ClinRatio *ClinicalLimits TotalSize TotalOut VoxelCheck* L Binned* TDV*
    %
  end
%
% Plotting Stuff.....
%
if MLCquery == 0
  shieldlabel = 'MLC=0';
  physIni = -10.3+0.2994*initial;
  physInt = 0.2994*interval;
```

```
    physExt = -10.3+0.2994*shift;
elseif MLCquery == 15
    shieldlabel = 'MLC=15';
    physIni = -10.5+0.2994*initial;
    physInt = 0.2994*interval;
    physExt = -10.5+0.2994*shift;
elseif MLCquery == 30
    shieldlabel = 'MLC=30';
    physIni = -10.7+0.2994*initial;
    physInt = 0.2994*interval;
    physExt = -10.7+0.2994*shift;
elseif MLCquery == 45
    shieldlabel = 'MLC=45';
    physIni = -10.9+0.2994*initial;
    physInt = 0.2994*interval;
    physExt = -10.9+0.2994*shift;
elseif MLCquery == 3000
    shieldlabel = 'Cerrobend=30';
    physIni = -10.7+0.2994*initial;
    physInt = 0.2994*interval;
    physExt = -10.7+0.2994*shift;
end
%
axisdef = ['xaxy(1:((',int2str(shift),'-',int2str(initial),')/',...
    int2str(interval),')+1) = [',num2str(physIni,'%+02.4f'),':',...
    num2str(physInt,'%+02.4f'),':',num2str(physExt,'%+02.4f'),'];'];
eval(axisdef);
plot(xaxy,abovePerCM,'-k');
ylim([0 7]);
grid on
%
title({['Hotspot volume below 5mm depth'];[', Threshold =',int2str(TU),'%']}...
    ,'FontSize',16);
xlabel('Abutment Gap (mm)','FontSize',14);
ylabel('Volume (cm^3) per unit Abutment length (cm)','FontSize',14);
filename = ['C:\matlab7\thesis\mergetest\images\hotspot',...
    int2str(MLCquery),'thresh',int2str(TU),'.png']
%print('-dpng', filename,'-zbuffer','-r75');
%close all
clear shift* n colsize TU TL EVol VolX *data interval table* MLCquery filename
%
```

B.1.8 Minimum dose at dmax

```
% maxcold.m
%
% Determines minimum dose in composite dataset. Reiterates over a
% user-defined abutment gap range at a user-defined sampling resolution.
%
% Jared Steel – 2006
% -----------------------------------------------------------------------------------------
MLCquery = input...
```

```
    ('which angle MLC field to use for this analysis? (0 15 30 45 / 3000) ');
if MLCquery == 0
    load('c:\matlab7\thesis\6X00\MLC00z.mat');
elseif MLCquery == 15
    load('c:\matlab7\thesis\6X15\MLC15z.mat');
elseif MLCquery == 30
    load('c:\matlab7\thesis\6X30\MLC30z.mat');
elseif MLCquery == 45
    load('c:\matlab7\thesis\6X45\MLC45z.mat');
elseif MLCquery == 3000
    load('c:\matlab7\thesis\6Xcerro30\cerro30z-finalcorr.mat');
elseif MLCquery ~= 0|15|30|45|3000
    error('There is no data for that MLC angle')
end
%
% Concatenate the MLC x-ray arrays
Xd15 = A15;
clear A*
%
% Now load the electron array data....and concatenate...
load('c:\matlab7\thesis\6E\electronarrays.mat');
Ed15 = a15;
clear a*
%
% Define total amount of shift, and interval within to sample at...
shift = input('what amount of shift to investigate over?    ');
interval = input('what interval to sample the shift range with?  ');
initial = input('what amount of shift to start script with?     ');
%
colsize = ((shift-initial)/interval)+1;
maxdoses = zeros(colsize,1);
    %
    for n = initial:interval:shift
        Varnamer = ['Xshifted',num2str(n,'%02.0f'),' = Xd15;'];
        eval(Varnamer);
        % Crop and pad the X-ray volume according to a value
        % (0:interval:shift) - emulates a relative shift for adding to the
        % electron volume...
        if n == 0
            Volcombiner0 = ['TDA',num2str(n,'%02.0f'),' = (Xshifted',...
                num2str(n,'%02.0f'),' + Ed15)/10;'];
            eval(Volcombiner0);
            clear Volcombiner0
        elseif n > 0
            Varcropper = ['Xshifted',num2str(n,'%02.0f'),'(:,(168-',...
                int2str(n),'):167) = [];'];
            eval(Varcropper);
            Varpadder = ['Xshifted',num2str(n,'%02.0f'),' = padarray(Xshifted',...
                num2str(n,'%02.0f'),',[0 ',int2str(n),'],''replicate'',''pre'');'];
            eval(Varpadder);
            % Add the shifted X-ray volume to the electron volume:
            Volcombiner = ['TDA',num2str(n,'%02.0f'),' = (Xshifted',...
                num2str(n,'%02.0f'),' + Ed15)/10;'];
```

```
            eval(Volcombiner);
            clear Xshifted* Varnamer Varcropper Varpadder Volcombiner
        end
        %
        % Find the minimum point dose:
        minfinder = ['mindose = min(min(min(TDA',num2str(n,'%02.0f'),'')));'];
        eval(minfinder);
        %
        clear minfinder
        %
        % Display data on-screen:
        fprintf('\nColdest Point-Dose at Dmax: %5.0f\n',mindose);
        %
        h = ((n-initial)/interval)+1;
        minlabeller = ['mindoses',int2str(MLCquery),'(h,1) = [mindose];'];
        eval(minlabeller);
        shiftdata(h,1) = [n];
        clear ClinRatio *ClinicalLimits TotalSize TotalOut VoxelCheck* L...
            Binned* TDV* minlabeller
        %
    end
%
% Plotting stuff.....
if MLCquery == 0
    shieldlabel = 'MLC=0';
    physIni = -10.3+0.2994*initial;
    physInt = 0.2994*interval;
    physExt = -10.3+0.2994*shift;
    color = 'b';
elseif MLCquery == 15
    shieldlabel = 'MLC=15';
    physIni = -10.5+0.2994*initial;
    physInt = 0.2994*interval;
    physExt = -10.5+0.2994*shift;
    color = 'g';
elseif MLCquery == 30
    shieldlabel = 'MLC=30';
    physIni = -10.7+0.2994*initial;
    physInt = 0.2994*interval;
    physExt = -10.7+0.2994*shift;
    color = 'm';
elseif MLCquery == 45
    shieldlabel = 'MLC=45';
    physIni = -10.9+0.2994*initial;
    physInt = 0.2994*interval;
    physExt = -10.9+0.2994*shift;
    color = 'r';
elseif MLCquery == 3000
    shieldlabel = 'Cerrobend=30';
    physIni = -10.7+0.2994*initial;
    physInt = 0.2994*interval;
    physExt = -10.7+0.2994*shift;
    color = 'k';
```

```
end
%
axisdef = ['xaxy',int2str(MLCquery),'(1:((',int2str(shift),'-',...
    int2str(initial),')/',int2str(interval),')+1) = [',num2str(physIni,...
    '%+02.4f'),':',num2str(physInt,'%+02.4f'),':',num2str(physExt,...
    '%+02.4f'),'];'];
eval(axisdef);
plotter = ['plot(xaxy',int2str(MLCquery),',mindoses',int2str(MLCquery),...
    ',color,''LineWidth'',2);'];
eval(plotter);
xlim([-11 11]);
grid on
%
title({['Minimum Point-Dose at Dmax'];[shieldlabel]},'FontSize',16);
xlabel('Abutment Gap (mm)','FontSize',14);
ylabel('Relative Dose (%)','FontSize',14);
%filename = ['C:\matlab7\thesis\mergetest\images\vol',int2str(MLCquery),...
%   'thresh',int2str(TU),'.png']
%print('-dpng', filename,'-zbuffer','-r75');
%close all
clear shift* n colsize TU TL EVol VolX *data interval table* MLCquery...
    filename above* Vol* phys* hot* axisdef maxdoses shieldlabel h initial...
    TDA* *d15 color plotter
% end
```

B.1.9 Percentage depth-dose normalisation

```
% plotbinz4.m
%
% Compliles composites dose volumes, selects VOI relative to photon beam edge geometry,
% and compares the dosimetry to electron PDD data for the relevant depth. Plots results.
%
% Jared Steel - 2006
% -----------------------------------------------------------------------------------------
MLCquery = input(...
'which angle MLC field to use for this analysis? (0 15 30 45, for Cerrobend use
3000) ');
if MLCquery == 0
    load('c:\matlab7\thesis\6X00\MLC00z.mat');
    load('c:\matlab7\thesis\mergetest\Midleafpos00.mat');
elseif MLCquery == 15
    load('c:\matlab7\thesis\6X15\MLC15z.mat');
    load('c:\matlab7\thesis\mergetest\Midleafpos15.mat');
elseif MLCquery == 30
    load('c:\matlab7\thesis\6X30\MLC30z.mat');
    load('c:\matlab7\thesis\mergetest\Midleafpos30.mat');
elseif MLCquery == 45
    load('c:\matlab7\thesis\6X45\MLC45z.mat');
    load('c:\matlab7\thesis\mergetest\Midleafpos45.mat');
elseif MLCquery == 3000
    load('c:\matlab7\thesis\6Xcerro30\cerro30z-finalcorr.mat');
    load('c:\matlab7\thesis\mergetest\Midleafpos30.mat');
```

```
elseif MLCquery ~= 0|15|30|45|3000
   error('There is no data for that MLC angle')
end
%
load('c:\matlab7\thesis\6E\electronarrays.mat');
load('c:\matlab7\thesis\depthdosedata.mat'); % brings in variables: dd6E & dd6X
%
% Define total amount of shift, and interval within to sample at...
shift      = input('what amount of shift to investigate over?      ');
interval   = input('what interval to sample the shift range with?  ');
%
colsize = (shift/3)+1;
for num = 1:7
   p1 = ['perXover',int2str(num),' = zeros(colsize,1);'];
   p2 = ['perEover',int2str(num),' = zeros(colsize,1);'];
   p3 = ['perXunder',int2str(num),' = zeros(colsize,1);'];
   p4 = ['perEunder',int2str(num),' = zeros(colsize,1);'];
   eval([p1,p2,p3,p4]);
end
%
aboveXdata  = zeros(colsize,1);
belowXdata  = zeros(colsize,1);
aboveEdata  = zeros(colsize,1);
belowEdata  = zeros(colsize,1);
withinXdata = zeros(colsize,1);
withinEdata = zeros(colsize,1);
shiftdata = zeros(colsize,1);
%
setthresh = input('what +/- threshold limits to set?    ');
for n = 0:interval:shift
   if n == 0       % This part adds the xray fields to the E fields for zero shift.
      for layer = 05:5:30
         layeradd = ['L',int2str(layer),' = (A',int2str(layer),' +
a',num2str(layer,'%02.0f'),')/10;'];
         eval(layeradd);
      end
   elseif n > 0    % This part simulates xray field shift by cropping and padding, then adds to the
E fields.
      for layer = 05:5:30
         xlayercopy  = ['Lx',int2str(layer),' = A',int2str(layer),';'];
         xlayercrop  = ['Lx',int2str(layer),'(:,(168-',int2str(n),'):167) = [];'];
         xlayerpad   = ['Lx',int2str(layer),' = padarray(Lx',int2str(layer),',[0
',int2str(n),',...
        '],''replicate'',''pre'');'];
         layeradd    = ['L',int2str(layer),' = (Lx',int2str(layer),' +
a',num2str(layer,'%02.0f'),')/10;'];
         eval([xlayercopy,xlayercrop,xlayerpad,layeradd]);
         % We now have 7 combined field layers "L*".
      end
   end
   %
   for layer = 5:5:30
      level = layer/5;
```

```
        % Next we want to define our ROI limits based on a pre-specified
        % ammount either side of the shifted MLC midleaf point. NB
        % MLC45midcols(*) locates the midleaf point of the divergent MLC
        % leaves through depth.
        if MLCquery == 3000
            Cerroangle = 30;
            roilimit1 = ['ROI_E_L',int2str(level),' =
MLC',int2str(Cerroangle),'midcolz(',int2str(level),...
           ')+',int2str(n),'-28;'];
            roilimit2 = ['ROI_X_L',int2str(level),' =
MLC',int2str(Cerroangle),'midcolz(',int2str(level),...
           ')+',int2str(n),'+28;'];
            eval([roilimit1,roilimit2]);
        else
            roilimit1 = ['ROI_E_L',int2str(level),' =
MLC',int2str(MLCquery),'midcolz(',int2str(level),...
           ')+',int2str(n),'-28;'];
            roilimit2 = ['ROI_X_L',int2str(level),' =
MLC',int2str(MLCquery),'midcolz(',int2str(level),...
           ')+',int2str(n),'+28;'];
            eval([roilimit1,roilimit2]);
        end
        %
        % We crop each copied L-layer down to a ROI either side of the MLC
        % midleaf point: xray side, and electron field side...
        if MLCquery == 3000
            Cerroangle = 30;
            roicutter1a = ['region_E',int2str(level),'=
L',int2str(layer),'(:,MLC',int2str(Cerroangle)...
           ,'midcolz(',int2str(level),')+',int2str(n),'-28:MLC',int2str(Cerroangle)...
           ,'midcolz(',int2str(level),')+',int2str(n),'-1);'];
            eval(roicutter1a);
            roicutter2a = ['region_X',int2str(level),'=
L',int2str(layer),'(:,MLC',int2str(Cerroangle)...
           ,'midcolz(',int2str(level),')+',int2str(n),':MLC',int2str(Cerroangle)...
           ,'midcolz(',int2str(level),')+',int2str(n),'+27);'];
            eval(roicutter2a);
        else
            roicutter1a = ['region_E',int2str(level),'=
L',int2str(layer),'(:,MLC',int2str(MLCquery)...
           ,'midcolz(',int2str(level),')+',int2str(n),'-28:MLC',int2str(MLCquery)...
           ,'midcolz(',int2str(level),')+',int2str(n),'-1);'];
            eval(roicutter1a);
            roicutter2a = ['region_X',int2str(level),'=
L',int2str(layer),'(:,MLC',int2str(MLCquery)...
           ,'midcolz(',int2str(level),')+',int2str(n),':MLC',int2str(MLCquery)...
           ,'midcolz(',int2str(level),')+',int2str(n),'+27);'];
            eval(roicutter2a);
        end
        %
        clear roi* ROI*
        %
        normtodepthdoseE = ['normdE',int2str(level),'=
```

```
region_E',int2str(level),'/dd6E(',int2str(level),');'];
      normtodepthdoseX = ['normdX',int2str(level),'=
region_X',int2str(level),'/dd6X(',int2str(level),');'];
      eval(normtodepthdoseE);
      eval(normtodepthdoseX);
      %
      globalhilim = 1.000+(setthresh/100);    % set threshold levels to +/-x
      globallolim = 1.000-(setthresh/100);
      %
      BinningEup = ['BinnedUpE',int2str(level),'     = normdE',int2str(level),'>
globalhilim;'];
      BinningEdn = ['BinnedDownE',int2str(level),'    = normdE',int2str(level),'<=
globallolim;'];
      BinningXup = ['BinnedUpX',int2str(level),'     = normdX',int2str(level),'>
globalhilim;'];
      BinningXdn = ['BinnedDownX',int2str(level),'    = normdX',int2str(level),'<=
globallolim;'];
      eval([BinningEup,BinningEdn,BinningXup,BinningXdn]);
      %
      clear Binning*
      %
      totalpixels = numel(region_X1);
      levelpercentsXover  = ['Xover',int2str(level),  ' =
100*sum(sum(BinnedUpX',...
     int2str(level),'))   /totalpixels;'];
      levelpercentsXunder = ['Xunder',int2str(level), ' =
100*sum(sum(BinnedDownX',...
     int2str(level),')) /totalpixels;'];
      levelpercentsEover  = ['Eover',int2str(level),  ' =
100*sum(sum(BinnedUpE',...
     int2str(level),'))   /totalpixels;'];
      levelpercentsEunder = ['Eunder',int2str(level), ' =
100*sum(sum(BinnedDownE',...
     int2str(level),')) /totalpixels;'];

eval([levelpercentsXover,levelpercentsXunder,levelpercentsEover,levelpercentsEund
er]);
      clear levelper*
      %
      %
   end
   %
   %
   binvol1 = ['XBinnedup',int2str(n),...
   ' =
cat(3,BinnedUpX1,BinnedUpX2,BinnedUpX3,BinnedUpX4,BinnedUpX5,BinnedUpX6);'
];
   binvol2 = ['EBinnedup',int2str(n),...
   ' =
cat(3,BinnedUpE1,BinnedUpE2,BinnedUpE3,BinnedUpE4,BinnedUpE5,BinnedUpE6);'
];
   binvol3 = ['XBinneddn',int2str(n),...
   ' =
```

```
cat(3,BinnedDownX1,BinnedDownX2,BinnedDownX3,BinnedDownX4,BinnedDownX5,
BinnedDownX6);'];
   binvol4 = ['EBinneddn',int2str(n),...
   ' =
cat(3,BinnedDownE1,BinnedDownE2,BinnedDownE3,BinnedDownE4,BinnedDownE5,
BinnedDownE6);'];
   eval([binvol1,binvol2,binvol3,binvol4]);
   clear Binned* binvol*
   Xabove = ['AboveExpectedX =
(sum(sum(sum(XBinnedup',int2str(n),'))/32732)*100;'];
   Xbelow = ['BelowExpectedX =
(sum(sum(sum(XBinneddn',int2str(n),'))/32732)*100;'];
   Eabove = ['AboveExpectedE =
(sum(sum(sum(EBinnedup',int2str(n),'))/32732)*100;'];
   Ebelow = ['BelowExpectedE =
(sum(sum(sum(EBinneddn',int2str(n),'))/32732)*100;'];
   eval([Xabove,Xbelow,Eabove,Ebelow]);
   %
   Xwithinbin = 100-AboveExpectedX-BelowExpectedX;
   Ewithinbin = 100-AboveExpectedE-BelowExpectedE;
   %
   h = (n/3)+1;
   for Num = 1:6
      P1 = ['perXover',int2str(Num),'(h,1) = [Xover',int2str(Num),'];'];
      P2 = ['perEover',int2str(Num),'(h,1) = [Eover',int2str(Num),'];'];
      P3 = ['perXunder',int2str(Num),'(h,1) = [Xunder',int2str(Num),'];'];
      P4 = ['perEunder',int2str(Num),'(h,1) = [Eunder',int2str(Num),'];'];
      eval([P1,P2,P3,P4]);
   end
   %
   aboveXdata(h,1) = [AboveExpectedX];
   belowXdata(h,1) = [BelowExpectedX];
   aboveEdata(h,1) = [AboveExpectedE];
   belowEdata(h,1) = [BelowExpectedE];
   withinXdata(h,1) = [Xwithinbin];
   withinEdata(h,1) = [Ewithinbin];
   shiftdata(h,1) = [n];
   %
   %
   clear L* layer level SD* STD* %region*
end
%
clear A* xlayer* layer* colsize h n interval shift TU* TL*
%
% Plotting Stuff.....
if MLCquery == 0
   xaxy(1:24) = [-10.3:0.9:10.4];
elseif MLCquery == 15
   xaxy(1:24) = [-10.5:0.9:10.2];
elseif MLCquery == 30
   xaxy(1:24) = [-10.7:0.9:10.0];
elseif MLCquery == 45
   xaxy(1:24) = [-10.9:0.9:9.8];
```

```
elseif MLCquery == 3000
   xaxy(1:24) = [-10.7:0.9:10.0];
end


figure
plot(xaxy,aboveXdata,'--
rx','LineWidth',2,'MarkerSize',4,'MarkerFaceColor','r','MarkerEdgeColor','r');
if MLCquery == 3000
   title(['Distribution of Dose vs. Abutment Conditions (Xray ROI)
Cerrobend'],'FontSize',11);
else
   title(['Distribution of Dose vs. Abutment Conditions (Xray ROI) MLC =
',int2str(MLCquery)],'FontSize',11);
end
ylim([0 100]);
xlim([-11 10]);
grid on
hold on
plot(xaxy,belowXdata,'--
bx','LineWidth',2,'MarkerSize',4,'MarkerFaceColor','b','MarkerEdgeColor','b');
xlabel('Abutment Gap (mm)','FontSize',11);
ylabel('% of Total Pixels within ROI''s','FontSize',11);
ylim([0 100]);
hold on
plot(xaxy,withinXdata,'--
gx','LineWidth',2,'MarkerSize',4,'MarkerFaceColor','g','MarkerEdgeColor','g');
ylim([0 100]);
xlim([-11 10]);
legend(['over ',int2str(setthresh),'%'],['under ',int2str(setthresh),'%'],'within
limits');
hold off
%
figure
plot(xaxy,aboveEdata,'--
rd','LineWidth',2,'MarkerSize',4,'MarkerFaceColor','r','MarkerEdgeColor','r');
if MLCquery == 3000
   title(['Distribution of Dose vs. Abutment Conditions (Electron ROI)
Cerrobend'],'FontSize',11);
else
   title(['Distribution of Dose vs. Abutment Conditions (Electron ROI) MLC =
',int2str(MLCquery)],'FontSize',11);
end
ylim([0 105]);
xlim([-11 10]);
grid on
hold on
plot(xaxy,belowEdata,'--
bd','LineWidth',2,'MarkerSize',4,'MarkerFaceColor','b','MarkerEdgeColor','b');
xlabel('Abutment Gap (mm)','FontSize',11);
ylabel('% of Total Pixels within ROI''s','FontSize',11);
ylim([0 100]);
xlim([-11 10]);
```

```
hold on
plot(xaxy,withinEdata,'--
gx','LineWidth',2,'MarkerSize',4,'MarkerFaceColor','g','MarkerEdgeColor','g');
ylim([0 105]);
xlim([-11 10]);
legend(['over ',int2str(setthresh),'%'],['under ',int2str(setthresh),'%'],'within
limits');
hold off
%
%
lws = 'LineWidth';
mss = 'MarkerSize';
%
figure
plot(xaxy,perXover1,'-rx',xaxy,perXover2,'-mx',xaxy,perXover3,'-
yx',xaxy,perXover4...
    ,'-gx',xaxy,perXover5,'-cx',xaxy,perXover6,'-bx','LineWidth',1,'MarkerSize',4);
title(['Over +',int2str(setthresh),'% threshold X-rays, MLC = ',int2str(MLCquery)]);
xlabel('Abutment gap (mm)');
ylabel('Number of pixels (%)');
ylim([0 105]);
xlim([-11 10]);
legend('5mm','10mm','15mm','20mm','25mm','30mm');
%
figure
plot(xaxy,perEover1,'-ro',xaxy,perEover2,'-mo',xaxy,perEover3,'-
yo',xaxy,perEover4...
    ,'-go',xaxy,perEover5,'-co',xaxy,perEover6,'-bo','LineWidth',1,'MarkerSize',4);
title(['Over +',int2str(setthresh),'% threshold Electrons, MLC =
',int2str(MLCquery)]);
xlabel('Abutment gap (mm)');
ylabel('Number of pixels (%)');
ylim([0 105]);
xlim([-11 10]);
legend('5mm','10mm','15mm','20mm','25mm','30mm','Location','SouthWest');
%
figure
plot(xaxy,perXunder1,'-rx',xaxy,perXunder2,'-mx',xaxy,perXunder3,'-
yx',xaxy,perXunder4...
    ,'-gx',xaxy,perXunder5,'-cx',xaxy,perXunder6,'-bx','LineWidth',1,'MarkerSize',4);
title(['Under -',int2str(setthresh),'% threshold X-rays, MLC =
',int2str(MLCquery)]);
xlabel('Abutment gap (mm)');
ylabel('Number of pixels (%)');
ylim([0 105]);
xlim([-11 10]);
legend('5mm','10mm','15mm','20mm','25mm','30mm');
%
figure
plot(xaxy,perEunder1,'-ro',xaxy,perEunder2,'-mo',xaxy,perEunder3,'-
yo',xaxy,perEunder4...
    ,'-go',xaxy,perEunder5,'-co',xaxy,perEunder6,'-bo','LineWidth',1,'MarkerSize',4);
title(['Under -',int2str(setthresh),'% threshold Electrons, MLC =
```

```
',int2str(MLCquery)]);
xlabel('Abutment gap (mm)');
ylabel('Number of pixels (%)');
ylim([0 105]);
xlim([-11 10]);
legend('5mm','10mm','15mm','20mm','25mm','30mm','Location','NorthWest');
%
clear per* *over* *under* *todepthdose* ans a05 a10 a15 a20 a25 a30 a35
normd* MLC* *above *below...
   global* *Expected* *withinbin region* *Binned*
% end
```

B.1.10 Exportation of scan data to VTK

```
function writevtkdata(M,outputvtkfile)
%WRITEVTKDATA: writes MATLAB data to ASCII .vtk format files.
%   INPUT: M is a 3D matrix
%        OUTPUTVTKFILE is the output file name (string) eg.
%       'C:\work\outfile.vtk'
%
% close all;
disp(datestr(now))
%
% Get the dimensions of the matrix and the number of points in it
[a b c] = size(M);
npoints = a*b*c;
%
% write the header. To change spacing, do it manually in WRITEVTKHEADER
writeVTKheader(a,b,c,outputvtkfile,0)
%
%Write matrix to file
 for z = 1:c
    fprintf('Writing Slice %i data to %s\n', z, outputvtkfile)
    for y = 1:b
       for x = 1:a

      dlmwrite(outputvtkfile,...
         M(x,y,z), '-append', 'delimiter', ' ', 'precision', '%.3f', 'newline', 'pc');

   end
  end
 end
 %
fprintf('\nFinished writing data to file\n', z)
disp(datestr(now))
% end

function [] = writeVTKheader(W,H,D,vtkfile,binOrASCII);
% Used to format the VTK scan data so can be read as "structured points" data in the Tcl
% interpretive language. Function called from writevtkdata.m.
%   dim:       The 1x3 matrix of volume dimensions
%   vtkfile:    The output filename (string)
```

```
%   binOrASCII: int flag 1 = binary, 0 = ASCII format
%
%   It is possible to save as 8 bit data or 16 bit data,
%   see saveAsVTK.m
%
% Erik Vidholm 2005
%
% dimensions
WHD = W*H*D;
%
% open output file
fid = fopen( vtkfile, 'w');
%
% write header
fprintf(fid, '%s\n', '# vtk DataFile Version 5.0');
fprintf(fid, '%s\n', 'A MATRIX');
if binOrASCII == 1
 fprintf(fid, '%s\n', 'BINARY');
else
 fprintf(fid, '%s\n', 'ASCII');
end
fprintf(fid, '%s\n', 'DATASET STRUCTURED_POINTS');
fprintf(fid, '%s%d%c%d%c%d \n', 'DIMENSIONS ', W, ' ',H, ' ',D);
fprintf(fid, '%s%0.1f%c%0.1f%c%0.1f \n', 'ORIGIN ', 0.0, ' ',0.0, ' ',0.0);
fprintf(fid, '%s%0.1f%c%0.1f%c%0.1f \n', 'SPACING ', 1.0, ' ',1.0, ' ',1.0);
fprintf(fid, '%s%d \n', 'POINT_DATA ', WHD);
%
fprintf(fid, '%s\n', 'SCALARS scalars1 float');
fprintf(fid, '%s\n', 'LOOKUP_TABLE default');
%
%close output file
fclose(fid);
% end
```

B.1.11 Converting optical density to relative dose

```
% od2dose.m
%
% This m-file is an experimental translator between OD arrays (as scanned
% on the VIDAR or Wellhofer densitomtery) and dose. Thisscript takes each
% entry in the OD image array/vector and converts it via an exponential
% function, and then places the result into the 'dosearray' image/vector.
% Note that the function really converts from OD to MU's, but this can be
% taken as 'relative dose' since the MU:dose relationship is linear.Therefore
% the resultant array only needs renormalising to give relative dose.
%
% Jared Steel – 2006
% -----------------------------------------------------------------------------
ODarray = (double(input('which OD array to convert?  ')));
dims = size(ODarray);
```

```
dimx = dims(1);
dimy = dims(2);
%
MUprof = zeros(dimx,dimy);
%
% Now to sample and translate each entry...
for x = 1:dimx
   for y = 1:dimy
      entry = ODarray(x,y);
     % Exponential function determined from sensitometry:
      MUex = 13.03*exp(0.6707*entry)-13.16*exp(-0.6182*entry);
      MUprof(x,y) = [MUex];
      clear MUZ entry MUex
   end
end
clear dim* x y ODarray
% end
```

B.2 VTK routines

B.2.1 Image plane through x-y-z and variable isosurface

The script below describes the process for viewing and manipulating the relative dose scan volume at a set abutment gap and shielding conditions (as composed in MATLAB®). Manipulation of abutment conditions was done in the MATLAB® workspace, while VTK was used only to view the resulting dosimetry. Here the script calls the initial abutment (-10.9 mm gap) data generated in the dataset involving MLC at 45°. We view through two methods: by x-y-z planar interrogation; and generation of an isosurface. The viewing of multiple isosurfaces is similar to the process described below, in fact simpler, as the GUI controls are removed, and the routine set for multiple dose values as defined only in the script.

```
package require vtk
package require vtkinteraction

# This script uses the vtkImagePlaneWidget to probe a 3D image
# dataset with three orthogonal planes.  Buttons are provided to:
#
# We also generate and render an isosurface that's value is defined
# on a horizontal slider in the GUI. The start value of this is set at
# 110% relative dose.

vtkStructuredPointsReader v16
  v16 SetFileName "C:/MatLab7/Thesis/Mergetest/VTK/M0.vtk"
  v16 Update
```

```
scan [[v16 GetOutput] GetWholeExtent] "%d %d %d %d %d %d" \
      xMin xMax yMin yMax zMin zMax
      puts " $xMin $xMax $yMin $yMax $zMin $zMax"

set spacing [[v16 GetOutput] GetSpacing]
set sx [lindex $spacing 0]
set sy [lindex $spacing 1]
set sz [lindex $spacing 2]

set origin [[v16 GetOutput] GetOrigin]
set ox [lindex $origin 0]
set oy [lindex $origin 1]
set oz [lindex $origin 2]

# An outline is shown for context.
vtkOutlineFilter outline
  outline SetInput [v16 GetOutput]

vtkPolyDataMapper outlineMapper
  outlineMapper SetInput [outline GetOutput]

vtkActor outlineActor
  outlineActor SetMapper outlineMapper

# The shared picker enables us to use 3 planes at one time
# and gets the picking order right
vtkCellPicker picker
  picker SetTolerance 0.005

vtkLookupTable alphalut
    alphalut SetNumberOfTableValues 256
    alphalut SetHueRange 0.1 1
    alphalut SetSaturationRange 0.0 1.0
    alphalut SetValueRange 0.0 1.0
    alphalut SetAlphaRange 0.2 0.8
    alphalut SetRampToSCurve
    alphalut Build

# The 3 image plane widgets are used to probe the dataset.
vtkImagePlaneWidget planeWidgetX
  planeWidgetX DisplayTextOn
  planeWidgetX SetInput [v16 GetOutput]
  planeWidgetX SetPlaneOrientationToXAxes
  planeWidgetX SetSliceIndex 52
  planeWidgetX SetPicker picker
  planeWidgetX SetKeyPressActivationValue "x"
  planeWidgetX SetLookupTable alphalut
  set prop1 [planeWidgetX GetPlaneProperty]
  $prop1 SetColor 1 0 0

vtkImagePlaneWidget planeWidgetY
```

```
  planeWidgetY DisplayTextOn
  planeWidgetY SetInput [v16 GetOutput]
  planeWidgetY SetPlaneOrientationToYAxes
  planeWidgetY SetSliceIndex 52
  planeWidgetY SetPicker picker
  planeWidgetY SetKeyPressActivationValue "y"
  set prop2 [planeWidgetY GetPlaneProperty]
  $prop2 SetColor 1 1 0
  planeWidgetY SetLookupTable [planeWidgetX GetLookupTable]

vtkImagePlaneWidget planeWidgetZ
  planeWidgetZ DisplayTextOn
  planeWidgetZ SetInput [v16 GetOutput]
  planeWidgetZ SetPlaneOrientationToZAxes
  planeWidgetZ SetSliceIndex 6
  planeWidgetZ SetPicker picker
  planeWidgetZ SetKeyPressActivationValue "z"
  set prop3 [planeWidgetZ GetPlaneProperty]
  $prop3 SetColor 0 0 1
  planeWidgetZ SetLookupTable [planeWidgetX GetLookupTable]

set current_widget planeWidgetZ
set mode_widget  planeWidgetZ

# Once generated, a vtkPolyDataNormals filter is
# is used to create normals for smooth surface shading during rendering.
# The triangle stripper is used to create triangle strips from the
# isosurface these render much faster on many systems.
vtkContourFilter skinExtractor
  skinExtractor SetInput  [v16 GetOutput]
  skinExtractor SetValue 0 500
vtkPolyDataConnectivityFilter connect
  connect SetInput [skinExtractor GetOutput]
  connect SetExtractionModeToAllRegions
vtkSmoothPolyDataFilter smoother
  smoother SetInput [connect GetOutput]
  eval smoother SetNumberOfIterations 100
  eval smoother SetFeatureAngle 90
  smoother FeatureEdgeSmoothingOn
  smoother BoundarySmoothingOn
  smoother SetConvergence 0
  [smoother GetOutput] ReleaseDataFlagOn
vtkPolyDataNormals skinNormals
  skinNormals SetInput [smoother GetOutput]
  skinNormals SetFeatureAngle 70.0
vtkPolyDataMapper skinMapper
  skinMapper SetInput [skinNormals GetOutput]
  skinMapper SetLookupTable alphalut
  skinMapper ScalarVisibilityOff
vtkActor skin
  skin SetMapper skinMapper
  [skin GetProperty] SetSpecular .8
```

```
  [skin GetProperty] SetSpecularPower 50
  [skin GetProperty] SetDiffuse .7

# Create the RenderWindow and Renderer
vtkRenderer ren1
vtkRenderWindow renWin
  renWin AddRenderer ren1

# Add the outline actor to the renderer, set the background color and size
ren1 AddActor skin
ren1 AddActor outlineActor
renWin SetSize 600 600
ren1 SetBackground  0.2 0.4 0.5

# Create the GUI
wm withdraw .
toplevel .top
wm title .top "VTK Isodose surface and XYZ planes"
wm protocol .top WM_DELETE_WINDOW ::vtk::cb_exit

set popm [menu .top.mm -tearoff 0]
set mode 1
$popm add radiobutton -label "nearest" -variable mode -value 0  \
        -command SetInterpolation
$popm add radiobutton -label "linear" -variable mode -value 1  \
        -command SetInterpolation
$popm add radiobutton -label "cubic" -variable mode -value 2  \
        -command SetInterpolation

set display_frame [frame .top.f1]

set ctrl_buttons [frame .top.btns]

pack $display_frame $ctrl_buttons \
      -side top -anchor n \
      -fill both -expand f

set quit_button [button $ctrl_buttons.btn1  \
      -text "Quit" \
      -command  ::vtk::cb_exit]

set capture_button [button $ctrl_buttons.btn2  \
      -text "PNG it!" \
      -command CaptureImage]

set x_button [button $ctrl_buttons.btn3  \
      -text "x" \
      -command AlignXaxis]

set y_button [button $ctrl_buttons.btn4  \
      -text "y" \
      -command AlignYaxis]
```

```
set z_button [button $ctrl_buttons.btn5  \
      -text "z" \
      -command AlignZaxis]

set last_btn -1
bind $x_button <Button-3> "set last_btn 0; configMenu; $popm post %X
%Y"
bind $y_button <Button-3> "set last_btn 1; configMenu; $popm post %X
%Y"
bind $z_button <Button-3> "set last_btn 2; configMenu; $popm post %X
%Y"

# Share the popup menu among buttons, keeping
# track of associated widget's interpolation mode
proc configMenu { } {
 global last_btn popm mode mode_widget
 if { $last_btn == 0 } {
  set mode_widget planeWidgetX
 } elseif { $last_btn == 1 } {
  set mode_widget planeWidgetY
 } else {
  set mode_widget planeWidgetZ
 }
 set mode [$mode_widget GetResliceInterpolate]
 $popm entryconfigure $last_btn -variable mode
}

pack $quit_button $capture_button $x_button $y_button $z_button \
      -side left \
      -expand t -fill both

# Create the render widget
set renderer_frame [frame $display_frame.rFm]

pack $renderer_frame \
      -padx 3 -pady 3 \
      -side left -anchor n \
      -fill both -expand f

set render_widget [vtkTkRenderWidget $renderer_frame.r \
      -width 980 \
      -height 560 \
      -rw renWin]

pack $render_widget $display_frame  \
      -side top -anchor n \
      -fill both -expand f

# Add a slice scale to browse the current slice stack
set slice_number [$current_widget GetSliceIndex]
```

```
scale .top.slice \
      -from $zMin \
      -to $zMax \
      -orient horizontal \
      -command SetSlice \
      -variable slice_number \
      -label "Slice"

pack .top.slice \
      -fill x -expand f

proc SetSlice {slice} {
  global current_widget
  $current_widget SetSliceIndex $slice
  ren1 ResetCameraClippingRange
  renWin Render
}

# Add a surface scale to browse the current isodose values
set surf_number 1100

scale .top.surf \
      -from 200 \
      -to 1705 \
      -res 5.0 \
      -orient horizontal \
      -command SetSurf \
      -variable surf_number \
      -label "IsoDose"

pack .top.surf \
      -fill x -expand f

proc SetSurf {surf} {
  global current_widget
  skinExtractor SetValue 0 $surf
  [skin GetProperty] SetDiffuseColor [expr $surf/800] [expr $surf/500] [expr
$surf/100]
  renWin Render
}

::vtk::bind_tk_render_widget $render_widget
# Set the interactor for the widgets
set iact [[$render_widget GetRenderWindow] GetInteractor]
planeWidgetX SetInteractor $iact
planeWidgetX On
planeWidgetY SetInteractor $iact
planeWidgetY On
planeWidgetZ SetInteractor $iact
planeWidgetZ On

# Create an initial interesting view
```

```
set cam1 [ren1 GetActiveCamera]
$cam1 Elevation 90
$cam1 SetViewUp 0 0 -1
$cam1 Azimuth 90
ren1 ResetCameraClippingRange

# Render it
$render_widget Render

# Align the camera so that it faces the desired widget
proc AlignCamera { } {
  global ox oy oz sx sy sz xMax xMin yMax yMin zMax zMin slice_number
  global current_widget
  set cx [expr $ox + (0.5*($xMax - $xMin))*$sx]
  set cy [expr $oy + (0.5*($yMax - $yMin))*$sy]
  set cz [expr $oy + (0.5*($zMax - $zMin))*$sz]
  set vx 0
  set vy 0
  set vz 0
  set nx 0
  set ny 0
  set nz 0
  set iaxis [$current_widget GetPlaneOrientation]
  if { $iaxis == 0 } {
    set vz -1
    set nx [expr $ox + $xMax*$sx]
    set cx [expr $ox + $slice_number*$sx]
  }  elseif  { $iaxis == 1 } {
    set vz -1
    set ny [expr $oy + $yMax*$sy]
    set cy [expr $oy + $slice_number*$sy]
  } else {
    set vy 1
    set nz [expr $oz + $zMax*$sz]
    set cz [expr $oz + $slice_number*$sz]
  }
  set px [expr $cx + $nx*2]
  set py [expr $cy + $ny*2]
  set pz [expr $cz + $nz*3]

  set camera [ ren1 GetActiveCamera ]
  $camera SetViewUp $vx $vy $vz
  $camera SetFocalPoint $cx $cy $cz
  $camera SetPosition $px $py $pz
  $camera OrthogonalizeViewUp
  ren1 ResetCameraClippingRange
  renWin Render
}

# Capture the display and place in a png
proc CaptureImage { } {
```

```
  vtkWindowToImageFilter w2i
  vtkPNGWriter writer

  w2i SetInput renWin
  w2i Update
  writer SetInput [w2i GetOutput]
  writer SetFileName "C:/MatLab7/Thesis/Mergetest/VTK/imageM0.png"
  renWin Render
  writer Write

  writer Delete
  w2i Delete
}

# Align the widget back into orthonormal position,
# set the slider to reflect the widget's position,
# call AlignCamera to set the camera facing the widget
proc AlignXaxis { } {
  global xMax xMin current_widget slice_number
  set po [ planeWidgetX GetPlaneOrientation ]
  if { $po == 3 } {
    planeWidgetX SetPlaneOrientationToXAxes
    set slice_number [expr ($xMax - $xMin)/2]
    planeWidgetX SetSliceIndex $slice_number
  } else {
    set slice_number [planeWidgetX GetSliceIndex]
  }
  set current_widget planeWidgetX
  .top.slice config -from $xMin -to $xMax
  .top.slice set $slice_number
  AlignCamera
}

proc AlignYaxis { } {
  global yMin yMax current_widget slice_number
  set po [ planeWidgetY GetPlaneOrientation ]
  if { $po == 3 } {
    planeWidgetY SetPlaneOrientationToYAxes
    set slice_number [expr ($yMax - $yMin)/2]
    planeWidgetY SetSliceIndex $slice_number
  } else {
    set slice_number [planeWidgetY GetSliceIndex]
  }
  set current_widget planeWidgetY
  .top.slice config -from $yMin -to $yMax
  .top.slice set $slice_number
  AlignCamera
}

proc AlignZaxis { } {
  global zMin zMax current_widget slice_number
  set po [ planeWidgetZ GetPlaneOrientation ]
```

```
  if { $po == 3 } {
    planeWidgetZ SetPlaneOrientationToZAxes
    set slice_number [expr ($zMax - $zMin)/2]
    planeWidgetZ SetSliceIndex $slice_number
  } else {
    set slice_number [planeWidgetZ GetSliceIndex]
  }
  set current_widget planeWidgetZ
  .top.slice config -from $zMin -to $zMax
  .top.slice set $slice_number
  AlignCamera
}

# Set the widget's reslice interpolation mode
# to the corresponding popup menu choice
proc SetInterpolation { } {
  global mode_widget mode
  if { $mode == 0 } {
    $mode_widget TextureInterpolateOff
  } else {
    $mode_widget TextureInterpolateOn
  }
  $mode_widget SetResliceInterpolate $mode
  renWin Render
}
# end
```

Appendix C

Technical specifications

C.1 Scanditronix-Wellhofer diode detectors

SCANDITRONIX

CERTIFICATE

RDPR-1040-01

This is to certify that detector no.

F 1949

is primarily designed for field measurements in ELECTRON beams and has the following

TECHNICAL SPECIFICATIONS

Detector material:	p-type Silicon
Thickness of the Silicon chip:	0.50 ± 0.02 mm
Detector diameter:	2.5 ± 0.1 mm
Typical effective thickness of the measuring volume:	60 µm
Preirradiation level of 10 MeV electrons:	8 kGy

Maximum deviation from linearity as a function of dose per pulse, in the range 0.1 to 0.6 mGy per pulse: <1%

Displacement from detector front surface of the effective point of measuring: 0,40 ± 0.10 mm

Sign. GR

Detector impedance at a bias of 0 V: >500 MΩ

Uppsala, Sweden 950214 Sign. ATL

SCANDITRONIX

CERTIFICATE

RDPR-1041-01

This is to certify that detector no.

EP 1942

is designed with energy compensation for field measurements in PHOTON beams and has the following

TECHNICAL SPECIFICATIONS

Detector material:	p-type Silicon
Thickness of the Silicon chip:	0.50 ± 0.02 mm
Detector diameter:	2.5 ± 0.1 mm
Typical effective thickness of the measuring volume:	60 µm
Preirradiation level of 10 MeV electrons:	8 kGy

Maximum deviation from linearity as a function of dose per pulse, in the range 0.1 to 0.6 mGy per pulse: <1%

Displacement from detector front surface of the effective point of measuring: 0,57 ± 0.15 mm

Sign. GR

Detector impedance at a bias of 0 V: 2500 MΩ

Uppsala, Sweden 950317 Sign. ES

C.2 Wellhofer Dosimetrie densitometry system

Principle of operation

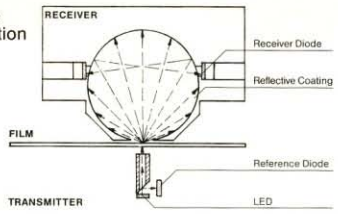

A collimated light beam from the regulated transmitter enters the film. The diameter of this beam (0,8 mm) defines the spatial resolution.

The penetrating and stray light enters into an Ulbricht sphere. Inside this sphere any multiple stray-light beam causes a signal at the light detectors, independent of the incident angle of the primary beam.

This fact provides non-critical adjustment of transmitter and receiver and supplies an extremely high longterm stability of the entire system without calibration or adjustment.

Following ISO R 5 – 1954 this system measures stray and penetrating light with the same accuracy. This provides reproducible results independent of the Callier-quotient.

Specular density aperture (option)

With this aperture, which can be retrofitted, specular density is measured to increase spatial resolution. The measurement depends on the Callier-quotient.

Technical data for specular density aperture

Light entrance of the aperture into the sphere Ø 2 mm

Range
Density 0 – 2.5, rise-time 10 ms
Density 0 – 3.5, rise-time 30 ms

Resolution with 2 mm aperture at the receiver
10 % to 90 % of full scale: 2.0 mm
10 % to 50 % of full scale: 0.8 mm
50 % to 90 % of full scale: 1.2 mm

Technical data for optical density measuremets

Light entrance into the sphere Ø 12 mm

Range
Density 0 – 3, rise-time 10 ms
Density 0 – 4, rise-time 30 ms

Scanning field
450 x 480 mm
Motor-operated in two dimensions controlled from the system controller of the phantom series WP 600 / WP 700

Resolution of display in % (selectable)
± 0.1 %

Resolution of display in density units
± 0.01

Spatial resolution with 12 mm aperture at the receiver
10 % to 90 % of full scale: 3.0 mm
10 % to 50 % of full scale: 1.2 mm
50 % to 90 % of full scale: 1.8 mm

Absolute accuracy compared to a grey-wedge with the density range 0 – 3.2 from PTB Braunschweig
± 0.005 density units

Zero stability
± 0.005 density units

Detected stray-light angle with 12 mm aperture
160°

Diameter of the Ulbricht sphere
50 mm

Measurement detectors in the sphere
four diodes symmetrically positioned in the stray light area

Light source
IR-diode 950 nm regulated, pulsed

Diameter of the collimated light-beam
0.8 mm

Control electronics
1/12 width AEC / NIM horizontally mounted in the base of the densitometer

Display
3 1/2 digits
0.00 – 4.00 density units
or selectable: 000.0 – 200 %

Analog output
1 V / density unit or selectable 10 V ≙ 200.0 %

Coordinate-information
From the system controller of the waterphantom systems WP 600 / WP 700

Dimensions (L x W x H)
700 x 660 x 350 mm

Weight
21 kg

Technical data are subject to change without notice

WELLHÖFER DOSIMETRIE
Bahnhofstrasse 5
D-90592 Schwarzenbru
Germany
Telephone 09128/607-0
Telefax 09128/607-10

References

1. Stewart, B.W. and P. Kleihues, eds. *World Cancer Report*. IARC*Press*: Lyons 2003.

2. Ministry of Health, *Atlas of Cancer Mortality in New Zealand 1994–2000*. 2005, Wellington: Ministry of Health.

3. Faiz M. Khan, K.P.D., Kenneth R. Hogstrom, Gerald J. Kutcher, Ravinder Nath, Satish C. Prasad, James A. Purdy, Martin Rozenfeld, and Barry L. Werner, *Clinical electron-beam dosimetry: Report of AAPM Radiation Therapy Committee Task Group No. 25.* Medical Physics, 1991. **18**(1): p. 73-109.

4. Varian Medical Systems, *Multileaf collimator databook 1105303-01*. 2001.

5. De Meerleer, G.O., et al., *The single-isocentre treatment of head and neck cancer: time gain using MLC and automatic set-up.* Cancer/Radiotherapie, 1999. **3**(3): p. 235-241.

6. Khan, F.M., *The physics of radiation therapy*. Third ed. 2003: LIPPENCOTT WILLIAMS & WILKINS.

7. Zhu, X.-R., E.E. Klein, and D.A. Low, *Geometric and dosimetric analysis of multileaf collimation conformity.* Radiotherapy and Oncology, 1998. **47**(1): p. 63-68.

8. Clark, B.G., T. Teke, and K. Otto, *Penumbra evaluation of the varian millennium and BrainLAB M3 multileaf collimators.* International Journal of Radiation Oncology*Biology*Physics - Intracranial and Extracranial Stereotacic Radiotherapy and Radiosurgery, 2006. **66**(4, Supplement 1): p. S71-S75.

9. Chow, J.C.L., G.N. Grigorov, and R. Jiang, *Intensity modulated radiation therapy with irregular multileaf collimated field: A dosimetric study on the penumbra region with different leaf stepping patterns.* Medical Physics, 2006. **33**(12): p. 4606-4613.

10. Chee-Wai Cheng, I.J.D., Todd Steinberg,, *Role of multileaf collimator in replacing shielding blocks in radiation therapy.* International Journal of Cancer, 2001. **96**(6): p. 385-395.

11. Kwok, C.B., G. Lam, and S. El-Sayed, *Suitability of using multileaf collimator (MLC) for photon field matching.* Medical Dosimetry, 2004. **29**(3): p. 184-195.

12. Galvin, J.M., D.D. Leavitt, and A.A. Smith, *Field edge smoothing for multileaf collimators.* International Journal of Radiation Oncology*Biology*Physics, 1996. **35**(1): p. 89-94.

13. Hwang, I.-M., et al., *An effective method for smoothing the staggered dose distribution of multi-leaf collimator field edge.* Nuclear Instruments and Methods in Physics Research Section A: Accelerators, Spectrometers, Detectors and Associated Equipment, 2002. **495**(2): p. 132-138.

14. Das, I.J., K.P. McGee, and C.-W. Cheng, *Electron-beam characteristics at extended treatment distances.* Medical Physics, 1995. **22**(10): p. 1667-1674.

15. Saw, C.B., et al., *Dose distribution considerations of medium energy electron beams at extended source-to-surface distance.* International Journal of Radiation Oncology*Biology*Physics, 1995. **32**(1): p. 159-164.

16. E. B. Podgorsak, ed. *Radiation oncology physics : a handbook for teachers and students*. 2005, International Atomic Energy Agency, 2005.: Vienna.

17. Johnson, J.M. and F.M. Khan, *Dosimetric effects of abutting extended source to surface distance electron fields with photon fields in the treatment of head and neck cancers.* International Journal of Radiation Oncology*Biology*Physics, 1994. **28**(3): p. 741-747.

18. Roback, D.M., et al., *The use of tertiary collimation for spinal irradiation with extended SSD electron fields.* International Journal of Radiation Oncology*Biology*Physics, 1997. **37**(5): p. 1187-1192.

19. Reynaert, N., et al., *Monte Carlo treatment planning for photon and electron beams.* Radiation Physics and Chemistry, 2007. **76**(4): p. 643-686.

20. Papiez, E., P.B. Dunscombe, and K. Malaker, *Matching photon and electron fields in the treatment of head and neck tumors.* Medical Physics, 1992. **19**(2): p. 335-341.

21. Karlsson, M. and B. Zackrisson, *Matching of electron and photon beams with a multi-leaf collimator.* Radiotherapy and Oncology, 1993. **29**(3): p. 317-326.

22. Sidhu, N.P.S. and C.J. Smith, *Dosimetric effects of matching electron fields with cobalt 60 fields in the management of head and neck cancer.* Medical Dosimetry, 1995. **20**(1): p. 19-24.

23. Arthur, D.W., et al., *Electron/photon matched field technique for treatment of orbital disease.* International Journal of Radiation Oncology*Biology*Physics, 1997. **37**(2): p. 469-474.

24. Sun, C., et al., *Dose Profiles in the Region of Abutting Photon and Electron Fields in the Irradiation of Head and Neck Tumors.* Medical Dosimetry, 1998. **23**(1): p. 5-10.

25. Li, J.G., et al., *Matching photon and electron fields with dynamic intensity modulation.* Medical Physics, 1999. **26**(11): p. 2379-2384.

26. Essers, M., et al., *Chest wall irradiation with MLC-shaped photon and electron fields.* International Journal of Radiation Oncology*Biology*Physics, 2000. **48**(4): p. 1205-1217.

27. Essers, M., L. van Battum, and B.J.M. Heijmen, *A linear diode array (JFD-5) for match line in vivo dosimetry in photon and electron beams; evaluation for a chest wall irradiation technique.* Radiotherapy and Oncology, 2001. **61**(2): p. 185-192.

28. Kemikler, G., *Dosimetric effects of matching 6 MV photon and electron fields in the treatment of head and neck cancers.* Radiation Measurements, 2006. **41**(2): p. 183-188.

29. Schroeder, W., K. Martin, and B.I. Lorensen, *The Design and Implementation of an Object-Oriented Toolkit for 3D Graphics and Visualization*, in *IEEE Visualization '96*. 1996: San Francisco, California, USA.

30. McKerracher, C. and D.I. Thwaites, *Notes on the construction of solid-state detectors.* Radiotherapy and Oncology, 2006. **79**(3): p. 348-351.

31. Dawson, J., et al., *Surface and percentage depth doses for secondary blocking using a multileaf collimator and cerrobend-alloy blocks.* Radiotherapy and Oncology, 1997. **42**(3): p. 285-288.

32. LoSasso, T., C.-S. Chui, and C.C. Ling, *Physical and dosimetric aspects of a multileaf collimation system used in the dynamic mode for implementing intensity modulated radiotherapy.* Medical Physics, 1998. **25**(10): p. 1919-1927.